Optoelectronic Design and Prototyping of Spectrum-Splitting Photovoltaics

Thesis by

John Vickery Lloyd

In Partial Fulfillment of the Requirements for the
Degree of
Doctor of Philosophy

CALIFORNIA INSTITUTE OF TECHNOLOGY
Pasadena, California

2018
Defended May 8, 2017

ACKNOWLEDGEMENTS

I am forever grateful for the love and support of my wife and my family. My life is richer for it, and this wonderful experience at Caltech would not have been possible without it. I also have deep gratitude and respect for my advisor, Harry Atwater. His expertise and ethic are inspiring, and I am grateful for the opportunity afforded me in his lab. Thank you to the members of the A-Team, working and learning with such an impressive group of people is one of the great honors of my life. Thank you to my Full Spectrum colleagues, these few words cannot express how much I appreciate you all, whether we overlapped by months or years. Thank you to my friends and peers, I will always treasure the support we showed each other. Thank you to the staff at Caltech who made life easier and richer, I cannot name you all, but thank you in particular Jennifer, Tiffany, Liz, Lyann, Christy, Connie, Barry, Ali, Greg, and Regina.

I would also like to thank the funders of my work presented within this thesis, the Advanced Research Projects Agency-Energy (ARPA-E) under Open 2012 Award Number DE-AR0000333 and the Dow Chemical Company under their University Partnership Program.

ABSTRACT

Global energy production is dominated by the combustion of fossil fuels but in order to avoid the projected consequences of anthropogenic climate change it is necessary that humankind reduce the carbon intensity of its energy supply. Fortunately the sun supplies a ubiquitous flow of energy of with excellent thermodynamic quality to earth. Massive investment and manufacturing scale has driven the costs of photovoltaic systems to levels competitive with fossil fuel generation, and yet commercial photovoltaic systems convert power from the sun into electricity with less than 20% efficiency. In this thesis we consider the thermodynamic and practical limits to the power conversion efficiency of photovoltaic systems and seek to design systems that address the greatest sources of loss, namely the lack of sub-bandgap absorption and the thermalization of excited carriers. We present several designs of spectrum-splitting systems that utilize optical structures to allocate incident broadband solar radiation into narrower spectral bands which can be converted by multiple distinct photovoltaic cells at greater efficiency. Furthermore, we report on the design and fabrication of thin film III-V single-junction cells at bandgaps spanning the solar spectrum for incorporation within spectrum-splitting systems. These devices were fabricated by utilizing epitaxial lift-off processes from both GaAs and InP wafers as proof of scalability. We additionally report on the fabrication and characterization of series of a spectrum-splitting prototypes. This design featured seven distinct spectral bands with single-junction photovoltaic cells designed to convert them with highest possible efficiency, and the ultimate prototype exhibited an 84.5% spectrum splitting efficiency and 30.2% power conversion efficiency under a standard AM1.5D solar spectrum. We also report a technical pathway to raise the prototype efficiency to a record breaking 45.2%. Finally, we present an optical design of a spectrum-splitting module that is informed by a technoeconomic analysis which drastically reduces the complexity and cost relative to the fabricated prototype.

PUBLISHED CONTENT AND CONTRIBUTIONS

[1] E. D. Kosten, J. Lloyd, E. Warmann, and H. A. Atwater. “Spectrum splitting photovoltaics: Light trapping filtered concentrator for ultrahigh photovoltaic efficiency”. *2013 IEEE 39th Photovoltaic Specialists Conference (PVSC).* June 2013, pp. 3053–3057. doi: 10.1109/PVSC.2013.6745105.
J. V. L participated in the conception of the project and performed optical calculations of the system.

[2] J. V. Lloyd, E. D. Kosten, E. C. Warmann, C. A. Flowers, and H. A. Atwater. “Ray trace optimization of a light trapping filtered concentrator for spectrum splitting photovoltaics”. *2014 IEEE 40th Photovoltaic Specialist Conference (PVSC).* June 2014, pp. 2249–2252. doi: 10.1109/PVSC.2014.6925373.
J. V. L participated in the conception of the project, built the ray-tracing model and the optimization algorithm, and prepared the manuscript.

[3] E. D. Kosten, B. K. Newman, J. V. Lloyd, A. Polman, and H. A. Atwater. “Limiting Light Escape Angle in Silicon Photovoltaics: Ideal and Realistic Cells”. *IEEE Journal of Photovoltaics* 5.1 (Jan. 2015), pp. 61–69. issn: 2156-3381. doi: 10.1109/JPHOTOV.2014.2360566.
J. V. L performed optical simulations of angle-restricting structures.

[4] C. N. Eisler, C. A. Flowers, E. C. Warmann, J. Lloyd, P. Espinet-Gonzalez, S. Darbe, M. Dee, M. Escarra, E. D. Kosten, W. Zhou, and H. A. Atwater. “The polyhedral specular reflector: A spectrum-splitting multijunction design to achieve ultrahigh(>50%) solar module efficiency”. *In preparation* (2016).
J. V. L participated in the conception of the project and performed the optical design of refractive concentrating elements.

[5] C. A. Flowers*, J. V. Lloyd*, C. N. Eisler, S. Darbe, P. Espinet-Gonzalez, and H. A. Atwater. “A spectrum-splitting photovoltaic submodule with seven independent junctions and 84% optical efficiency”. *In preparation* (2017).
J. V. L participated in the conception of the project, fabricated the photovoltaic devices, assisted with the prototyping and characterization of the optical systems and is co-authoring the manuscript with C. A. F.

[6] Emily C. Warmann, Cristofer Flowers, John Lloyd, Carissa N. Eisler, Matthew D. Escarra, and Harry A. Atwater. “Design of photovoltaics for modules with 50% efficiency”. *Energy Science & Engineering* (2017). issn: 2050-0505. doi: 10.1002/ese3.155. url: http://dx.doi.org/10.1002/ese3.155.
J. V. L participated in the conception of the project and the assisted with the electronic design and simulation of the photovoltaic cells.

TABLE OF CONTENTS

LIST OF ILLUSTRATIONS

LIST OF TABLES

Number *Page*

NOMENCLATURE

AM1.5D. A standard solar spectrum referring to the direct portion of solar radiation passing through an air mass of 1.5..

Base. The more lightly doped side of a pn-junction, generally thicker than the emitter and the major light absorbing layer..

BSF. Back Surface Field. A passivating layer grown adjacent to the base in a photovoltaic to reduce minority carrier recombination..

Contactless device efficiency. A metric of power conversion efficiency for a photovoltaic system that incorporates optical losses and device physics but exclude electrical resistive losses from the contacts..

CPC. Compound parabolic concentrator. A nonimaging optic that concentrates light..

ELO. Epitaxial lift-off. Seperation of epitaxially grown layers from their growth substrate via growth and etching of sacrificial release layers..

Emitter. The more heavily doped side of a pn-junction..

EQE. External quantum efficiency. A spectrally dependent metric with which incident photons are collected as photocurrent..

ERE. External radiative efficiency. The ration of luminesced light from a photovoltaic relative to the total recombination current. Generally defined at open circuit..

III-V. Compound semiconductors composed of atoms from the CAS group IIIA and CAS group VA of the periodic table..

LTFC. Light trapping filtered concentrator. A cavity-type spectrum splitting design..

PDMS. Polydimethylsiloxane. An cross-linkable organosilicon polymer with excellent adhesion to glass and optical transparency..

PSR. Polyhedral specular reflector. A family of spectrum splitting photovoltaic designs that incorporate reflection/transmission filters and a specular beam path..

TIR. Total internal reflection..

Window. A passivating layer grown above an emitter to limit surface recombination in a photovoltaic..

Chapter 1

INTRODUCTION

1.1 Solar Photovoltaics

According to the Fifth Assessment Report [1] of the intergovernmental Panel on Climate Change, the impact of additional greenhouse gas emissions resulting from economic and population growth under baseline scenarios with no efforts made to constrain emissions will cause global mean surface temperatures to rise between 3.7 °C and 4.8 °C relative to pre-industrial levels by the year 2100 with atmospheric CO_2 concentration in excess of 1300 ppm. This magnitude of climate change will herald countless negative shocks to ecosystems and human societies, and represent significant negative externalities to greenhouse gas emission which are largely unaccounted for. The IPCC further reports that constraining atmospheric CO_2 concentrations below 450 ppm will likely limit warming to 2 °C relative to pre-industrial levels or less.

The accumulating atmospheric CO_2 is resulting from the combustion of hydrocarbon fuels and the release of their previously sequestered carbon. These emissions are in excess of natural source-sink systems, and have been raising atmospheric CO_2 concentrations since the mid-18th century at an accelerating rate. In order to limit further emissions and stabilize global temperatures we must reduce the carbon intensity of our global energy systems.

Fortunately, there is a 6000 K blackbody source of free energy that provides ubiquitous power at the level of 1 kW/m^2 on the surface of our planet. Over the last decade the costs of solar photovoltaic systems have dropped significantly [2] and the scale of their utilization has increased accordingly. Greater than 70 GW of capacity of solar photovoltaics were installed in 2016 [3], the vast majority of which was single-junction silicon modules which convert incident sunlight into electricity with less than 20% efficiency.

The ability achieve scale and reduce costs has resulted in a dominant market position for silicon photovoltaics. Ultimately, though, the low power conversion efficiency is a drag on the total system costs, and efforts to increase the efficiency are a lever to reduce the associated costs of installing solar photovoltaic systems. This thesis explores optoelectronic designs alternative to tiling silicon photovoltaic cells in an effort to significantly enhance power conversion efficiencies. Although complexity resulting from such efforts is an impediment to low costs, they may ultimately offer pathways to higher system efficiencies and lower costs.

1.2 Basic Explanation of the Photovoltaic Effect

The photovoltaic effect is the spontaneous generation of voltage from a material under exposure to light was first described by Alexandre-Edmond Becquerel in 1839 while working with electrolytic cells with photosensitive electrodes [4]. Nearly 200 years hence, the photovoltaic effect is most commonly exploited with solid state semiconducting devices. There are many rich and thorough treatments of the solid state and device physics involved, and the reader is directed to references [5][6][7] for more complete treatments. A brief overview for the lay reader is included here.

Semiconductor materials are characterized by a distribution of available states for their constituent electrons to occupy which feature gaps within which no or few states exist. In thermal equilibrium the electrons in a semiconductor will populate lower energy states according to the Fermi-Dirac distribution, and the highest energy band below the Fermi level is referred to as the valance band, while the lowest energy band above it is known as the conduction band. When a photon enters a semiconductor it can excite an electron from the valence to the conduction band if there is an unoccupied state at an energy level equal to the sum of the energy of the electron and the photon. The unoccupied state in the valance band is then referred to as a “hole” and treated as a quasi-particle of positive charge.

This band-to-band absorption gives rise to the characteristic optical behavior of semiconductors, as the absorption of a photon and resulting excitation of an electron from a state in the valance band to an unoccupied state in the conduction band cannot occur for photon energies less than the electronic bandgap. Thus, there is an optical bandgap owing to the electronic bandgap, and the semiconductor is mostly transparent to photons with energy below its optical bandgap.

When electrons are excited from the valance band to the conduction band they are perturbed from their thermal equilibrium distribution given by statistical mechanics. They can decay back to thermal equilibrium by falling back down to the valance band through several mechanisms. They could emit a photon with energy of the bandgap, so called radiative recombination. They could transition through intermediate discrete states within the energy bandgap resulting from defects in the crystal lattice or impurities, known as Shockley-Read-Hall recombination. They can also interact with another excited electron and excite that electron even higher in the conduction band while falling back to the valance band a process known as Auger recombination. Regardless of the process, in the absence of light the electrons and holes within a semiconductor will rapidly relax to thermal equilibrium. However, with the continuous excitation from a light source, there will be excited populations of electrons and holes in steady state.

The distribution of the electrons and holes across the energy levels in the semiconductor are thus no longer in thermal equilibrium under steady state illumination. However, it turns out that due to the much faster relaxation processes within a band than between them, the electrons and holes can each be described by separate Fermi-Dirac distributions, with so-called quasi-Fermi levels describing them. Thus, to turn a semiconductor into a photovoltaic device all one needs is to apply electronic contacts that are selective to the carrier type, electrons or holes, such that they drive a current through an external circuit. The voltage that is seen at the external contacts is equal to the separation between the quasi-Fermi levels, divided by the elementary charge to convert between electric potential and energy.

On common way of forming carrier selective contacts is to dope opposite sides of a semiconductor n-type and p-type. This so-called pn-junction is the basis of most (though not all) commercially produced photovoltaic cells. Figure 1.1 shows the simplified band diagram of a pn-junction in the dark and under illumination at both zero applied bias and some forward bias with the quasi-Fermi levels indicated.

1.2.1 Current-Voltage Relationship in a Photovoltaic Cell

The power generated by a photovoltaic device depends on how much photocurrent it can supply at forward biases. In the simple description of a photovoltaic device in the previous section, we described how the quasi-Fermi levels of the electron and hole populations are equal to the potentials at the contacts. When there is zero voltage difference between the two contacts, as in a short circuit condition, then the quasi-Fermi levels are coincident and there is a net current flowing through the external circuit due to the photogenerated carriers. As a forward bias is applied, the quasi-Fermi levels separate, and there is a forward bias recombination current in the device that opposes the photocurrent. At some point, the forward bias recombination current is equal to the photocurrent, and there is no net current flowing through the external circuit. This is the open-circuit condition.

The maximum power point of a photovoltaic device is then the voltage at which the

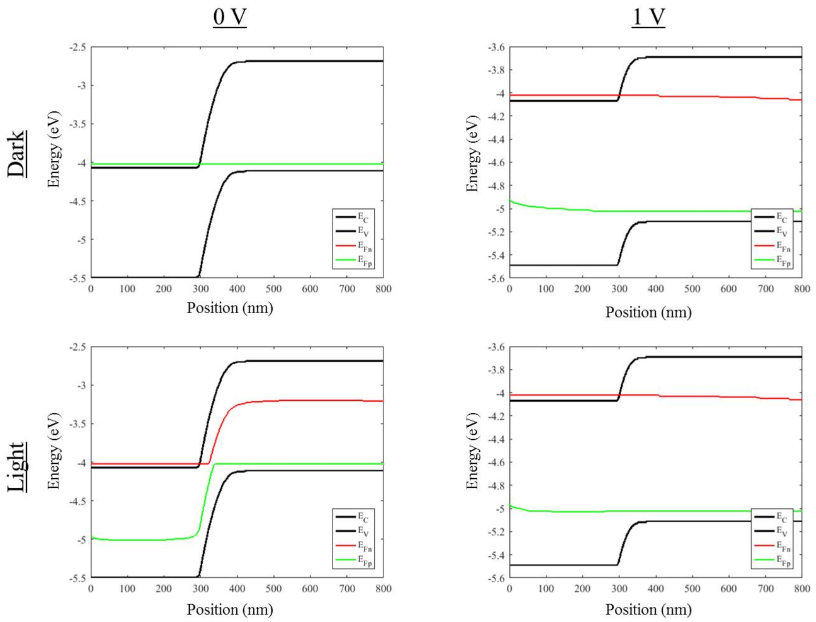

Figure 1.1: Band diagrams of a pn-junction. In the dark with no applied bias (top left), in the dark with 1 V applied bias (top right), in the light with no applied bias (bottom left), in the light with 1 V applied bias (bottom right).

product of the voltage and current is a maximum. This is the power delivered to the external circuit to drive a load. It is apparent then that the power supplied by a photovoltaic device would be optimized if the photocurrent was as high as possible, and the forward bias recombination current was as low as possible, so that many carriers can be extracted at high voltages. The ratio of the power delivered at the maximum power point and the product of the open circuit voltage and short circuit current is referred to as the fill factor of a solar cell, as in equation 1.1. A typical current-voltage relationship of a photovoltaic device is depicted in figure 1.2.

$$FF = \frac{J_{MPP} * V_{MPP}}{J_{SC} * V_{OC}} \tag{1.1}$$

1.2.2 Detailed Balance Efficiency

The question of how efficiently a photovoltaic device can convert incident optical power to electrical power is a natural and important one. The sun is nearly a 5800 K blackbody which subtends an average solid angle of 6.87 x 10-5 steridians as seen from earth. If one could create a heat engine with the sun as the hot reservoir and earth as the cold reservoir at 300 K, it could be operated with a maximum Carnot

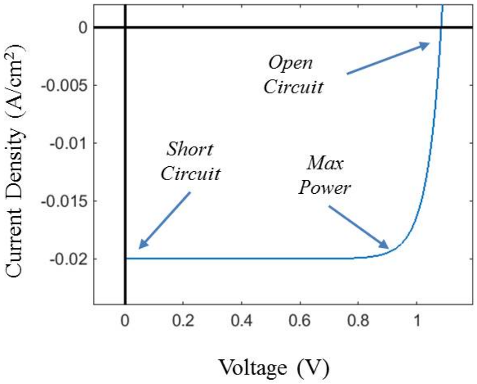

Figure 1.2: Current-Voltage behavior of a typical photovoltaic device.

efficiency of 94.8%. With appropriate geometric optics and in accordance with the first and second laws of thermodynamics, a receiver could be built on earth which is optically coupled to the sun and completely insulated from its surroundings with its temperature raised to the temperature of the sun. However, when one considers the entropy generated by the converter as it exchanges entropy with the cold reservoir one arrives at the Landsberg limit [8] of 93.3%, given by equation 1.2 where T_C is the temperature of the cell, T_S is the temperature of the sun.

$$\eta \leq 1 - \frac{4}{3}\frac{T_C}{T_S} + \frac{1}{3}\frac{T_C}{T_S}^4 \tag{1.2}$$

These efficiencies are much higher than any realized solar energy converters. To understand why, let us restrict ourselves to photovoltaic converters. The formalism of detailed balance is very useful here and used throughout this thesis, so an explanation is in order. The most well-known detailed balance model is the Shockley-Queisser limit [9] that treats the sun as a 6000 K blackbody and the solar cell as a step function absorber defined by a bandgap. Every absorbed photon generates an excited electron-hole pair which is collected at the contacts at zero bias. At applied forward bias, the device acts as a diode with a forward bias recombination current opposite the photocurrent and driven by the excess carrier populations. Shockley and Queisser recognized that due to the reciprocity of absorption and emission of light from a semiconductor, the radiative recombination current is the fundamental limiting recombination current. If the device were ideal in material quality and electronic design it would approach the radiative recombination limit, where all of the recombination current was radiative.

This offers a pathway for designing a photonically optimized photovoltaic cell. To maximize the conversion efficiency a photovoltaic device should obey three dictates. First, absorb all available incident light via inter-band absorption. Second, eliminate all non-radiative sources to the greatest extent possible. This requires good material quality to avoid defects and non-radiative recombination centers. It also requires high quality direct bandgap semiconductors, such as III-V compound semiconductors. In indirect bandgap materials non-radiative recombination mechanisms generally dominate radiative recombination owing to the lower probability of electron-phonon coupling leading to radiative emission. Third, it requires minimizing the total radiative recombination.

This final point may seem counter to earlier statements that as much of the recombination as possible should be radiative. Really, though, this is only recognizing the reciprocity between absorption and emission. A radiative recombination current at forward bias is inevitable if a device is also able to absorb all the incident light, as required by the first dictate. However, we can recognize that across the surfaces of the photovoltaic device, light is not incident from all angles at all positions. Indeed, we want to emit or admit light only from those positions and angles along the surface where there is a greater flux of incident light than emitted light at open circuit. For instance, a photovoltaic cell grown on a thick substrate will emit radiation isotropically into the substrate at open circuit even though there is no incident light coming from the substrate. This represents a net loss of flux, and the radiative recombination current could be reduced by placing a back reflector below the device and reflecting the emitted photons back into the absorber, thereby recycling them. Thus, a quantity known as external radiative efficiency is defined as the ratio of the flux of light back out of the cell towards the illumination source at open circuit to the flux of light into the cell.

1.2.3 Modified Detailed Balance Efficiency

Throughout this thesis a modified detailed balance model is used to parameterize device quality and calculate power conversion of various incident spectra with realistic device quality. The model used herein parameterizes the absorption and collection efficiency of incident light with a single term for the photocurrent, and uses external radiative efficiency (ERE) to parameterize the device quality. These are useful parameters because both are often reported [10] or can be inferred from reports of devices from literature, and they can be determined from device physics models as well. Parameterizing a modified detailed balance efficiency using values extracted from device physics models is significantly less computationally expensive than rerunning device physics simulations, and thus allows a larger design space to be examined when optimizing optical designs.

The modified detailed balance model using absorption and ERE then assumes superposition between a device under illumination and the forward bias recombination in the dark, which is generally a very good assumption for carefully designed III-V photovoltaic cells. The short circuit current is given by the incident spectra and the absorption term. The forward bias recombination current resulting from radiative recombination can be calculated as a function of applied voltage from a generalized Planck's law for emission from a semiconductor with quasi-Fermi level splitting [11] [12][13], as in equation 1.3 where, $a(E)$ is the spectral absorption of the semiconductor, V is the quasi-Fermi level splitting, and Ω is the etendue of the light emitted from the semiconductor.

$$J_{Radiative}(V) = \frac{q^4\Omega}{4\pi^3\hbar^3c^2}\int_0^\infty \frac{a(E)E^2}{e^{(\frac{E-qV}{k_BT})}}dE \tag{1.3}$$

The radiative recombination current at zero applied voltage (no quasi-Fermi level splitting) is often called the radiative dark current, and results from interband transitions from thermally excited carriers.

$$J_{0,Rad} = J_{Radiative}(0) = \frac{q^4\Omega}{4\pi^3\hbar^3c^2}\int_0^\infty \frac{a(E)E^2}{e^{(\frac{E}{k_BT})}}dE \tag{1.4}$$

The parameterized ERE then gives the total recombination current, which is $\frac{1}{ERE}$ times the radiative recombination, with care taken to track the etendue of emission. The voltage at which the recombination current equals the photocurrent is the open circuit voltage, and the rest of the power producing curve can be traced by calculating the sum of the photocurrent and recombination current between zero bias and open circuit, as shown in 1.5. The voltage at which the product of the net current and voltage is at a maximum is, naturally, the maximum power point. The ratio between the power produced at the maximum power point and the product of the short circuit current and open circuit voltage is the fill factor as described earlier.

$$J_{net}(V) = -J_{Photo} + \frac{1}{ERE}J_{0,Rad}e^{\frac{qV}{k_BT}} \tag{1.5}$$

This simple model as described assumes, somewhat unphysically, that the ERE is independent of illumination level or voltage in a device. In actuality this is not generally true, and depends on how the non-radiative recombination mechanisms scale with voltage, if differently that the proportionality of radiative recombination. In order to more accurately model the device performance not just at open and short circuit current, but at the maximum power point as well, a parameter can be added that describes how the non-radiative recombination current scales with voltage.

This is done by adding a second diode term, resulting in a double diode model. The scaling of non-radiative recombination is parameterized by an exponential term and assuming a log-linear behavior described by a diode ideality, n_2 in equation 1.6. Here J_{net} is the net current to the external circuit, J_{photo} is the photogenerated current parameterized by an absorbance and taken to be negative by convention.

$$J_{net}(V) = -J_{photo} + J_{0,Rad}e^{\frac{qV}{k_BT}} + J_{0,Non-Rad}e^{\frac{qV}{n_2k_BT}} \tag{1.6}$$

The exponential prefactor $J_{0,Non-Rad}$, representing the non-radiative recombination current at zero applied bias, can be determined by solving the for the non-radiative recombination at open circuit from the definition of the ERE and extrapolating back to zero bias with the assumed ideality, n_2.

$$J_{Non-Rad}(V_{OC}) = J_{0,Rad}e^{\frac{qV_{OC}}{k_BT}}\left(\frac{1}{ERE} - 1\right) \tag{1.7}$$

$$J_{0,Non-Rad} = \frac{J_{Non-Rad}(V_{OC})}{e^{\frac{qV_{OC}}{n_2k_BT}}} \tag{1.8}$$

This double diode modified detailed balance model is capable of better capturing deviations from ideality due to non-radiative recombination. With three parameters it can faithfully fit a current-voltage trace of a photovoltaic device at the short circuit current, open circuit voltage, and maximum power point. Its fidelity to data away from those three points depends on the validity of the underlying assumptions, and additional exponential terms can be added to improve fitting if desired. The double diode model for radiative and non-radiative recombination, however, provides a computationally simple model with some physical basis to simulate the performance of single junction photovoltaic cells under an arbitrary spectral irradiance. Figure 1.3 depicts a semilogarithmic plot of the recombination currents in the dark and a linear

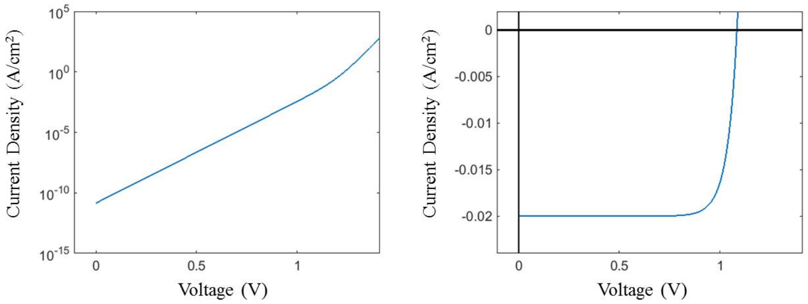

Figure 1.3: Left: Semilogarithmic plot of forward bias recombination current from a double diode model. Right: Plot of net current from a double diode model with photocurrent.

plot of the net current under forward bias under illumination for a simulated 1.42 eV device with step function absorption above bandgap and 20 mA/cm^2 photocurrent.

1.2.4 Hydrodynamic Analogy

Having described the basic photovoltaic effect, a mechanical analog can provide a more intuitive appreciation of a photovoltaic device. Consider a container which collects rainwater and releases it through through a valve to drive a waterwheel and extract power. The release valve is located at the bottom of the tank, and the higher the water level in the device, the greater the pressure at the valve to drive the generator. The water pressure due to the height of the water column is analogous to voltage in a photovoltaic device. The flow of water out of the valve to drive the generator is analogous to the current delivered from a photovoltaic to an external load. If the valve is fully open such that all of the rainwater being collected is flowing out the valve without building up any height that is equivalent to the short circuit condition in a photovoltaic cell. Maximum current is being extracted but at zero voltage, and thus no power delivered. Similarly, if the valve is fully closed the water column reaches maximum height but with no flow, as in the open-circuit condition of a photovoltaic device.

In a rain catch basin, the height of the water could continue to rise until the container is full, but this is not a meaningful situation in a photovoltaic device, so consider the following modifications. First, allow that evaporation of water from the surface is significant, and proportional to the surface area of the rain catch. Next, allow that the vertical profile of the container walls flare outward, such that the area increases exponentially with height. This provides analogy to the radiative recombination and emission from a photovoltaic device. In our rain generator, if the valve is fully closed the water level will now only rise to the point where the rate of evaporation is equal to the rate of collected rain. Now there is a maximum flow rate for water to be extracted, as too much water flow results in low water column height and low pressure, and too little flow means the water height increases and too much water is lost to evaporation.

Consider now that the base of the container is semipermeable, with a flow rate exponentially proportional to the pressure of the water, that is to say the height of the water level, with the exact same proportionality as the evaporative loss. This loss is analogous to radiative recombination that does not go back out the top of a photovoltaic device, but rather is absorbed in a growth substrate or other device layers and does not contribute to the quasi-Fermi level splitting in the absorber layers. The evaporative loss is a necessary condition of getting rain into the collector, but the leakage through the bottom is not. This is analogous to so-called photon recycling in photovoltaic cells. To extract maximum efficiency from a photovoltaic cell light can enter or escape through the top side, as required by reciprocity, but any light escaping through positions and angles where a greater amount of light is entering lowers the efficiency of the device.

Consider finally a series of cracks or holes along the bottom of the rain collector. These are analogous to various non-radiative recombination mechanisms in a photovoltaic device. The flow of water lost through them is again exponentially proportional to the pressure or height of the water column. These leaks represent recombination through intra-band defect states, from impurities in the material to crystallographic defects. Some can be eliminated or minimized by careful materials growth. Recombination at the sidewalls of devices where intra-band surface states can dominate the total recombination in small devices can be mitigated by chemical passivation of dangling bonds.

An ideal rain water generator then is one where all rain that falls on it is collected, the cracks and holes are plugged, the bottom is sealed, and when the valve is closed the rate of evaporative loss is equal to the rate of rain collected. This evaporative efficiency of unity is analogous to an external radiative efficiency of unity in an ideal photovoltaic device. This ideal photovoltaic device, in the so-called radiative limit, collects all incident light and at open circuit the emitted flux of light out the top of the device equals the flux of incident light. Collecting all the rain is making it optically thick. Plugging the cracks is eliminating electronic defects. Sealing the

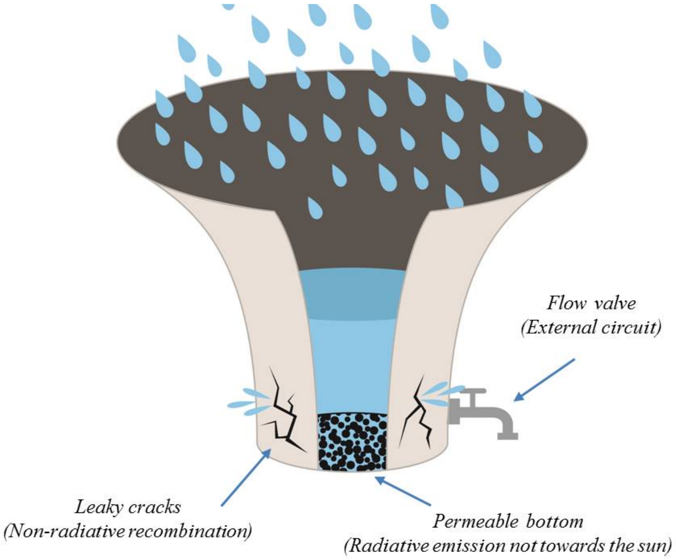

Figure 1.4: Illustration of the hydrodynamic analogy of a solar cell with components labeled and their photovoltaic analogs indicated in parenthesis. Figure courtesy of Loren Vitello.

bottom is placing a reflector on the bottom of the device. Figure 1.4 illustrates this analogy.

1.3 Multijunction and Spectrum Splitting Photovoltaics

Appreciating that the largest loss mechanisms [14] inherent to the photovoltaic effect for a broadband source are the related lack of sub-bandgap absorption and thermalization of excited carriers, the obvious solution is to convert different portions of the broad solar spectrum in different photovoltaic devices with different bandgaps. The methods for incorporating multiple bandgaps into a system are grouped into two categories depending on their optical architecture, referred to as multijunction photovoltaics and lateral spectrum-splitting photovoltaics.

In multijunction photovoltaics a single material growth or stack with the multiple absorbers directly in contact with each other separates the spectrum through absorptive filtering. Light passes in series through the absorbed in descending order of bandgap and each spectral band is absorbed in order. In spectrum-splitting approaches the different absorbers are separated in space, and an optical element distinct from the cells themselves uses some mechanism to direct spectral bands upon the different cells. These distinctions can become blurred when single junction cells are arranged laterally to absorptively filter a beam bouncing across them in a spectrum splitting configuration, or physically stacked upon each other to absorptively filter a beam in so called mechanically stacked multijunctions, but in multijunction photovoltaics the cells themselves perform the optical and electrical functions, while in spectrum splitting there are optical elements that split the beam and electrical devices which convert each spectral band.

1.3.1 Benefits of Spectrum Splitting

The primary reason to pursue spectrum splitting photovoltaics rather than multijunction photovoltaics is that multijunction photovoltaics are practically limited to five or fewer bandgaps. Typical multijunction devices that were deployed in commercial systems employed three bandgaps[15], and four bandgap devices currently hold the concentrator cell efficiency records [16]. The primary reason is that in order to reach the highest efficiencies possible high quality materials are used, and this means epitaxial growth of all the constituent absorber layers on a single growth substrate. Unfortunately, there do not exist in nature material systems with tunable bandgaps that spans a wide energy range at similar enough crystallographic lattice constants. Growing materials with different lattice constants in the same growth gives rise to crystallographic defects that degrade the electronic quality of the resulting devices, and the diminishing returns to efficiency from additional junctions are overwhelmed by the loss of efficiency due to material quality. In spectrum splitting designs there is no such material limit to the number of junctions that can be incorporated, as long as the complexity of the optical system can be managed. Optical losses at interfaces and alignment losses can compound with increasing numbers of absorbers in spectrum splitting photovoltaics, but these can be designed around in a way that the thermodynamics of crystallographic growth cannot. Any system capable of reaching very high (>50%) power conversion efficiency will require a number of bandgaps in excess of what is practical with monolithic multijunction devices.

Typically then multijunction photovoltaics involve absorbers that are not just optically in series but also electrically in series, and impose a constraint on the operation of the devices that the photocurrents must all be equal to satisfy Kirchoff's law. This leads to some loss in efficiency because not every cell can operate at its maximum power point except under fortuitous spectral conditions. In contrast, spectrum splitting designs have cells with independent electrical connection, which allows the cells to each be independently driven at its maximum power point. This effect can potentially offer greater energy yield over the course of a day and a year as the solar spectrum changes. Dr. Emily Warmann has modeled [17] that for systems with seven bandgaps, this benefit of independent maximum power point tracking could yield up to 15% greater energy yield over the course of a year when independently electrically connected rather than connected in series.

Finally, another potentially significant benefit to spectrum splitting photovoltaics is reduced thermal loads on the photovoltaic cells [18]. In photovoltaics, much of the energy not extracted as power from the device is lost dissipated as waste heat in the cell. This raises the temperature of the device, and as in any heat engine the efficiency degrades as the cold reservoir gets warmer. In multijunction photovoltaics this is a significant loss in efficiency, as they are deployed in systems with optical concentration on the order of several hundred suns to reduce the cost of the cells. As the multiple absorbers are located in intimate thermal contact, all the waste heat is generated in the same place and must be dissipated. In a spectrum splitting approach, by contrast, the cells are often physically isolated, meaning that the waste heat can be dissipated from multiple distinct points, lowering the steady state temperature of the devices. Furthermore, with more spectral bands and more efficiency single junction devices, there is less waste heat generated per band and thus lower operating temperatures and higher operating efficiencies.

1.4 Spectrum Splitting Systems

Spectrum splitting photovoltaics exploit some optical phenomenon to perform the task of separating incident broadband light in space according to its energy. There are many physical mechanisms that have been used or proposed in spectrum splitting photovoltaics, including dispersion, diffraction, absorption, and interference. Conceptually, one can categorize spectrum splitting designs according to whether they steer a beam in different forward directions or whether they split a beam in reflection and transmission across an interface.

Examples of systems that steer light including using dispersion, such as prisms [19] [20] or lenses with chromatic aberration, or diffraction as with holograms [21][22] or polychromats [23], or interference based filters [24], to send incident broadband light forward at different angles. Examples of splitting systems include using interference based dichroic filters or high contrast gratings. Splitting designs can be further classified according to whether the splitting elements are arranged such that the incident light strikes them in series or in parallel. In series configurations the design of the geometric optical systems must ensure a specular beam path that strikes the elements in the correct order. In parallel systems there must be a way to couple rejected light between elements, as in an optical cavity. These categorizations are not exclusive, and designs can conceivably include aspects of multiple categories, but they provide a useful conceptual framework to consider the wide variety of spectrum splitting designs.

1.4.1 Sharpness of Spectrum Splitting Mechanisms

The marginal benefit from adding additional absorbers to a spectrum splitting design diminishes with increasing total number, and thus it is apparent that in order to gain a net benefit the spectral allocation must be very good[25]. A design with many bandgaps that poorly allocates light between them can be inferior to one with fewer bandgaps but better spectral allocation. We might call this the sharpness of the splitting mechanism. That is to say how sharp is the transition in the allocation between in-band and out of band light?

To illustrate, consider two hypothetical splitting mechanisms. The first has perfectly allocates light within a spectral band to each constituent photovoltaic cell, except in some transition region between bands where it linearly transitions allocation between adjacent cells. This transition can be described by a width in the spectrum, here considered in nanometers, and we may refer to it as the series design. The second mechanism correctly allocates some fraction of light to the correct photovoltaic cell, and randomly distributes the rest between all remaining cells, and we may call it the parallel design. We can calculate the system efficiency with a modified detailed balance model for various bandgap ensembles with different numbers of cells. Let us assume for simplicity that all cells have an external radiative efficiency of 1%, 92% in-band absorption, non-radiative ideality of 1.3 and external optical concentration of 500x. The split spectra for a bandgap ensembles containing 10 bandgaps with various degrees of splitting sharpness are shown in figure 1.5 for the series design and in figure 1.6 for the parallel design.

Figure 1.7 depicts the efficiency landscape for these two hypothetical splitting designs as a function of the number of bandgaps and the sharpness of the splitting. It is apparent that the marginal benefit to increasing number of junctions is reduced with poorer splitting sharpness. Thus, we can conclude that to realize the high theoretical efficiencies of a large number (>5) of bandgaps, we need a sharp splitting mechanism. This provides us with a heuristic to quickly assess various spectrum splitting designs, and abandon efforts to develop them if they cannot split the spectrum with

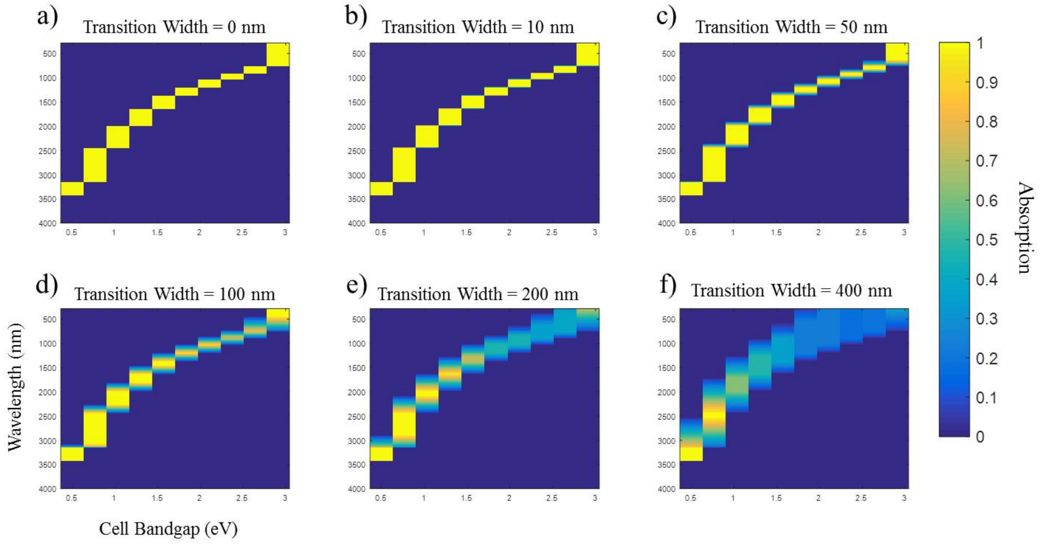

Figure 1.5: Absorption in each cell in a 10 bandgap ensemble for six different transition widths of the series splitting mechanism.

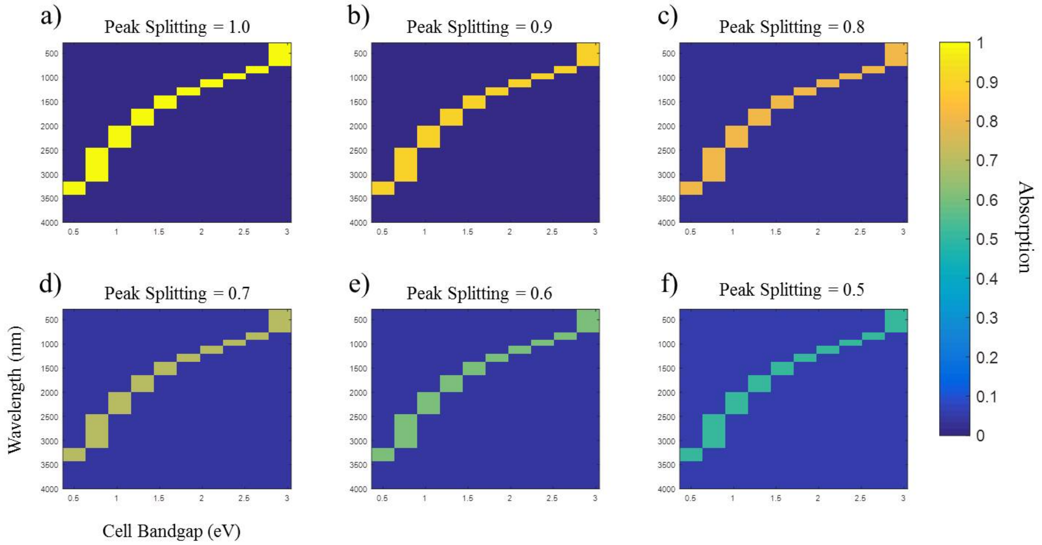

Figure 1.6: Absorption in each cell in a 10 bandgap ensemble for six different peak splitting efficiencies of a parallel splitting mechanism.

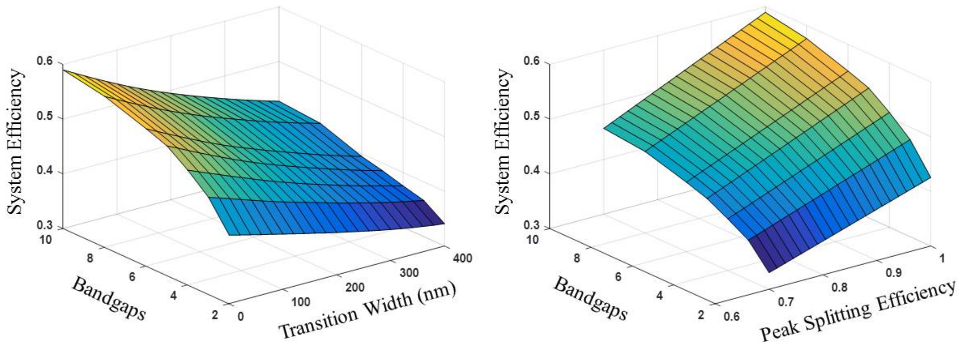

Figure 1.7: System efficiencies as a function of the size of the bandgap ensemble and the sharpness of the splitting mechanism for the hypothetical series (left) and parallel (right) mechanisms described in the text.

sufficient fidelity.

Chapter 2

LIGHT TRAPPING FILTERED CONCENTRATOR DESIGN

2.1 Concept

The light trapping filtered concentrator (LTFC) is one realization of a cavity-type [26][27] spectrum splitting concentrator. The operating principle is to create an optical cavity in which light is admitted and trapped to create a high intensity, and then spectral bands are selectively coupled into solar cells adjacent to the cavity. In order to achieve high efficiencies, the cavity must admit as much light as possible while simultaneously trapping already admitted light. Additionally, the optical structures which couple the photovoltaic cells to the cavity must admit in-band light and reject out of band light with exactness.

The LTFC is comprised then of the following components. There is a solid optical cavity, referred here as the slab due to its planar nature. There is some scattering element that scatters incident light into the slab in a Lambertian manner to maximize light trapping. There is an optical element that restricts the angles of acceptance into the slab and, equivalently, emission from the slab. There are photovoltaic cells of various bandgaps coupled to the bottom of the slab to convert the optical power into electrical power. Finally, in most embodiments there would be a primary optical concentrator above the slab that increases the intensity of incident light within the slab. This external concentration comes at the cost of a higher angular divergence incident upon the slab, and must be accounted for in the optical design.

In order to raise the intensity of light within the cavity we propose a planar slab of material with high refractive index. The greater the refractive index, the greater the number of optical modes in which light can propagate within the slab, and with some appropriate surface or volume scattering mechanism to couple incident light into those modes, the intensity of the light within the slab can increase by up to $4n^2$ [28]. This is a consequence of total internal reflection and the smaller cone of escape within the higher index slab. Unfortunately, materials with a large real index of refraction also tend to have lower bandgaps [29] which would impinge upon the solar spectrum, and dampen the quality of the cavity for shorter wavelengths. Empirically, if we wish to keep the optical bandgap of the slab material above 3 eV, we are limited to materials with refractive indices below 2.

The scattering element would ideally be some random texturing of the front surface of the slab. Random surface texturing is a demonstrated mechanism [30] for Lambertian scattering of light into a medium, and it has the advantage of being a forward scattering mechanism. Alternative possibilities include embedding scattering particles within the slab, but this raises the possibility of backward scattering incident light which would be an undesirable loss mechanism. One consideration then for selecting the material for the slab would be something which is compatible with random surface texturing.

2.2 Angle Restriction

There is another way that light can be trapped within the slab, however. The $4n^2$ light trapping can be achieved by accepting light from all angles in air above the slab and scattering into all angles within the slab. However, if we restricted the angles from which light is emitted from, and regrettably but necessarily by reciprocity accepted into, the slab we can arbitrarily reduce further the escape cone for light within the slab. Thus, when light is scattered into all angles within the slab, the smaller the cone of escape angles is, the higher the intensity within the slab and the better the light trapping.

There are several structures with which we could restrict the angles of emission of light from the slab. One possible way is with interference based optical filters, composed of alternating layers of different materials with different indices of refraction. These are challenging to make broadband, however, and tend to have some wavelength dependence which could degrade the performance. A second possibility is the use of geometric features to restrict the emission angle. If an array of geometric concentrators is close-packed, arranged such that their smaller aperture is against the slab and their larger aperture is facing the sun, then light emitted from the slab into the small apertures is collimated back towards the sun. This is depicted in figure 2.1.

Compound parabolic concentrators (CPCs) are a class of non-imaging geometric concentrators. Their sidewalls are parabolic profiles, offset and tilted relative to each other in a manner that determines the range of angles they admit and emit. Most light incident upon the input aperture within the designed acceptance angle will be reflected through and out the output aperture within the designed output angle. There are some skew rays which will be rejected despite being within the acceptance angle, but their number is small and can be accounted for in the design for they exist

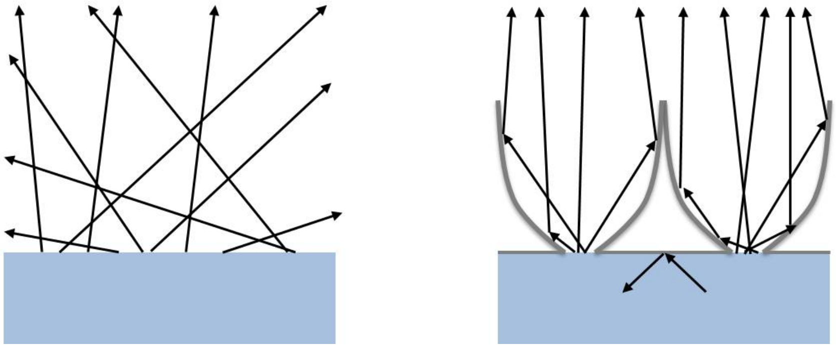

Figure 2.1: Schematic of angular restriction via geometric collimating optics. Left: Isotropic light emission from a higher refractive index medium into a lower one, with light emitted into all angles. Right: Collimation of emitted light into a lower refractive index medium by tiled compound parabolic concentrators.

at the margin of the design angle. CPCs can be designed with rotational symmetry or with polygonal apertures, and we use here hexagonal apertures, which suffer less skew ray rejection than square CPCs, but close pack in space unlike circular CPCs.

Light within the slab that strikes the output face of a CPC within the escape angle of the slab material will be lost back towards the sun. However, since the output faces are smaller than the input faces, in a fashion determined by the acceptance and emission angles, the output faces cover less than the full area of the top of the slab. The remaining area can be covered in a reflector, thus reducing the area from which light can escape. Thus, using geometric concentrators we can increase the light trapping of the slab by reducing the area from which light can escape. The geometric concentrators provide equivalence between the area of escape and the angular divergence of the emitted light, and when considered as a system, this is equivalent to reducing the escape cone within the slab by restricting the divergence of emitted light.

The next important component of the LTFC is the ensemble of photovoltaic cells that do the optical to electrical power conversion. We propose these to be from the III-V compound semiconductor family because that provides a range of possible bandgaps that spans the solar spectrum. Photovoltaic devices made from III-V materials have been demonstrated with extremely high performance owing to the ability to grow high quality epitaxial layers of various and controllable composition and doping levels. Furthermore, III-V solar cells can be fabricated as thin film devices with a back reflector, which can serve to recycle unabsorbed light back into the cavity.

The final component of the LTFC system under consideration is the external optical concentrator. We do not concern ourselves deeply with the design of this element, but rather propose it would be similar to any number of demonstrated geometric optical concentrators. This could be a reflective element or more likely a refractive element such as a plano-convex or Fresnel lens. Fresnel lenses have been the most widely deployed geometric concentrator for concentrating photovoltaic systems as their low profile saves weight and cost and is compatible with a box-like module form factor. For our purposes, we care only that the primary concentrator accepts light on its front aperture within an acceptance angle and concentrates it onto the slab with some larger angular divergence, determined by the degree of geometric concentration.

2.3 Analytical Multi-Pass Model

We can calculate aspects of the system performance of a light trapping filtered concentrator with a simple analytical model. If we consider the light trapping cavity has multiple different bandgap photovoltaic cells of number s arranged in some checkerboard fashion against the bottom of the cavity, then each time a photon strikes the bottom face of the cavity it has a probability of $1/s$ of striking the cell designed for it and being absorbed. All the light which enters the cavity will strike the bottom face at least once, but any light not absorbed by the correct cell on the first pass will have a possibility of escaping the cavity out the top. This is $(1 - 1/s)$ of the total incident light. If we allow some probability of escape, p, which as we discussed is related to the size of the angular escape cone, then $(1 - p)$ of the light not absorbed on the first pass is reflected back down towards the cells for a second chance at striking the correct cell. Thus, the amount of light absorbed on the second pass becomes $(1/s) * (1 - p)$. Each successive pass gains an extra power for the probability of absorption and probability of not being emitted. This logic can be extended indefinitely and the resulting series of terms can be summed, as in 2.1.

$$A = \frac{1}{s} * \sum_{i=1}^{\infty}(1 - \frac{1}{s}) * (1 - p)^i \tag{2.1}$$

This summation has a geometric series equivalent in the form of equation 2.2.

$$A = \frac{\frac{1}{s}}{(1 - \frac{1}{s}) * (1 - p)} \tag{2.2}$$

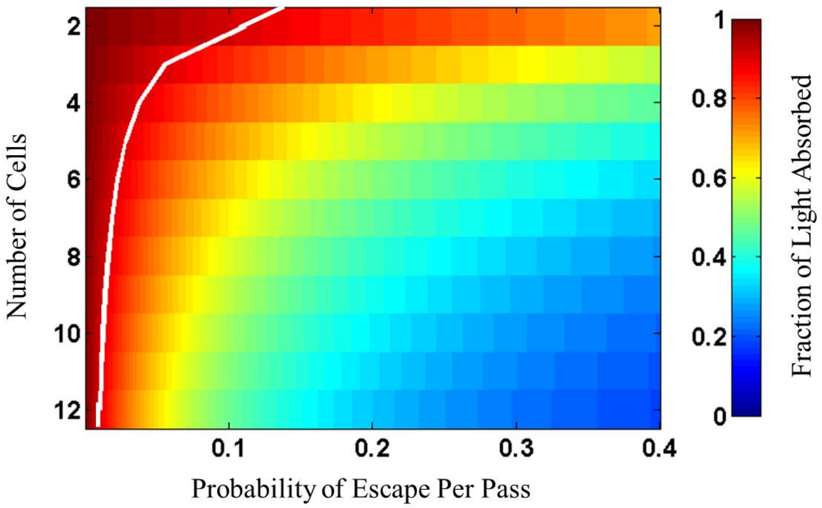

Figure 2.2: Fraction of incident light ultimately absorbed in the cells of an LTFC with perfect optical filters as a function of the number of cells and the probability of escape per pass. The white line indicates an isoefficiency contour at 90% absorption in the photovoltaic cells.

If we sweep out the parameter space of number of cells and probability of escape from the slab on each pass, we can observe the region where there is sufficiently good allocation of light according to its wavelength to allow for high optical efficiency. In this simple model we have assumed perfect filters on each cell, admitting all photons in band and rejecting all photons out of band. Additionally, there is no accounting for any parasitic optical absorption in the system. Figure 2.2 depicts the fraction of light which is correctly absorbed in its corresponding cell in such a system as a function of the number of cells and the probability of escape per pass. The white line denotes an isoefficiency contour at 90%, and demonstrates that in order to achieve high optical efficiency both the number of cells and the probability of escape must be kept low.

The probability of escape per pass is directly related to the index of refraction of the slab and the extent of the emission angle restriction from the slab. Specifically, the probability of light inside the slab striking an aperture of an angle restricting CPC is related to the concentration ratio of each CPC, and assuming the CPCs output at 90 degrees into the slab, this concentration ratio is equal to $\frac{1}{\sin^2\theta}$ where θ is the acceptance angle of the CPC. Additionally, once a photon strikes such an aperture from inside the slab, the probability of escape into air is equal to $\frac{1}{4n^2}$ because of the

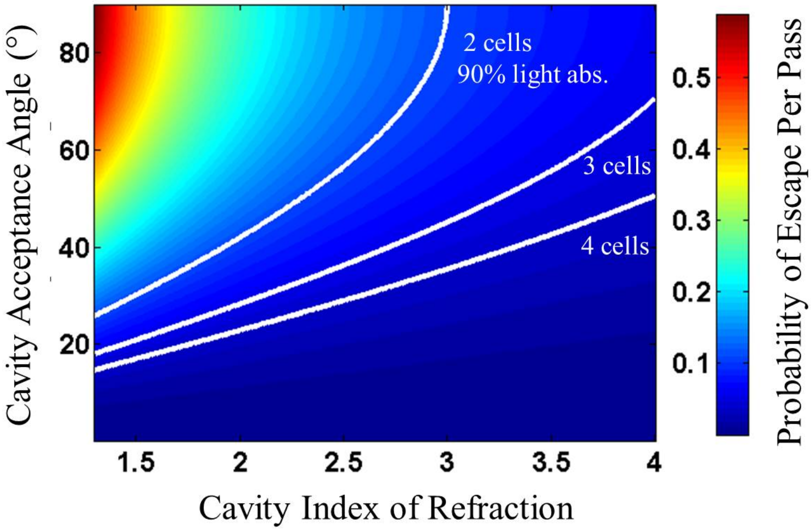

Figure 2.3: Probability of escape from the LTFC cavity per pass as a function of the refractive index of the cavity and the extent of emission angle restriction. White contours correspond to a probability of escape equal to 90% absorption for 2, 3, and 4 cells.

ergodic light trapping. The probability of escape on each pass is thus the cumulative probability of these two events, equal to $\frac{\sin^2\theta}{4n^2}$. Figure 2.2 demonstrated that there is a design space where greater than 90% of incident light is directed to the correct cells with a sufficiently low probability of escape per pass. Figure 2.3 shows that an appropriately low probability of escape per pass can be achieved with reasonable slab index of refraction, angle restriction and small number of cells.

The white contours on figure 2.3 depict contours where the probability of escape for the given number of cells equates to 90% of the light absorbed in the correct cell. It is apparent that with angular restriction of less than 20 degrees and an index of refraction of just 1.4, 90% of the light can be correctly allocated for three cells. Three bandgaps are not sufficient to reach ultra-high efficiencies, but each cell could in principle be a monolithic multijunction device, featuring 2-3 bandgap absorbers optically and electrical in series. This would allow 6-9 bandgaps in an LTFC design with high optical efficiency.

2.4 Ray Trace Model

The simple analytical model described thus far demonstrated that a feasible design space exists where a large number of bandgaps (6-9) can be utilized with greater

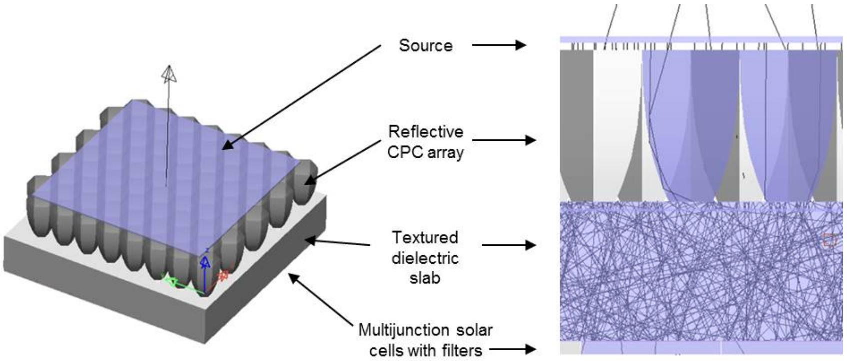

Figure 2.4: Perspective view (left) and cross section (right) of ray trace model of an LTFC.

than 90% proper spectral allocation for a non-absorbing slab material (Silicate glass) utilizing moderate emission angle restriction (20 degrees). There are many geometric and material details ignored by this simple model, however, and in order to probe the true efficiency potential of this design a ray trace model was constructed using Synopsis LightTools, a commercial ray tracing software package. Figure 2.4 shows a ray trace of a typical LTFC geometry with the various components identified.

Ray tracing models allowed a comprehensive examination of the LTFC geometry and were used to validate certain assumptions of the early analytical. For instance, the analytical model presented earlier assumed that on each subsequent bounce a ray was randomly sampling the available photovoltaic cells attached to the cavity. It is obvious though that in the limit of a very thin slab rejected rays will strike the same cell multiple times before impinging upon an adjacent cell. However, as the slab is made thicker there increasing optical path length on each bounce and volumetric absorption can reduce the efficiency. Figure 2.5 depicts the resulting trade-off. As the slab becomes as thick as the cells are wide, the assumption of random sampling becomes increasingly valid. There is a broad maximum, and then increasing volumetric absorption takes a slowly increasing toll on the efficiency.

The necessary equivalence between the width of the cells and the thickness of the slab is an important design constraint. Any economically practical implementation of this design without primary optical concentration would be limited to a slab thickness below one centimeter, and likely on the order of the 3 mm glass found in commercially available flat plate silicon modules. Cells this small would require approximately 100,000 cells per square meter, and the associated complexity

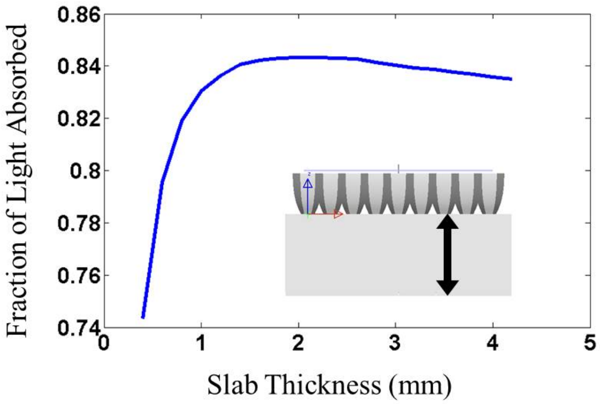

Figure 2.5: Modeled efficiency of an LTFC as function of thickness of slab (cavity), for 2 mm wide cells.

of placement and interconnection would be a significant technical and economic challenge. This is a strong driver towards the LTFC as a receiver under a high concentration optic rather than as a tracked flat plate or low concentration design.

One important non-ideality present in the ray trace but lacking in the analytical model is the presence of skew rays that are rejected from the CPCs without entering the slab. Two ways to minimize skew ray rejection are to increase the acceptance angle of the CPCs or decrease their output angle. Both of these modifications consume some of the angular budget afforded by the solid angle of the sun and the conservation of etendue, and thus come at the expense of primary concentration, light trapping, or some combination thereof.

2.4.1 Filter Design

At this point attention should be paid to the optical filters that couple the cells to the slab. The ideal behavior of these filters is unity transmission in-band and unity reflectance out of band, where each band is defined between the electronic band edge of the lowest bandgap absorber in each multijunction cell. For instance, if there are two cells with bandgaps of 1.1 eV and 1.7 eV, the two relevant spectral bands would extend from 300 nm to 729 nm and from 729 nm to 1127 nm. 300 nm is chosen as the short wavelength limit of simulations as shorter wavelength light is very strongly attenuated and not a significant source of power. Furthermore, in the ideal case the spectral properties of the filters are insensitive to the incident angle of light, as light within the slab is ergodically scattered in all directions.

We focused design efforts on aperiodic multilayer dielectric stacks of alternating materials of different refractive index. The spectral properties of these filters can be designed by controlling the indices of refraction, thickness, and number of the constituent layers. Such interference based filters inevitably have sensitivity to incident angle, but they are a well understood commercial technology that can exhibit the very high in-band transmission and out of band reflection necessary for high optical efficiencies.

In the design of aperiodic dielectric stack filters, certain trade-offs are made between various filter properties. The optimal design of the set of filters that would yield the highest efficiency module was then not a priori obvious, and so a method was developed to design and compare a large set of filters. Additionally, the optimal geometric design of the LTFC may not be the same for every set of filters. Filters with better in band transmissivity may favor designs incorporating less light trapping and more primary concentration, and vice versa for filters with less transmissivity but better out of band reflection. The most interesting comparison is the highest achievable efficiency of each set of filters with its own optimal cell bandgaps and LTFC geometry.

The freely available software OpenFilters was used to generate a large number of candidate filter designs with different spectral responses. Designs were seeded manually by creating a basic filter with rudimentary anti-reflection, short-pass, band-pass, or long-pass characteristics, and then programmatic optimization was applied to these seeds to generate a variety of optimized filters. Specifically, design targets for transmission and reflection were set for a large number of wavelengths weighted by the AM1.5D solar spectrum standard, and the weighting of these targets was varied between filters to generate diversity. The resulting ensemble of filters had varying numbers of layers, cutoff wavelengths, and transmission/reflection spectra. Of this large ensemble, a smaller set representing 600 possible combinations of three filters was selected as having the best characteristics, and more than 100 combinations were evaluated using the ray tracing model to understand design trends. Figure 2.6 depicts example long-pass and band-pass filter tangle averaged reflectivity, and the influence of varying the total thickness the filters on the reflectivity.

2.4.2 Optimization

To evaluate each set of filters the flux to each multijunction cell was determined via the ray trace model, and a modified detailed balance model assuming 0.1%

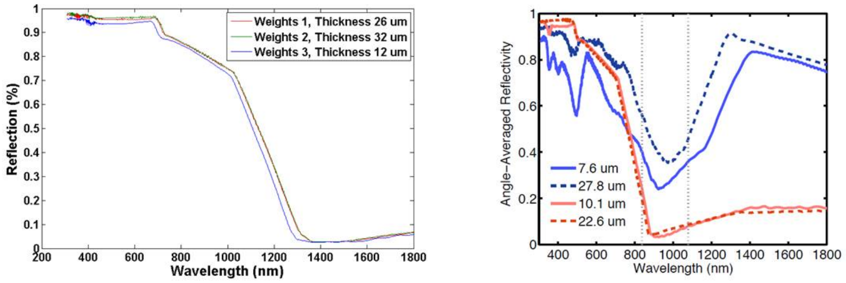

Figure 2.6: Left: Angle-averaged reflectance of three long-pass filter designs with varying optimization weights and total thicknesses. Right: Angle-averaged reflectivity for several long-pass and band-pass designs with different total thickness.

external radiative efficiency and 90% internal quantum efficiency was used to calculate module efficiency. The geometry of the LTFC was optimized for each filter combination by applying a gradient ascent algorithm via a scripted ray trace model that incorporated realistic non-idealities of the design, using the module efficiency as the figure of merit.

The optimization algorithm operated on the reduced design space of three geometric parameters that define the light trapping and external concentration. Those three parameters are the acceptance angle of the hexagonal CPCs, the output angle of the hexagonal CPCs, and the difference between the angular spread of the primary concentrator and the acceptance angle of the hexagonal CPCs, called here the acceptance angle offset. The input and output angles of the hexagonal CPC array define the extent of light trapping within the slab. However, at greater output angles hexagonal CPCs suffer additional skew ray rejection, so there is a trade-off between coupling light into the slab and trapping it there. Furthermore, reducing the hexagonal CPC acceptance angle promotes light trapping, but this then limits the amount of primary concentration. Finally, the acceptance angle offset allows the design to give up some degree of light trapping and concentration to promote coupling light into the slab. These three optimization parameters allow comparison between each combination of filters with each having its specific optimal combination of primary concentration, light trapping, and coupling of light into the slab.

It was not known a priori if this geometric design space was convex, so several computationally intensive parametric sweeps on various models were performed. These sweeps all showed convex landscapes suitable for a simple gradient ascent optimization. Furthermore, they suggested reasonable initial positions to reduce the

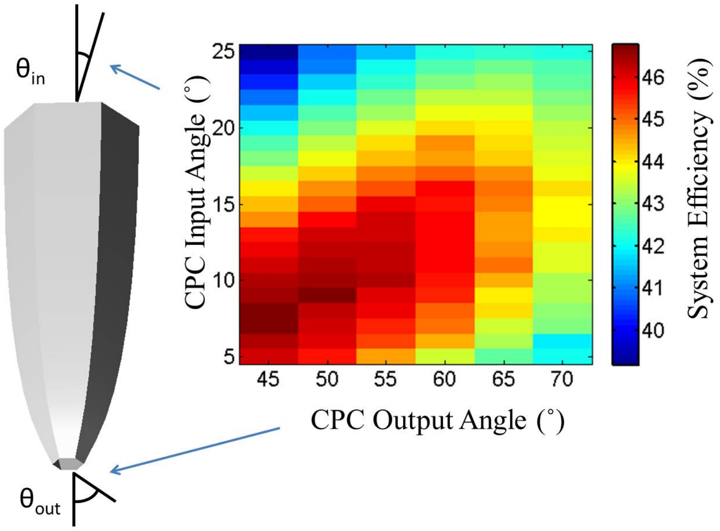

Figure 2.7: Simulated system efficiency of an LTFC with ideal filters as function of the input and output design angles of the angle-restricting CPCs.

computational complexity of the optimization. To ensure this did not harmfully bias the optimization, occasionally random seeds were used that also converged towards the same optimum. Figure 2.7 depicts the efficiency, which is the figure of merit for the optimization, as a function of two of the optimization parameters for an arbitrary filter set to demonstrate the convex nature of the design surface.

2.4.3 Results

Several trends were observed throughout the ray tracing optimizations of each filter set. The clearest was that all of the highest performing sets of filters incorporated an antireflection coating on the highest bandgap multijunction cell rather than a short-pass filter. This is a clear indication that the short-pass filters featured intolerably high reflectivity at photon energies above the bandgap, even when the designed cutoff wavelength was shifted to wavelengths longer than the bandgap. The penalty associated with improperly reflecting a high energy photon is greater than the parasitic absorption imposed on low energy photons admitted into the highest bandgap multijunction. This is dependent upon the assumed parasitic absorption, and so some care should be taken to ensure the various layers of the highest bandgap multijunction are not strongly absorbing lower bandgap light. In addition to free carrier absorption, band-to-band absorption in cladding layers or contact layers needs to be carefully considered as well when designing the epitaxial structure of the multijunction devices. A second common feature of the highest efficiency designs was the absence of band-pass filters. long-pass filters for both the middle and bottom cell proved superior, despite their ready admittance of low energy photons into the middle cell. long-pass filters showed superior transmissivity in-band and reflectivity out of band than band-pass filters, and thus parasitic absorption of sub-bandgap photons is outweighed by the improved absorption of intermediate energy photons and avoiding thermalization of high energy photons in the middle cell. Also of note, the best performing long-pass filter for the bottom cell featured the greatest number of layers, which improved the total out of band reflectivity and therefore offered the greatest avoidance of thermalization losses of high energy photons. In contrast, the highest performing long-pass filter for the middle cell had fewer layers, which improved the in-band transmission. This is because the thermalization losses of high energy photons are not as great in the middle cell relative to the bottom cell, and similarly improper reflection is more costly since it operates at a greater voltage.

Finally, contrary to initial assumptions, the optimized geometries of each set of filters were ultimately very similar. The filters were far enough from ideality that there was only minimal preference shown for light trapping over concentration, or vice versa. The acceptance angle of the angle restricting hexagonal CPCs was between 10 and 15 degrees with output angles between 50 and 55 degrees. The acceptance angle offset was never greater than 1 degree in optimized designs, owing to the minimal skew ray rejection at such low output angles and the importance of preserving the angular budget for concentration and light trapping. These acceptance angles are compatible with a primary concentrating optic generating 450-500x concentration, a level well within demonstrated commercial high concentration photovoltaics and thus no burden for pointing or tracking accuracies.

2.4.4 System Performance and Losses

The angle-averaged reflectivity of the set of filters which had the highest efficiency is shown in figure 2.8, along with the resulting photon flux to each multijunction cell plotted against the AM1.5D standard solar spectrum. A module with an optimized LTFC receiver featuring ideal angle-insensitive top hat filters, a primary concentrating optic with 90% throughput, and perfect reflecting surfaces on the angle-restricting CPCs and inside the slab would have an optical to electrical power conversion efficiency of 46.8%. The quality of the slab cavity is strongly dependent on the reflectivity of the reflecting surfaces, and thus reducing the reflectivity of the angle-restricting CPCs and the surfaces of the slab from unity to a wavelength independent 98% results in a module efficiency of 40.6%. Finally, substitution of

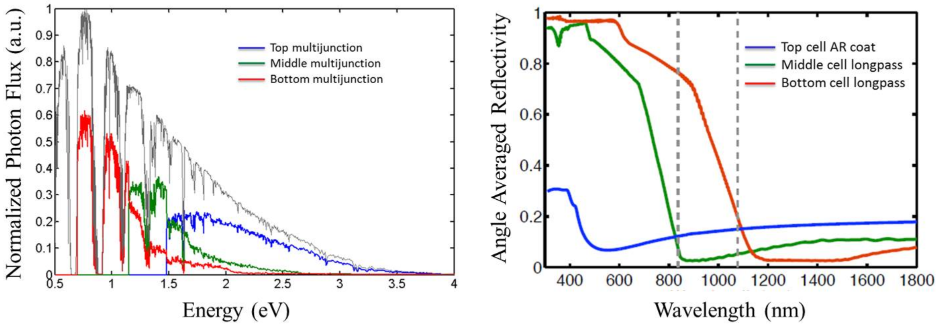

Figure 2.8: Left: Calculated photon flux to each of three multijunction cells coupled to the LTFC along with the AM1.5D solar spectrum. Right: Angle averaged reflectivity of the three multilayer dielectric coatings with the highest performance in an optimized LTFC receiver.

ideal filters with the best performing set of three designed filters further reduces the modeled module efficiency to 36.8%. An additional challenge is that the optimized set of bandgaps in the highest bandgap multijunction includes an absorber with a 2.31 eV bandgap. This is a difficult bandgap to grow a high quality photovoltaic device at, and restricting the highest achievable bandgap to 2.1 further lowers the attainable efficiency to 35.5%.

2.5 Conclusions

This work demonstrated a spectrum splitting receiver design that incorporated eight photovoltaic bandgaps across three multijunction devices with a maximum attainable STC module efficiency of 46.8%, and 35.5% when limited to currently attainable materials and optical filters. This design would exceed the record concentrating photovoltaic module efficiencies, and would exhibit the additional benefit of reduced losses imposed by current matching because each multijunction would have its load tracked independently. Additionally, there is a strong reason to believe the thermal load on the photovoltaic cells would be less, since the thermalization losses are much less than in a three or four bandgap multijunction device. Optical losses in the system are greater, but all else being equal a unit power of light not absorbed is preferable to a unit power of minority carrier thermalization, because the latter increases the temperature of the photovoltaic and reduces its conversion efficiency while the former exits the system. However, the thermal benefits of spectrum splitting are not as great as in other lateral splitting designs where cells are separated laterally allowing more efficienct heat spreading and extraction. Improvements in omnidirectional filters could significantly boost the attainable efficiency of an LTFC module. The effect of angle-averaging on the aperiodic dielectric stacks is a transition width between reflecting bands and transmitting bands on the order of 100-200 nm, which is too broad for efficient spectral allocation. Future improvements in high contrast gratings and meta-surfaces should be considered for incorporation in an LTFC receiver. Similarly, photonic solutions for broadband angle-selective coatings would be desirable over the microfabrication of geometric angle restricting CPCs.

Chapter 3

OPTOELECTRONIC DESIGN OF POLYHEDRAL SPECULAR REFLECTOR

3.1 Introduction

Dichroic mirrors are optical filters with high transmission in some spectral region and high reflection in other spectral regions. Created from multilayer stacks of thin films with different indices of refraction which give rise to constructive and destructive interference of incident light, they have the capability of very starkly different spectral transmission properties with narrow spectral transition width. Spectrum-splitting solar module designs incorporating dichroic mirrors have a long history owing to this property.

In this work we examined a number of variations of spectrum-splitting modules involving dichroic mirrors, and we refer to them collectively as polyhedral specular reflector (PSR) designs [31]. The name polyhedral specular reflector derives from several key characteristics. First, that all of the designs explored involved optical paths in polyhedral solids to avoid the Fresnel losses that would accompany the many air-solid interfaces in a spectrum-splitting module with seven spectral bands if the filters were not embedded in a solid. Second, the reflections off of filters and the total internal reflection of the solid optic must remain as specular as possible to retain the preferred geometric path and conserve the angular budget of the incident beam. Finally, obviously reflector refers to the transmission/reflection nature of the dichroic mirrors, in contrast to splitting optics that steer a beam rather than split it between reflection and transmission.

In this chapter I describe the design space of dichroic mirror based spectrum-splitting modules. Then I examine in more detail the choices made for the optoelectronic design to be prototyped in an attempt to realize the high potential efficiency of this family of designs. This includes the selection of seven single-junction photovoltaic cells and the most suitable materials to create them with. Additionally, the electronic design of the photovoltaic cells using a one-dimensional device physics solver is described. Next, the incorporation of optical concentration via two stages of geometric concentrators, both before and after the spectrum splitting optics is discussed. Finally, the optical design of the dichroic mirrors is reviewed for completeness.

3.2 Polyhedral Specular Reflector Architectures

The nature of dichroic mirrors requires that an incident beam of light is split, with one portion of the beam transmitting through the mirror and one portion of the beam reflecting off of it. Dichroic filters can be designed in several configurations, including both short-pass (shorter wavelengths transmitted, longer wavelengths reflected) and long-pass (longer wavelengths transmitted, shorter wavelengths reflected). Additionally, band-pass filters allow a spectral band to transmit while reflecting wavelengths longer and shorter than the band edges, while band-stop filters reflect a spectral band while allowing wavelengths longer or shorter than the band edges to transmit. The type of filter used in a PSR design will dictate the order and placement of the filters and their matching photovoltaic cells.

The geometric configuration of the filters determines whether the reflected beam or transmitted beam is directed to a photovoltaic cell for absorption, and this is independent of the choice of long-pass or short-pass filters. Figure 3.1 depicts several architectures of PSR designs incorporating long-pass filters or short-pass filters in reflection or transmission mode.

3.3 PSR Design for Prototyping

The ultimate optical design which was selected for prototyping involved a series of seven long-pass filters, arranged from high to low bandgap cutoff in a vertical arrangement. The selection of long-pass filters, in place of band-pass or short-pass filters, due to the much higher out of band transmission achieved in candidate filter designs. short-pass and band-pass filters tended to have harmonics out of band which significantly reduced their achievable splitting efficiency.

The choice of long-pass filters drove the choice of the geometric configuration of the filters in a vertical arrangement, as it was desirable to place the highest bandgap photovoltaic cells earlier in the optical path. This is because the operating voltage of each cell is directly proportional to its bandgap, and as the currents are roughly similar, the contribution of each cell to the total module power production scales with the bandgap. Therefore, as optical losses due to interfaces or defects accumulate along the optical path of the splitting optic, it is advantageous to place the filters and their cells in descending order of bandgap.

The configuration of filters embedded in a solid optic and reflecting spectral bands 90 degrees to the side via a 45 degree orientation means that the incident beam strikes the filters around 45 degrees of incidence. At non-normal incidence of interference

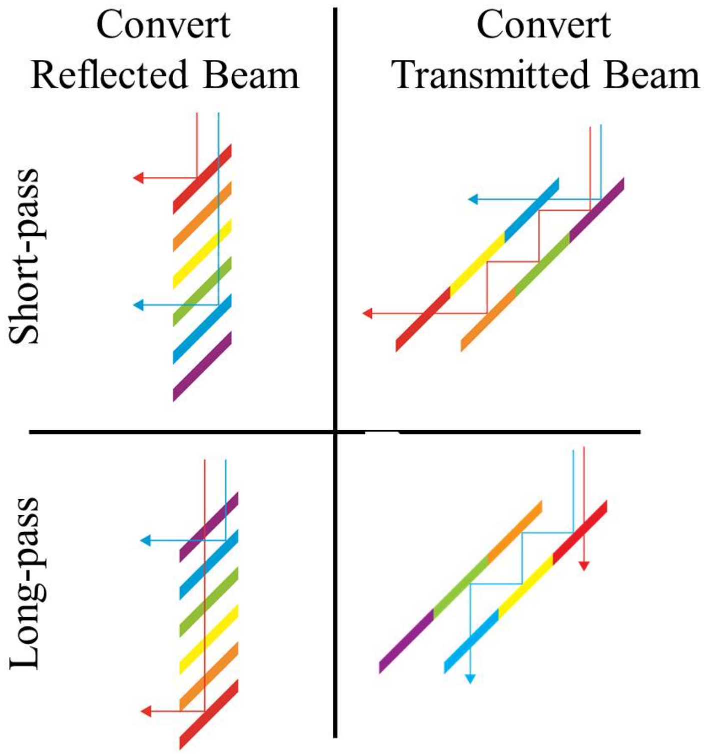

Figure 3.1: Variations in possible architectures within the polyhedral specular reflector (PSR) family of spectrum splitting designs.

based filters, the cutoff wavelength for each polarization of light differs, reducing the sharpness of the splitting somewhat.

An additional source of misallocation of photons comes from the fact that the cutoff wavelength of the dichroic filters shifts as the polar angle of incidence changes away from the design angle of 45 degrees. Although the disc of the sun subtends an angular width of only 0.25 degree half angle, when one considers the impact of a primary optical concentrator concentrating light into the splitting optic, the angular width of the beam increases along with the extent of concentration. This is necessitated by thermodynamics [32] and the smallest attainable increase in the angular width for a two-dimensional optical concentrator is given by equation 3.1.

$$\theta_{Out} = \arcsin \sqrt{C * \sin^2(\theta_{in})} \tag{3.1}$$

This introduces a trade-off between the extent of primary concentration and the attainable module efficiency. Higher primary concentration is desirable because it increases the power delivered to each repeating submodule unit, effectively reducing the cost of those units on a power or areal basis. However, the increased angular width of the beam exiting from the primary concentrator is less efficiently allocated between the seven spectral bands, lowering the power conversion efficiency.

A partial solution is found by incorporating optical concentration in two stages: a primary stage before the splitting optics, and a secondary stage between the splitting optic and the cells. This allows the cells to gain the cost and efficiency benefits of high optical concentration, while reducing the angular width of the beam incident on the splitting optics. The trade-offs between primary and secondary concentration are discussed further in subsection 3.4.3, along with candidate optical designs for the concentrators.

3.4 Bandgap Ensemble

As demonstrated in chapter 1, a spectrum splitting module capable of achieving greater than 50% power conversion efficiency must have at a minimum photovoltaic cells at six different bandgaps, and realistically seven. This fact drove the choice of seven spectral bands pursued in this work, and in order to possibly achieve such high efficiencies, the optimal ensemble of bandgaps with attainable materials is necessary.

Dr. Emily Warmann performed exhaustive calculations to determine the optimal combinations of bandgaps in spectrum-splitting ensembles containing up to 20 different electrically independent photovoltaic cells [33]. In order to search such a large design space, random ensembles were generated and a Monte Carlo optimization method known as simulated annealing was used to perturb and evolve the highest performing set. The merit function for the optimization was the sum detailed balance efficiency of the constituent cells in the ensemble. This optimization is described in detail in her doctoral thesis, and the reader is encouraged to consult it for a richer description of the numerical methods involved.

The seven bandgap ensemble that resulted from this optimization is described in table 3.1, along with the suggested alloy compositions exhibiting said bandgaps. Additionally, several of the bandgaps were adjusted slightly through negotiations with the epitaxial grower, but it should be noted that the optimum ensemble is broad, and small perturbations do not strongly affect the maximum attainable efficiency. This is easy to understand, for example, in the case of 1.84 eV InGaP being reduced to 1.78 eV. The photons falling between 1.84 and 1.78 eV now suffer much less thermalization losses, as they are absorbed near the band edge of this cell rather than more than 200 mV above the band edge of the next cell down. However, the rest of the photons in the spectral band between 1.84 and 2.15 eV suffer an additional 60 mV of thermalization loss. To first order, these two effects cancel, and the maximum efficiency is mostly unchanged.

Optimal Bandgap	Adjusted Bandgap	Absorber Alloy	Growth Substrate	Designed ERE
0.74 eV	0.74 eV	InGaAs	InP	11%
0.93 eV	0.93 eV	InGaAsP	InP	1.6%
1.15 eV	1.15 eV	InGaAsP	InP	1.2%
1.42 eV	1.42 eV	GaAs	GaAs	22.5%
1.58 eV	1.54 eV	AlGaAs	GaAs	3%
1.84 eV	1.78 eV	InGaP	GaAs	8%
2.15 eV	2.10 eV	AlInGaP	GaAs	0.19%

Table 3.1: Ensemble of bandgaps as designed and as grown, along with their suggested alloy, their growth substrate and the targeted ERE.

Three modifications to the optimal ensemble were made through discussions with Spectrolab. First, the top cell bandgap would ideally be at least 2.15 eV, but as material quality degrades with the incorporation of Al which raises the bandgap, the decision was made to pursue a cell with the highest open circuit voltage possible rather than pursue a nominal bandgap. This resulted in a 2.10 eV cell being developed, even though the first filter cutoff was designed at 2.15 eV. Second, the bandgap of the 1.84 eV cell was lowered to 1.78 eV. As described, this had a negligible impact of maximum efficiency, and was done due to Spectrolab's greater experience with growing ordered-InGaP devices. Finally, the 1.58 eV bandgap was lowered slightly to 1.54 eV to balance the photocurrents after the previous two adjustments.

3.4.1 Electronic Design of Photovoltaic Cells

The devices reported on in this work were fabricated from epitaxial growths by Spectrolab Inc. in collaboration under an ARPA-E 2012 Open FOIA award. The epitaxial growths were performed on a best-effort basis according to device performance targets generated by Caltech, and their electronic designs were proprietary to Spectrolab. In order to develop appropriate device performance targets, one-dimensional device models which had been developed prior to beginning th collaboration were utilized. Single-junction devices were designed by Caltech and grown by a commercial III-V foundry, Sumika Electronic Materials. These growths were not used directly in the fabrication of prototypes discussed in chapter 5, but they did play two important roles in this effort. First, they offered a learning experience and platform to understand the likely design of the Spectrolab devices, whose precise layer compositions, thicknesses, and doping profiles were kept confidential. Second, they offered test platforms to help develop Ohmic contact schemes and wet etch processes, including epitaxial lift-off, thus sparing the Spectrolab growth material. As such, a brief description of the electronic device design is offered here. Dr. Emily Warmann led this effort, particularly helping to correspond available data about radiative and non-radiative lifetimes to realistic parameters for simulation, and was assisted in designing the ensemble of devices by myself, Dr. Carissa Eisler, Dr. Matthew Escarra, and Dr. Cris Flowers.

In designing the single-junction III-V devices, first the alloy compositions were chosen for each bandgap. The composition was constrained by the requirement of lattice matching an available growth substrate, namely InP or GaAs wafers, to offer potential for high-quality epitaxial growth. One of the bandgaps was at 1.42 eV, accessible with binary GaAs. For ternary alloys, there generally exists only a single lattice matched composition. For instance the lowest bandgap cell composition is $In_{0.48}Ga_{0.52}As$, lattice matched to InP. However, for AlGaAs alloys, the fortuitous similarity in lattice constant between AlAs and GaAs allows a wide range of compositions and bandgaps to be grown at essentially the same lattice constant. Finally, for InGaP, at the lattice matched composition the bandgap can be tuned via ordering on the group III lattice sites, which is controllable through growth conditions. This leaves just three quaternary allows. The composition of the quaternary alloys, at 0.93, 1.15, and 2.10 eV, was fixed by the lattice matched composition that gave the required bandgap. The functional dependence of the lattice constant and bandgap on the alloy composition was taken from literature reports [34], and the solution of this system of two equations provides the desired composition.

Material properties of these alloys were collected from literature reports, and one-dimensional device physics models using the freely available device physics solver AFORS-HET [35] were built to optimize the device design. The seven resulting device structures are included in [33], but generally they all shared the following commonalities. First, they were designed as conventional, upright pn-junctions, either n^+p or p^+n. Second, they all featured wide bandgap cladding layers at the front and rear, referred to as the window and back surface field. These cladding layers act to limit minority carrier recombination and raise device voltages. Next, both front and rear cladding layers are connected to heavily doped contact layers, generally lower bandgap for ease of forming Ohmic contacts. These contact layers can be selectively removed everywhere except underneath metal contact features so as to avoid parasitic optical absorption while still performing their electronic role.

Some care needs to be taken in designing the appropriate cladding layers. An ideal window or BSF has an appropriate band alignment to allow majority carrier transport across itself while limiting minority carrier transport. Additionally, the bandgap of the window and BSF should be wide enough so as to not absorb light of that devices spectral band, since carriers generated in the window and BSF are not efficiently collected. The cladding layers also need to have certain chemical compatibilities for device processing. A selective etch is necessary to remove the front, rear, or both contact layers in places without removing the cladding layer. Fortunately a wide variety of selective wet chemical etches are known in the III-V material system. For the lower bandgap ternary and quaternary devices to be grown on InP substrates, InP or InAlAs are good candidates for cladding layers that are resistant to etches used on InGaAs, which is a useful low bandgap contact layer material. For devices grown on GaAs substrates, AlGaAs, InGaP, and AlInP can all be suitable cladding layers with GaAs contact layers depending on the composition of the absorber. High Al content AlGaAs, however, should be avoided as it would not be compatible with the hydrofluoric acid epitaxial lift-off process.

A typical band diagram with the device layers identified for one such designed device, the 1.42 eV GaAs cell, is shown in figure 3.2.

Optimization of the Top Electrical Contact Grids

The top electrical contacts of a solar cell perform an electrical role in competition with an optical role. They extract current from one terminal of the photovoltaic cell but they also obscure the optically absorbing active area of the cell from incident illumination. Although there have been demonstrations of methods to reduce this shadowing loss, either by incorporation of an optical element above the contacts [36] or by structuring the metal grid lines of the contacts [37], absent such efforts the metal coverage represents an essentially linear loss of efficiency on a photovoltaic cell. If the grid lines are to thin or too sparsely placed, however, resistance losses accumulate and degrade the device efficiency. Therefor, the optimal contact grid will balance the competing losses of shadow fraction and series resistance.

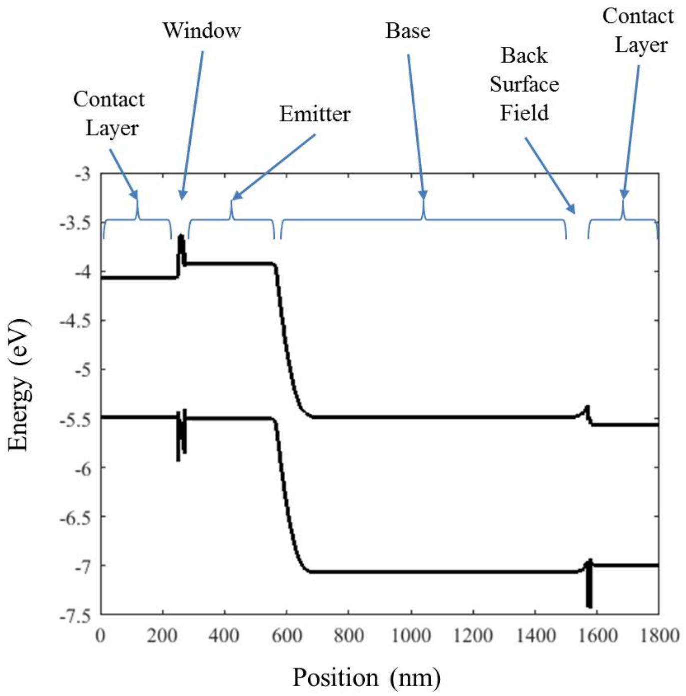

Figure 3.2: Band diagram of a p^+n-GaAs with constituent device layers identified.

In order to design the optimal contact grids for devices in this work, Dr. Cris Flowers constructed an electrical model in HSPICE that numerically optimized the grid design by balancing these twin loss mechanisms. Cells were modeled as unit area diodes with current generation sources where not obscured by a metal grid element. The effective series resistance is calculated from the network of elements, and results from contributions from the sheet resistance within the emitter layer, contact resistance into the metal, and line resistance of the metal fingers. The details of that calculation are available in Dr. Flowers doctoral thesis [38]. The resulting design offered an optimal number of equally spaced fingers arranged in an inverted square pattern for a given photocurrent, characteristic cell resistances, and metal grid width and thickness.

3.4.2 Filter Optical Design

Having selected the optimal bandgap ensemble and the splitting architecture as cascading long-pass filters, the optical design of the filters themselves can be addressed. Dr. Carissa Eisler designed a set of six filters made from aperiodic multi-layer stacks of TiO_2 and SiO_2 using the open source transfer matrix method software OpenFilters. This set of filters had an optical splitting efficiency of 93%, which is defined as the ratio of power converted by the seven photovoltaic cells under the split spectrum to the power converted by the same cells in a perfectly split spectrum. In both cases the power converted by the cells is determined by a modified detailed balance model.

As each filter in this ensemble features up to several hundred alternating thin layers which sum to several tens of microns thick in total, their fabrication would be somewhat challenging in a multi-user laboratory environment. Fortunately, commercial vendors with excellent process control provide the opportunity to outsource the fabrication of these filters. Chroma Technology was contracted to fabricate the long-pass filters, and in collaboration with Dr. Eisler, they developed a design featuring alternating layers of SiO_2 and either Ta_2O_5 or Nb_2O_5 to be deposited on parallelepiped pieces of Corning 7980 fused silica. These parallelepiped pieces with two square faces, two rectangular faces, and two rhombohedral faces, along with a triangular prism for the top of the stack, could then be joined into a single solid splitting optic just as modeled.

3.4.3 Primary and Secondary Optical Concentration

There are several design priorities that would drive the optimal design towards higher primary concentration. These include reducing the count and areal requirements of the elements under concentration, primarily the cells and filters. Additionally, higher primary concentration reduces the number of subunits per unit area, and thus strongly affects system costs. Finally, high optical concentration at the cells is necessary to achieve high efficiencies for thermodynamic reasons. There are two optical loss mechanisms, however, that come along with primary concentration. These are the angular response of the dichroic filters and geometric losses from spreading of the specular light path. A compromise is found in two-stage concentration, with a primary concentrator prior to the splitting optics, and secondary concentrators applied to each spectral band. This provides higher optical concentration on the cells while limiting the angular width of the beam incident on the filters. The efficiency of optimized point designs featuring primary and secondary concentration are shown in figure 3.3, with the secondary concentration noted in parenthesis along each data point.

Primary and Secondary Compound Parabolic Concentrators

The design of the geometric optics for the PSR was performed using commercial ray tracing software, LightTools by Synopsis. Dr. Carissa Eisler built a model that

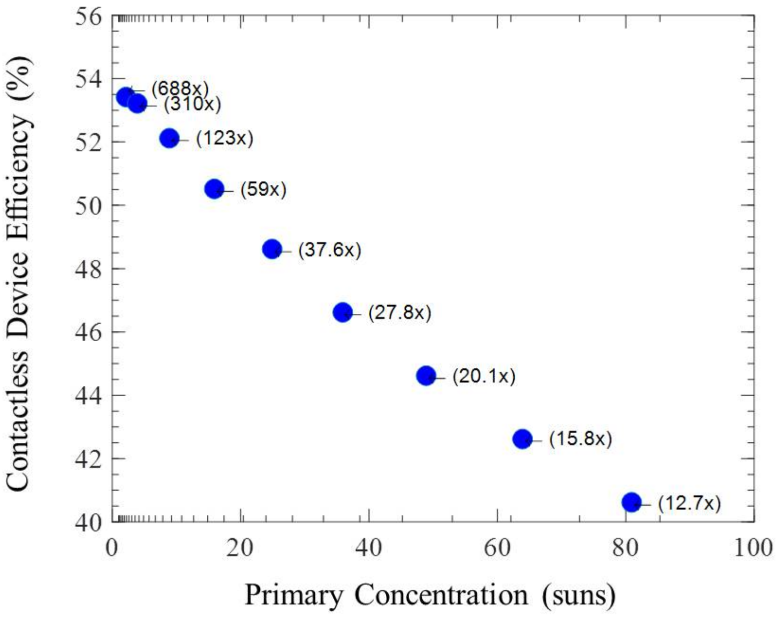

Figure 3.3: Efficiency of a PSR with two-stage CPC concentration. Extent of secondary concentration is noted for each point design in parenthesis.

incorporated the optical properties of the filters, and utilized two stages of optical concentration. These were a hollow reflective compound parabolic concentrator (CPC) as the primary concentrator, and solid glass CPCs utilizing total internal reflection as secondary concentrators. The aspect ratio of CPCs can become quite large with concentration, particularly for CPCs with restricted output angles, and thus the truncation of the CPCs was a design parameter. This afforded significant solid volume and cost savings at the expense of concentration levels.

Light Pipe Secondary Concentrators

Owing to the impossibility of acquiring square profile CPCs made of fused quartz, straight-walled light pipe concentrators were substituted in their place as secondary concentrators. One-dimensional trough CPCs are ideal non-imaging optical concentrators, transmitting all incident optical power incident on the input face within the designed acceptance angle out through the output face within the acceptance angle. When they are extended to two-dimensional shapes, either with circular, square, or other polygonal profiles, they deviate slightly from ideality. In these two-dimensional CPCs there exist skew ray paths within the acceptance angle that are rejected, leading to less than the thermodynamic limit of optical concentration, and requiring a slightly larger acceptance angle for optimal radiative power transfer. Despite these skew rays, though, the transmission efficiency of incident light retains a relatively sharp cutoff around the designed acceptance angle.

For straight-walled light pipes, one can imagine what the incident beam “sees” when it strikes the input face. At those positions and angles where rays are aimed directly at the output face, they transmit without being perturbed. Every other ray will proceed until it strikes a sidewall, at which point it is reflected inward and its direction cosine is increased by twice the angle inclination of the sidewall. Imagining all these reflected rays then, that portion now aimed directly at the output face is transmitted without further reflection, while all other rays repeat the reflection off the sidewall. This process repeats over and over, ratcheting up the angle about the optical axis of reflected rays by twice the angle of inclination of the sidewalls. It is then understandable why the angle of the sidewalls, which correlates directly to the length of the light pipe for a given geometric gain, dictates the sharpness of the transmission efficiency with angle. The smaller the angle of the sidewalls, that is, the longer the light pipe, the smaller the angular ratchet, and the fewer rays are ratcheted past the output face and back out the top of the light pipe. A straight-walled light pipe can be adiabatic in the limit of infinite length, gently squeezing a beam of light into a narrower spatial extent while increasing the angular width infinitesimally.

The trade-off between the length and acceptance angle then of a straight-walled light pipe for a given geometric gain is depicted in figure 3.4 Ultimately, two point designs were selected for prototyping. They were a 16x light pipe 25 mm in length with a 2.5 mm wide square output face, and a 100x, 100 mm long light pipe with a 1 mm wide square output face.

Fresnel Lens Primary Concentrator

In ray-optical simulations a reflective walled square profile CPC was used as a primary optical concentrating element. This type of optical concentrator offers many design advantages, including minimizing the angular width of the concentrated beam and avoiding the Fresnel losses associated with refractive optics. However, there are several significant drawbacks to using CPCs as primary concentrators in an actual system. First is that even with truncation CPCs have a very large aspect ratio. This is directly related to the low angular width of the output beam for a given concentration, but unfortunately it requires a significant amount of material, even

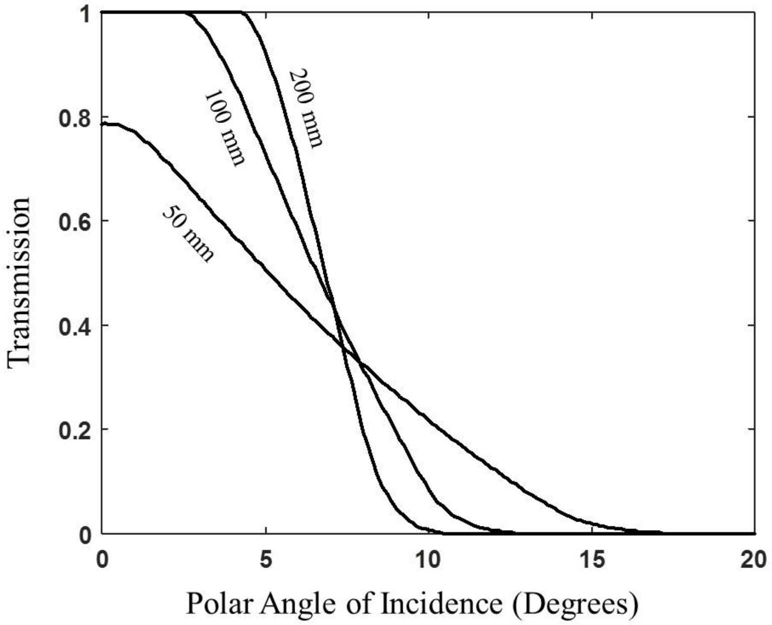

Figure 3.4: Transmission through straight walled light pipe 100x concentrators of several lengths as a function of incident polar angle.

for a hollow reflective CPC, due to the large surface area. Next, a reflective CPC deployed outdoors would certainly need a coversheet to prevent it from collecting dust, debris, and water. This coversheet would then present two air-solid interfaces with their concomitant Fresnel losses, negating that benefit of a reflective optic. Finally, a large primary reflective CPC would likely need some degree of mechanical coupling to the splitting optic, whereas a refractive optic is physically isolated and need only maintain registry of the focal spot.

For these reasons, an effort was made to design a refractive primary optic to demonstrate the feasibility and performance of a PSR under a more conventional optical concentrator. Towards this end several plano-convex and Fresnel lenses were designed to mimic the performance of certain PSR top concentration point designs. Single-zone lenses were utilized for simplicity as the secondary concentrators provide an illumination homogenization function. Furthermore, although nonimaging Fresnel lenses utilizing prisms of minimum deviation [39] are most efficient with the angular budget of incident light, the front face was designed here as flat to better mimic the Fresnel lenses deployed in commercial concentrating photovoltaic systems.

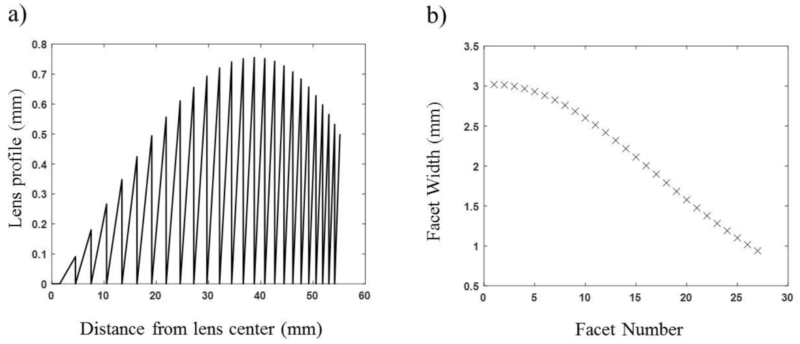

Figure 3.5: Example profile of a single-zone non-imaging Fresnel lens. The profile of the facets is depicted on the left, and the width of each facet is plotted on the right.

Code was written in MATLAB (included in appendix) to calculate the facet profile of an extruded non-imaging Fresnel lens with a constant index of refraction for simplicity. This was done by setting the height of the lens and the angular width of the incident beam as inputs, and then sequentially calculating the edge rays of each facet. For instance, working from the center outward, first the half-angle of the incident beam was projected onto the focal length. For a given incident angular width there is a maximum focal length where the projected edge ray falls within the desired 1 cm wide aim spot representing the input face of the splitting optic. This first flat facet is extended until the edge ray strikes the edge of the aim spot. The angle of inclination of the next facet is then calculated from the geometry that aligns the other edge ray with the opposite edge of the aim spot. This inclined facet is then extended until the first edge ray again reaches the edge of the aim spot, and the process is repeated. As the facets are inclined at greater angles they become narrower due to the increased divergence between the edge rays owing to the non-linearity of Snell's law. An example lens profile along with a plot of the width of its facets is shown in figure 3.5.

Through this calculation, a design surface was identified that corresponds the highest optical concentration attainable without geometric losses to the focal length of the Fresnel lens and the angular width of the incident beam. The angular width of the output beam is mapped onto this surface, depicted in figure 3.6. For primary CPCs an incident beam with a 1.8 degree half angle was assumed to allow for the angular width of the sun and tracking tolerances with large reflective optics. For Fresnel lenses, we can assume a tighter tracking tolerance and assume an incident beam of

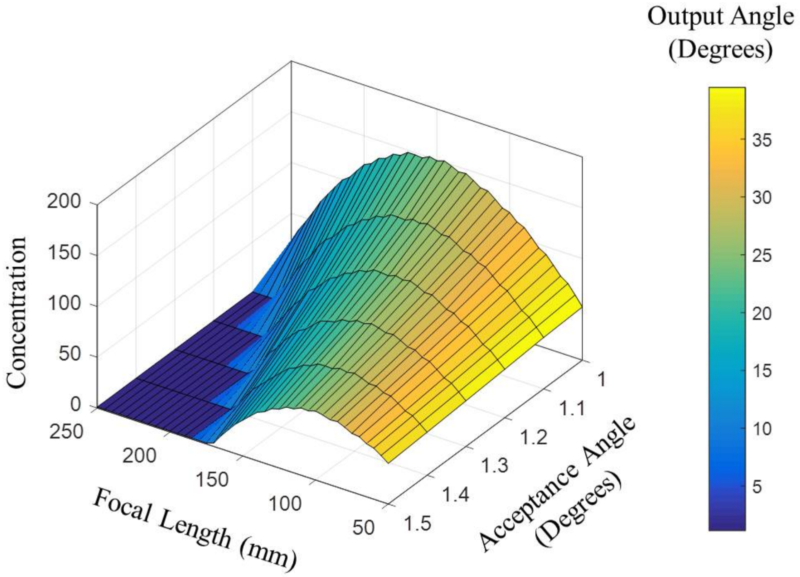

Figure 3.6: Design space of non-imaging Fresnel lenses demonstrating the relationship between the focal length, acceptance angle and geometric concentration. The angular width of the resulting beam is color mapped upon this surface.

1 degree half angle, reflecting the tolerances of deployed commercial systems. This allows us to design Fresnel lenses with very similar optical characteristics to the otherwise superior CPCs.

This surface provided a starting point for designing an aspheric Fresnel lens. A point design incorporating a CPC with 81x and 16.4 degree output angle was chosen for replacement with a Fresnel lens. The design surface from figure 3.6 offered an initial design point for optimization. A ray trace model was constructed in Synopsis LightTools that placed a plano-convex acrylic lens at the distance from the splitting optic input face as indicated by figure 3.6. The aspheric coefficients of this lens were then optimized via a gradient ascent method to maximize broadband power throughput onto the input aperture. These aspheric coefficients were then used to generate a Fresnel lens with aspheric facets, and the distance from the receiver was perturbed to maximize the throughput on the receiver. This perturbation corrected somewhat for the conversion from a plano-convex aspheric lens to a Fresnel lens, and chromatic aberration from acrylic not considered when designing the non-imaging Fresnel lenses.

The optimized replacement single-zone 81x Fresnel lens is depicted as ray traced

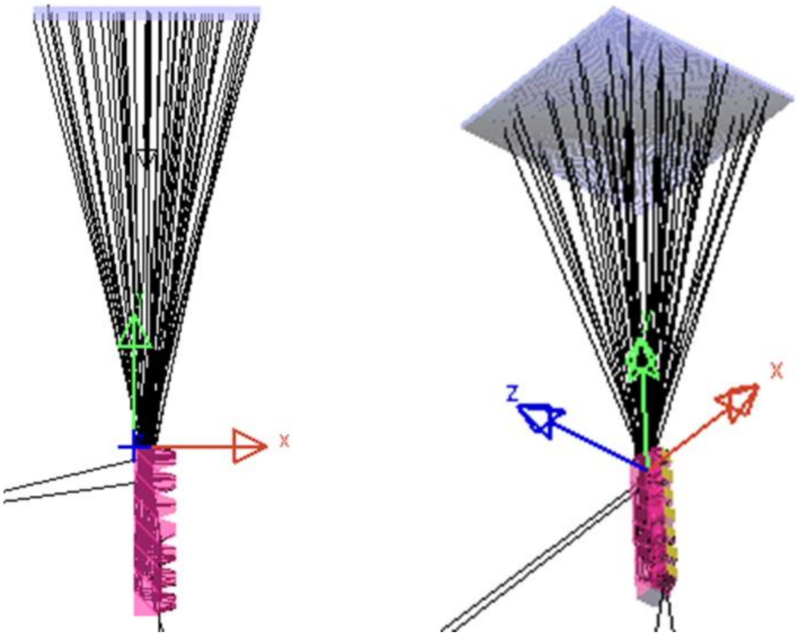

Figure 3.7: Ray trace model of 81x single-zone Fresnel lens shown from two perspectives.

in figure 3.7 and had the following performance characteristics. At a focal length of 190 mm and a minimum acrylic thickness of 3 mm as required by mechanical constraints, 90.8% of incident power was transmitted to the splitting optic input. The primary loss was 7.8% absolute from two Fresnel reflections, and an additional 0.25% absolute was volumetric absorption in the acrylic. The output beam was nearly uniform in intensity out to a half angle of 14.7 degrees. The irradiance and radiant intensity at the focal plane from this Fresnel lens is shown in figure 3.8.

A second point design with a higher geometric concentration, 90x, to match the total flux of an 81x reflective CPC lacking Fresnel losses was also considered. At a focal length of 178 mm and 16.4 degree wide output, this closely matched the performance of an 81x reflective CPC primary, and resulted in modeled module efficiency of 42.2% compared to 44.5% for the reflective CPC design without a coversheet. This is a strong indication that the replacement of a CPC with a more conventional refractive primary concentrating element does not materially change the system performance.

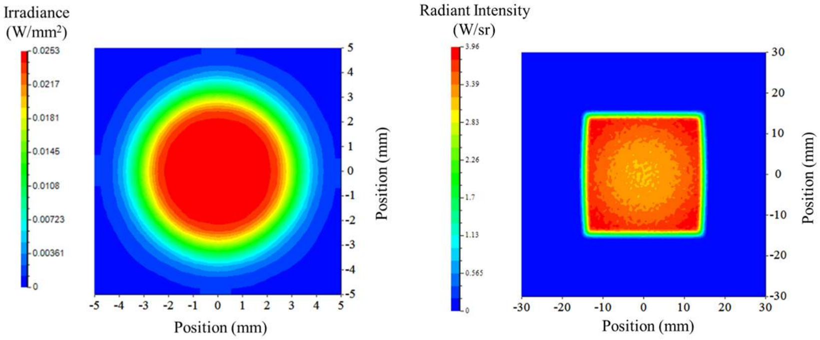

Figure 3.8: The irradiance (left) and radiant intensity (right) delivered to the splitting optics from the optimized 81x Fresnel lens on the input to the splitting optic.

Chapter 4

POLYHEDRAL SPECULAR REFLECTOR FABRICATION

4.1 Introduction

The polyhedral specular reflector (PSR) design ultimately emerged from an internal design competition as the spectrum splitting design with the highest realizable power conversion efficiency. Taking an optical design envisioned in a gravity free modeling environment, however, and reducing it to practice involved quite a lot of learning and effort. In this chapter I detail the process steps involved in fabricating the photovoltaic cells and integrating them with the optical system while managing all the mechanical, optical, and electrical coupling between components in the system.

4.2 Splitting Optic Fabrication

The optical splitting assembly for the polyhedral specular reflector spectrum splitting module consisted of seven individual optical elements attached sequentially. These elements included six parallelepiped pieces and a single triagonal prism piece, all fabricated from Corning UVFS 7980 fused silica. On one face of each element an optical coating was applied, including a metallic mirror on one of the parallelepipeds and the multilayer dielectric stack dichroic filters described in chapter 3 on the remaining six elements. Dr. Carissa Eisler led the efforts to fabricate the optical splitting structures, and those efforts are described in much greater detail in her doctoral thesis [40]. They are reviewed here briefly for completeness.

The seven splitting elements were sequentially attached to each other to form a single prism with embedded optical filters. This was done by dispensing 5 uL of polydimethylsiloxane (PDMS) on one face of an element and placing the adjoining face of the next element in contact. Prior to joining, the faces of the elements adjacent to the joining surface were covered in polyimide tape to as to prevent overspill of PDMS from covering them. The pieces were set on an alignment jig that held the stack in place while the PDMS was degassed in a vacuum desiccator under rough vacuum for 15 minutes and then cured in an oven at 80 °C for 40 minutes. Finally, a fused silica slide with a broadband anti-reflection coating purchased from Reynard Corporation was attached with PDMS to the input face of the splitting prism. Figure 4.1 shows the filters as deposited on parallelepipeds and a fully assembled splitting prism.

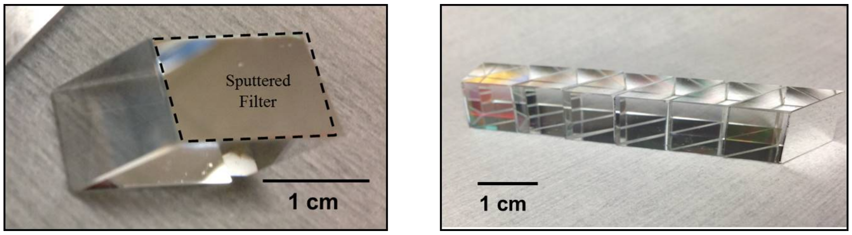

Figure 4.1: A single parallelepiped (left) with a multilayer dielectric stack deposited on one face (dashed black box) and a splitting prism (right) assembled from 6 such parallelepiped pieces and one triangular prism capping piece.

4.3 Thin Film Single-Junction Photovoltaic Device Fabrication

As described in chapter 3, III-V compound semiconductors are nearly an ideal material system for fabricating high quality single junction photovoltaics that convert narrow spectral bands of light as close to the thermodynamic limits as possible. This is owing to the large range of compositions that can be epitaxially grown in lattice matched configurations and released from their substrates thanks to the fortuitous etch selectivity of certain alloys. They are easily doped both n and p type, have direct bandgaps, and excellent internal radiative efficiency. They have benefited from decades of material growth and device development, and devices made from this material system hold records for the highest efficiency cells.

Epitaxial growth of III-V semiconductors is performed commercially by foundries and device manufacturers utilizing metal-organic chemical vapor deposition (MOCVD). This is a vaper phase epitaxy technique whereby metel-organic precursers are flowed over a growth substrate held at a process temperature. The precursers decompose and deliver atoms to the surface of the growth substrate, and by controlling the temperature, gas pressure ratios, and dopant gases a large number of alloy compositions with wide tunability of doping can be grown.

In order to benefit from the expertise gained via decades of commercial production, Spectrolab Inc. was partnered with as a collaborator to supply epitaxial growths of all seven single junction devices on a best-effort basis. The design and qualification of these growths is described in chapter 3, and here I describe how the bare wafers with epitaxial layers as-grown by Spectrolab were delivered to Caltech for device processing. The steps for processing these epitaxial growths into testable optoelectronic devices with highest possible efficiency is described in this section.

4.3.1 Rear Mirror and Electrical Contact

The final epitaxial layer that was grown on each device was a heavily doped p-type layer designed to allow an electrical contact to be formed with a deposited metal. This contact is required to be Ohmic in nature with a contact resistance small enough so as not to contribute significantly to the total series of the device. The first process in the fabrication of the photovoltaic devices from the epitaxial growths, then, is the creation of this Ohmic contact via thin film deposition of select materials.

The deposited electrical contact serves an optical function as well as an electrical one. It should be as reflective as possible for light at wavelengths corresponding to the absorber bandgap and shorter. This allows for the optimal photonic performance of a high radiative efficiency single junction photovoltaic device described in chapter 1. The absorber layers can be made thinner as reflected light has at least twice the optical path length as the absorber thickness. Similarly, luminesced photons cannot escape out the rear of the device, as they can in a device remaining on its growth substrate, reducing the radiative dark current.

One centimeter square wafer chips were the preferred size for processing devices, offering enough size to parallelize multiple devices and electrical test features while also being conservative with the limited available epitaxial material. However, the rear mirror depositions were performed on larger pieces so as to be efficient with thin film depositions. The epitaxial wafers were first cleaved into 2 x 3 cm pieces and those pieces underwent a surface cleaning procedure.

An epitaxial surface as free as possible from organic residue and surface oxides will ensure good adhesion and electrical contact. The cleaning procedure utilized in this work was common to both growths on InP and GaAs, and involved first a solvent rinse with acetone followed by isopropyl alcohol. After blowing fry with clean dry nitrogen samples were loaded into an oxygen plasma chamber and treated with an oxygen plasma so as to remove any remaining organic residue. A March Instruments PX 500 plasma tool was used for the oxygen plasma clean, with samples exposed to a 300 W plasma with a pressure of 300 mTor for five minutes duration.

Following the oxygen plasma treatment, samples were immersed for one minute in hydrochloric acid, diluted in the ratio 3:1 of deionized water:hydrochloric acid. Immediately following this surface oxide removal the wafer pieces were loaded into the vacuum chamber of an electron beam evaporator system for the deposition of the rear mirror.

The electron beam evaporation system exclusively utilized for this work was built by Angstrom Engineering and featured twin 6-pocket carousals from Telemark for electron beam evaporation as well as dual thermal evaporation pockets. Deposition rates were monitored via a quartz crystal monitor in real time and output power was PID controlled, with a shutter engaging to stop further material deposition after the desired thickness had accumulated. Tooling factors to calibrate the quartz crystal monitor signal to a thickness for each material was performed by evaporating a layer of material to a target thickness of 100 nm thick on a glass slide with a piece of polyimide tape to create a step edge, and then measuring the height of the step edge with a profilometer. The calibrated error of the profilometer was under 10 nm, resulting in a confidence in deposited thickness of at least 10%.

The formation of Ohmic contacts between heavily doped p-type GaAs and InGaAs is not challenging, and thus any number of metals directly deposited resulted in Ohmic contacts. For devices at all seven bandgaps, grown on either InP and GaAs, the rear mirror and Ohmic contact was formed by sequential deposition of a thin nickel adhesion layer followed by a 125 nm thick metal reflector. Ultimately gold was utilized in all devices fabricated for the prototype, because although it is not as reflective as silver at some wavelengths, its chemical inertness is desirable during wet chemical processing, particularly during the mesa edge isolation where the back mirror is exposed to corrosive agents.

Advanced Mirrors

In order to fully realize the efficiency potential of photonically optimized solar cells additional effort should be expended on enhancing the reflectivity of the back mirror and minimizing parasitic absorption [41]. In this work undesirably thick rear contact layers were grown which strongly absorbed band-edge luminescence and negated the benefit of photon recycling via the back mirrors.

Attempts were made at improving the reflectivity of the back mirrors by patterning electrical contacts and selectively removing the contact layer everywhere except directly above them. This is depicted in figure 4.2 in schematic form and by optical micrographs of a patterned contact layer in-filled with aligned SU-8 resist. Su-8 resist was chosen as a dielectric spacer layer for its chemical robustness to hydrofluoric acid during the epitaxial lift-off process, and if the layer was kept less than 1 μm the parasitic optical absorption in the SU-8 is minor. Infilling a dielectric material that could withstand the subsequent processing would serve

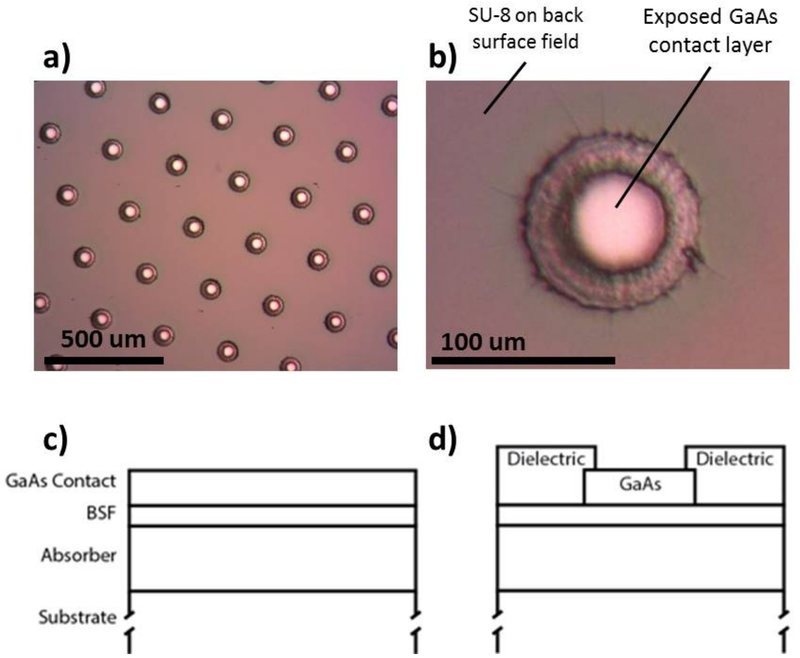

Figure 4.2: a) Optical micrograph of patterned array of GaAs contact pillars remaining after selective etching of rear contact layer and infilling with an aligned pattern of SU-8 photoresist. b) Closer inspection of a single pillar showing the overlapping SU-8 and GaAs with an exposed central area for electrical contact. c) Simplified schematic of typical inverted epitaxial growth before mirror processing. d) Simplified schematic of a cross section of a GaAs contact pillar following mirror processing.

the dual purpose of enhancing the reflectivity of the metal and preventing metal deposition directly on the back surface field where it might diffuse into the base and degrade the minority carrier lifetime. This work was not ultimately incorporated into the devices utilized in the integrated splitting prototypes as effort was focused on more significant loss mechanisms. However, improving the reflectivity of the back mirrors offers a pathway to extracting each excited carrier as close to its thermodynamic potential as possible.

4.3.2 Copper Handle Fabrication

After the deposition of an optically thick rear mirror, wafer pieces were cleaved into a working size of 1 cm x 1 cm. A thicker layer of copper was electroplated directly onto the rear mirror of those one centimeter square chips. This thick copper layer has several functions. It provides a mechanically robust handle to allow manipulation of the thin film devices following their separation from their substrates. It also provides a thermally and electrically conductive backside to minimize device series resistance and maximize heat spreading away from devices under concentration [42].

Samples were suspended from electrodes in an aqueous copper sulfate plating solution by clipping the corners of the samples with flat jawed alligator clips. One side of the alligator clip attached directly to the rear mirror, making electrical contact. The underside of the alligator clip which presses against the substrate was wrapped in polyimide tape to electrically isolate it from the substrate. This helped minimize plating on the substrate and helped improve the uniformity of the deposited copper film. The copper electroplating was performed with a Gamry Reference 600 galvanostat driving a current through a bath of copper electroplating solution, depositing copper ions on the sample. The copper electroplating solution was sulfuric acid based and sourced from Transene Company of Danvers MA.

The rear mirror serves a useful role here as a seed layer for the copper plating. The seed layer reduces the lateral resistance across the surface of the sample, thus reducing gradients in current density that give rise to non-uniform thickness or density of the copper. Plating was done slowly at first to build up the thickness while minimizing non-uniformity and the sample was rotated periodically to ensure complete and uniform coverage. The preferred process, resulting in a dense and uniform copper film approximately 50 μm in thickness is indicated below.

1. 5 mA/cm^2 for 10 minutes
2. Sample removed and alligator clip attached to opposite corner of sample (180 degree rotation)
3. 5 mA/cm^2 for 10 minutes
4. Sample removed and alligator clip attached to adjacent former (90 degree rotation)
5. 30 mA/cm^2 for 30 minutes
6. Sample removed and alligator clip attached to opposite corner of sample (180 degree rotation)
7. 30 mA/cm^2 for 30 minutes
8. Thorough rinse in deionized water

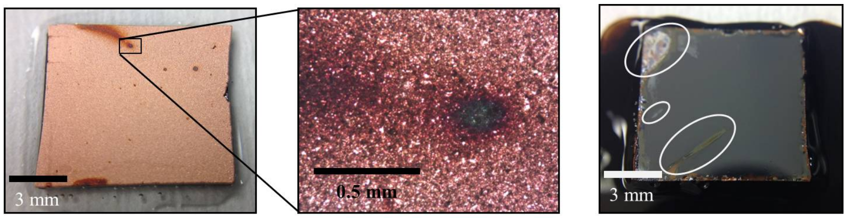

Figure 4.3: Left: A plated sample after soaking in water for 1 hour to expose pits caused by copper sulfate precipitated within the deposited copper. Center: Closer inspection of pit etched by sulfuric acid when copper sulfate dissolves during later aqueous processing. Right: Pits present in a lifted-off film due to the precipitation and subsequent dissolving of copper sulfate.

9. Blow dry with clean dry nitrogen

It should be noted that it is important to keep the copper sulfate concentration well below saturation, otherwise copper sulfate crystals will precipitate out of solution. These precipitates can prevent a dense mesh of copper, and more harmfully they will dissolve during subsequent aqueous process steps resulting in corrosion of critical device layers. This was observed in certain samples where the plating bath concentration became saturated. Small copper sulfate crystals that went unnoticed precipitated within the copper film. Despite the rinse in deionized water following plating, which lasted for nearly one minute, the precipitates remained in the film. The time scale associated with dissolving and diffusing out of the copper sulfate is greater than one minute, and thus it was only during the subsequent epitaxial liftoff step that the precipitates dissolved. When they did, the resulting sulfuric acid etched pits in the copper film and the GaAs epitaxial layers. This is seen in figure 4.3.

4.3.3 Mounting for Epitaxial Lift-Off

Although the copper film plated on the sample will support the epitaxial layers and its own weight after separation from the growth substrate, it is rather fragile and so prior to lift-off the samples were bonded to silicon wafer chips to protect the films and allow easy handling during device processing.

The electroplating process generally deposited material on the sidewalls of samples, which needed to be removed in order to allow exposure of sacrificial etch layers for epitaxial lift-off. Several techniques were investigated, including various masking strategies, and the preferred method is mechanically cutting away the copper film with a sharp razor blade. This was done by holding the blade at a 45 degree angle relative to both the sidewall and the epitaxial layers, and starting about a millimeter or so from a corner, drawing the razor blade along the edge to be exposed. It is important to apply pressure towards the substrate side with the blade, which results in a cleaner cut and also crucially prevents delamination of the rear mirror and attached copper film by avoiding tensile stress. Copper was removed from each of the four edges sequentially, and then the samples were flipped and the process repeated to remove the millimeter or so stretch of copper adjacent to each vertex which was not removed on the first pass in the other direction.

This mechanical removal of the copper is a delicate manual step, and care must be taken to avoid several failure modes. First, as described above, avoiding delamination of the rear mirror and copper film is crucial. If there is any degree of delamination the samples do not lift-off correctly. Second, although there will inevitably be some degree of damage to the III-V material along the edges, cracks or chips in the chip will generally make subsequent processing difficult and the sample should be discarded. Finally, it is important to fully separate the copper film from the substrate. If there is some remaining connection, then following epitaxial lift-off, when the substrate is pulled away from the film, it will pull on the epitaxial film. This pulling may induce cracks in the epitaxial layers, or separate the film from the wax mount (described in the following section). Any lifting up of the film reduces the planarity of the film and can makes subsequent photolithographic processing steps difficult.

Following the exposure of the sidewalls, the samples were mounted to their silicon-wafer carriers with Apiezon-W black wax. Silicon wafers were cleaved into 2 x 2 cm pieces. Identifying labels were scribed onto the silicon chips to prevent confusion while processing multiple samples in parallel. Wax was applied to the silicon chips by heating the chips on a hotplate to approximately 120 °C and spreading a bead of black wax around to cover an area greater than 1 x 1 cm. The samples were placed copper side down into the wax, and pressed down to minimize the thickness of wax. The samples were also moved back and forth to ensure a complete and uniform coverage of wax beneath the copper.

The samples were allowed to settle for thirty seconds and then removed from the hotplate. Excess wax was scraped away from the sidewalls with a razor blade. The samples were then returned to the hotplate until the wax began to flow again, and they were moved around the silicon to further spread and thin the wax. After removing from the hotplate again, the excess wax was again scraped from the

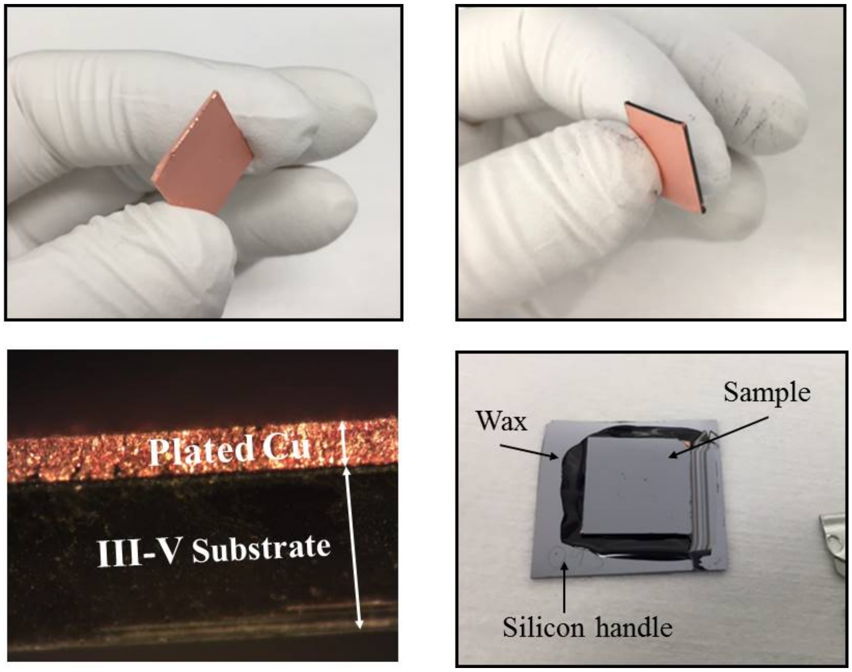

Figure 4.4: Top Left: Sample after copper plating with copper being removed from sidewall. Top right: Sample after having copper removed from all sidewalls. Bottom left: Optical micrograph of sample sidewall showing thickness of plated copper handle. Bottom right: Sample mounted on Si wafer chip with wax in preparation for epitaxial lift-off.

sidewalls. If necessary, this process was repeated until heating on the hotplate did not cause additional wax to flow out from under the sample. This ensured a thin and repeatable layer of wax which would not flow out from under the film during subsequent processing steps.

The sidewalls were carefully scraped with a razor blade one last time prior to epitaxial lift-off to ensure the sacrificial etch layer was exposed. Although wax was still visible in many places on the sidewalls, this physical cleaning proved sufficient for effective lift-off. Solvent cleaning was also explored, but this actually introduced additional challenged. For solvent cleaning, trichloroethylene was applied to fabric tipped plastic applicator sticks, and gently brushed along the sample sidewalls. This is effective in removing the wax, but it also tends to dissolve wax directly under the sample. This dissolved wax leaches out, and must be removed. It takes multiple iterative cleanings, and it is possible to remove too much wax from the edges of the sample to leave them unsupported, complicating subsequent processing. The mounting sequence for epitaxial lift-off as described here is depicted in figure 4.4

Additionally, solvent casting of the black wax in trichloroethylene was explored as an alternative to the thermal casting described above. This involved dissolving black wax in trichloroethylene and applying the viscous mixture to the silicon mounting chip. The sample is applied copper side down to the chip, and pressed into the wax. Excess wax is removed via physical scraping or solvent cleaning as before. Then the solvent must be allowed to diffuse out of the wax. Solvent casting allows a thinner resulting layer of wax, but the time associated with complete evaporation of the solvent via diffusion over five millimeters out to the edge of the samples is on the order of 10-20 hours. If the solvent is not fully removed, it will cause challenges during subsequent processing steps. If there is enough solvent in the wax, then during later processing steps involving heating it will volatilize and create bubbles underneath the film. These bubbles can rupture the film or cause cracks in the epitaxial layers. They can also cause undulations in the film which makes photolithographic processes less effective.

4.3.4 Epitaxial Lift-Off

The extreme (10^6) selectivity [43] of the etching in hydrofluoric acid of AlxGa1-xAs compounds where x> 0.35 over x< 0.35 has been known and exploited via epitaxial lift-off processes for decades [44]. III-V devices made from III-V epitaxial layers grown on GaAs can be fully released from their growth substrate by first growing a sacrificial high Al content AlGaAs layer on the order of 5-10 nm in thickness. Immersion in hydrofluoric acid etches the sacrificial layer rapidly, but the extreme selectivity prevents nearly any attack of the substrate or device layers even during the hours-long etch process. Once the sacrificial layer has been fully etched, the device layers are free from their growth substrate, which can be reused for additional growths so as to amortize the substrate cost over many more devices.

GaAs-based photovoltaic cells have been fabricated via epitaxial lift-off for more than two decades, and in fact presently hold the records for efficiency of single and dual junction cells [16]. This is not a coincidence. The thin film configuration presents the optimal optical design of a solar cell as described in detail in chapter 1. Epitaxial lift-off allows the potential for low-cost high-efficiency single-junction III-V solar cells, and even though in this work the substrates were not reused for additional growths, we believed it to be an important demonstration to fabricate all seven bandgaps via a scalable epitaxial lift-off process rather than substrate removal.

Once samples have been mounted to silicon carriers and their sidewalls cleaned, they are ready for epitaxial lift-off. For the seven different bandgap devices grown for this project, the four highest were grown on GaAs and the three lowest on InP. These substrates have different lattice constants, and so slightly different epitaxial lift-off processes were used. Epitaxial lift-off from GaAs was already well described, but epitaxial lift-off from InP substrates had a much sparser history.

Epitaxial Lift-Off from Gallium Arsenide Substrates

Devices grown lattice matched to GaAs were grown on ELO layers 5 nm thick of $Al_xGa_{1-x}As$ where x is approximately 0.90. There are reactor durability reasons to prefer the incorporation of at least a small amount of Ga in the liftoff layer, although the binary AlAs would work as well since the lattice constant is so close to GaAs and the layers are so thin.

Once samples were mounted on silicon wafer chips for handling as described in the previous subsection, they were immersed in an ELO etch consisting of equal parts by volume 48% hydrofluoric(HF) acid and ethanol. The most common etching solution for GaAs epitaxial liftoff is 10% hydrofluoric acid, and it has been reported that at higher concentrations of acid the higher rate of hydrogen production results in the formation of bubbles that clog the etch channel and prevent the diffusion of reactants and products, stalling the etch. There are also reports that adding alcohol serves as a surfactant, preventing the formation of hydrogen gas bubbles and allowing higher hydrofluoric acid concentrations and thus faster etching. This was not studied in detail in this work, however based on data acquired while developing the process, it was determined that the 1:1 by volume mixture of concentrated HF acid with ethanol appeared to more reliably lift-off films in an expected duration of 12-24 hours than the 10% hydrofluoric acid solution.

Samples were etched for at least 12 hours and generally 24 hours in a PTFE beaker with the etchant. This was kept in a closed wide-mouth polypropylene jar for secondary containment, to prevent contamination and for safety reasons in a multi-user environment. After the etch period, samples were removed from the etchant and rinsed by sequential immersion and agitation in three PTFE beakers of deionized water. Following the rinse, the handle attached to the substrate was gently pulled to separate it from the thin film. If the substrate did not detach with gentle pulling, it was dried with nitrogen and observed to ensure the sidewalls were properly cleaned and exposed, and then it was placed back in the etchant for an additional period of etching.

This physical separation of the substrate proved to be hazardous for the samples. In a minority of samples the substrates detached easily while the samples were being immersed in water for rinsing. However, in a majority of samples a small amount of force needed to be applied to detach the substrate, owing to the surface tension of the liquid-filled etch channel. If the etch had not completed entirely, however, the applied force could tear the small area of un-etched epitaxial material. This resulted in a tear in the film, lowering the yield of high-quality devices. Additionally, in some cases the etch had completed entirely but there existed some region along the edge where plated copper had not been completely removed, and remained continuous between the substrate and the epitaxial film. This most often occurred around corners, particularly if the corner was damaged during cleaving and the mechanical removal of the plated copper was hindered. In these cases, when the substrate was pulled apart from the epitaxial film, the copper could pull up the film, separating it from the silicon wafer chip it had been mounted to with wax. Depending on the degree of curling and detachment of the film, this may or may not render the sample unsuitable for further processing. In all such cases, however, photolithography is complicated by the non-planarity of the film.

Once the substrate was successfully separated from the epitaxial film, the film was rinsed with clean deionized water a last time and thoroughly blown dry with clean dry nitrogen. It was found that if the sample was not dried thoroughly enough, a light haze formed on the epitaxial film. This haze is believed to be, based on x-ray photoelectron analysis of the surface and discussions with experts in epitaxial lift-off, arsenic oxides. A cleaning procedure consisting of a 30 s dip in a 5% H_2O_2 solution followed by a 30 s dip in a 5% NH_4OH, was successfully employed to remove this surface oxide. However it was also found that the formation of the oxide could be avoided if the sample was thoroughly dried on all surfaces and stored in a nitrogen dry-box.

Epitaxial Lift-Off from Indium Phosphide Substrates

InP wafers acted as the growth substrates for the three lowest bandgap devices, but their suitability for epitaxial lift-off was not as well evidenced as GaAs devices. Early demonstrations of epitaxial lift-off from InP utilized AlAs release layers, grown via molecular beam epitaxy (MBE). The large lattice mismatch between InP and AlAs means that even very thin layers of AlAs are susceptible to relaxation via the formation of crystallographic defects which act as centers of non-radiative recombination and degrade device performance. In this work, we pursued two parallel strategies for achieving epitaxial lift-off from InP wafers. First, we explored ternary lift-off layers of InAlAs whereby the alloying if In would reduce the lattice mismatch with the substrate, and allow pseudomorphic growth of sufficiently thin sacrificial layers. Second, we explored a lattice matched ternary alloy of AlAsSb which ultimately proved the more attractive solution.

InAlAs Epitaxial Release Layers

The Matthews-Blakeslee model [45] for critical thickness of a mismatched epitaxial layer is an equilibrium force-balance model that calculates the thickness of a mismatched epitaxial layer at which there is a driving force for the generation of misfit dislocations within the epitaxial layer. As an equilibrium model, it is possible to grow structures thicker than the critical thickness that remain pseudomorphic do to kinetic limitations, but it provides an idea of the difficulty in attempting to do so. The composition of InAlAs lattice matched to InP, lattice constant of 5.869 A, is $In_{0.52}Al_{0.48}As$. Binary AlAs, with a lattice constant of 5.660 has a 3.56% lattice mismatch. In order for there to exist a useful ternary InAlAs ELO layer, it must incorporate as much indium as possible so as to minimize the lattice mismatch and allow pseudomorphic growth, while retaining the chemical etch properties of AlAs as regards stability in hydrofluoric acid.

To investigate this system, Spectrolab provided growth templates of InP layers on InP substrates with InAlAs release layers. The template structure is denoted in table 4.1 below. The two compositions of InAlAs release layers grown were $In_{0.20}Al_{0.80}As$ and $In_{0.06}Al_{0.94}As$. In the AlGaAs system, the transition from stability in hydrofluoric acid to rapid etching spans several orders of magnitude over a small composition range [46], and it was hoped that Al-rich InAlAs alloys would behave similarly.

Samples from the low indium content growth exhibited good epitaxial liftoff in 10% hydrofluoric acid solution. Samples up to 1 cm wide etched for 12 hours reliably lifted-off from their substrate without issue. Samples from the higher indium content growth, however, exhibited significantly retarded lateral etching. In order to enhance the etch rate, process variables were modified on various samples. Table 4.2 describes a set of experiments varying the bath temperature and the etch concentration.

A final effort was made to promote the lateral etching by applying tension to the film during the etch such that as the sacrificial layer etched away, the crack would

Growth Order	Description	Composition	Thickness (nm)
5	Test Layer	InP	1500
4	Sacrificial Etch Layer	$In_xAl_{1-x}As$	10
3	Buffer Layer	InP	1500
2	Etch Stop Layer	$In_{0.53}Ga_{0.47}As$	100
1	Buffer Layer	InP	200
-	Substrate	InP	-

Table 4.1: Epitaxial layer structure for a template to test epitaxial liftoff from InP with InAlAs layers.

Etchant	Bath Temperature (C)	Result
2% Buffered HF	20	No significant Etching
10% HF	20	No significant Etching
25% HF	20	No significant Etching
48% HF	20	No significant Etching
2% Buffered HF	65	No significant Etching
10% HF	65	<1 mm lateral etching
25% HF	65	<1 mm lateral etching
48% HF	65	<1 mm lateral etching

Table 4.2: Summary of experiments to sacrificially etch In-rich InAlAs lift-off layers.

be widened by the applied force, allowing easier diffusion of reactants and products, ensuring the etch was reaction rate limited. This was accomplished by mounting the epitaxial film to a flexible polyimide sheet with wax, and inserting a threaded PTFE rod through two holes in the sheet and securing it with PTFE nuts. The applied stress was controlled by the radius of curvature of the sheet, which was adjusted by the distance between the insertion points of the rod in the sheet. This apparatus is pictured in figure 4.5. The strained films were etched at 50 °C in etchant concentrations of 10% or 25% hydrofluoric acid, but unfortunately the only films that separated from their substrate showed significant attack of the InP overlayer.

These experiments showed that a useful InAlAs ELO layer composition need contain less than 20% indium on the group III sub-lattice. While the 6% indium samples lifted off well, the InP films they released showed significant texture that would not be compatible with high voltage devices. Figure 4.6 depicts optical micrographs of the epitaxial surfaces after growth of both the low-indium and higher-indium content growths.

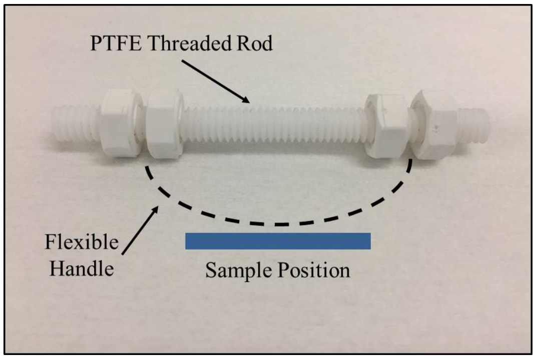

Figure 4.5: Apparatus to apply tension via a flexible handle (indicated by a dashed line) constrained at two ends by a PTFE threaded rod. Adjusting the position of the nuts adjusts the induced curvature in the flexible handle, and thus the tension applied to the film being lifted off.

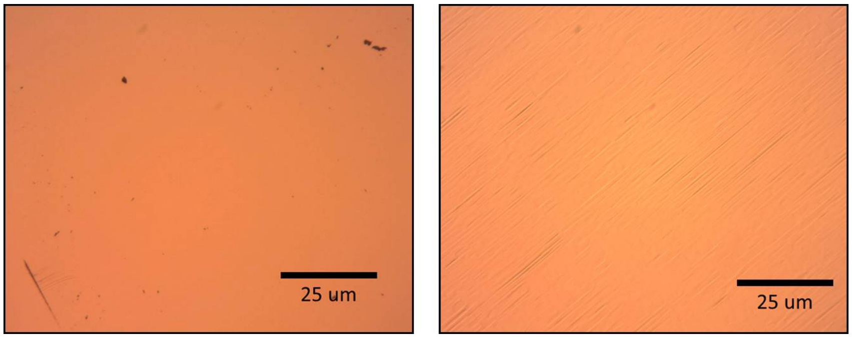

Figure 4.6: Optical micrographs of the surface of epitaxial InP grown upon an In-rich InAlAs layer (left) and an In-poor InAlAs ELO layer (right). The sample on the right exhibits surface texture incompatible with high material quality.

These experiments set a bound on the desired composition of an InAlAs ELO layer, and whether or not there exists an intermediate composition that has excellent etch selectivity with low enough lattice mismatch to grow a 5 nm thick unrelaxed pseudomorphic layer remains to be seen. Our efforts shifted towards AlAsSb ELO layers at this point after they demonstrated promise.

AlAsSb Epitaxial Release Layers

As discussed already, AlAs has a lattice constant smaller than InP by more than 3.5%, making it unsuitable as a release layer from InP. AlSb, meanwhile, has a lattice constant of 6.136 A, larger than InP by more than 4.5%. This means that there is a ternary alloy with composition $AlAs_{0.56}Sb_{0.44}$that is lattice matched to

InP. Literature reports of the etching of AlSb with hydrofluoric acid suggest that the lattice matched ternary composition will also etch in hydrofluoric acid, and if it etches quickly enough it will serve as an ideal ELO layer.

Epitaxial growths were performed by Spectrolab featuring 0.74 eV single junction InGaAs photovoltaic cells on InP wafer substrates with lattice matched AlAsSb ELO layers. These samples reliably released from their substrates in 10% hydrofluoric acid. Of note is that unlike the epitaxial lift-off from GaAs substrates, the epitaxial lift-off from InP substrates using AlAsSb ELO layers did not work with the hydrofluoric acid and ethanol etchant. The mixture of equal parts by volume concentrated (48%) hydrofluoric acid and ethanol did not release the InGaAs devices despite etch times of up to several days. Thus 10% hydrofluoric acid at room temperature was utilized for all subsequent InP-based epitaxial lift-off in this work. The success of the AlAsSb ELO layer obviated the need to tune the composition of InAlAs for possible use as an ELO layer.

4.3.5 Top Contact Formation

Following successful epitaxial lift-off, the epitaxial layers which were grown inverted are not upright, and the buried n-type contact layer which was adjacent to the sacrificial etch layer is exposed. The next step in the device fabrication process is to form an electrical contact to this layer via thin film metal deposition. Unlike the rear electrical contact, however, this contact cannot cover the entirety of the contact layer or it would block any light from entering the cell. Depositing thin metal lines in a grid can minimize this shadow loss. Generally grid designs involve smaller, densely packed lines referred to as fingers which feed into wider metallic traces known as busbars. External contacts can then be made to the busbars.

If the metal fingers are too sparse or too thin they will exhibit unacceptably high series resistance that will degrade device efficiency. The path of collected carriers in the device involves lateral transport through the emitter and window layer until they reach a finger, transport from the semiconductor into the metal, and then transport along the finger. Thus the series resistance for a given grid layout is the sum of the sheet resistance of the emitter and window, the contact resistance into the metal, and the resistance within the metal finger. A fuller description of the design of the top contacts is offered in chapter 4.

Photolithography was used to define the top contacts by masking the film everywhere except where metal is desired. A Karl Suss MJB3 mask aligner, along with two types of photomasks were utilized in this work. Ink printed transparency masks purchased from CAD Art Services of Bandon OR were used because they were inexpensive and can be acquired with rapid turn around, useful for testing different mask designs rapidly. These transparency masks have a minimum feature size of 10 μm, which was not limiting. However, there are two drawbacks to ink transparency masks. First, when attached to a quartz plate in the mask aligner window, they have a tendency to sag very slightly, and the air gap between the quartz plate and the mask can diffract or scatter light, resulting in less sharp lithographic patterning. Secondly, the plastic on which the masks are printed has small scattering features, possibly bubbles, that result in more light scattering under printed mask area, and also less light directly underneath the bubbles. This scattering results in a narrowed window of process parameters for good photolithography. When using a negative resist, the scattering of light away from these bubbles can result in an under exposure beneath them, and thus leaves areas where the resist comes off during development where it should have stayed. This results in unintended metal deposition on areas of the front surface, and undesirable shadowing losses. Longer exposures avoid this issue, but will result in additional dosage underneath mask features, limiting the minimum attainable feature size.

Photolithographic processing for the top contact was undertaken in a cleanroom facility. A lift-off resist, LOR-10a was used to facilitate metal lift-off. A spin coater was used to apply LOR-10a, spun at 1500 rpm for 30 seconds resulting in approximately 2 μm thick layer. Samples were then baked at 165 °C for 10 minutes on a hotplate before removal from the hotplate to return to room temperature. Negative photoresist, specifically nLOF 2000 from AZ Electronic Materials, was then spun on top of the lift-off resist at 3000 rpm for one minute. Samples were pre-baked on a hotplate at 110 °C for one minute to remove some solvent from the resist.

Samples were then exposed for either 30 seconds under a transparency mask or 10 seconds under a chrome mask on quartz. These correspond to UV dosages of approximately 180 and 60 mJ/cm^2 respectively, although it should be noted that the higher dosage under the transparency mask is due to strong UV absorption in the mask, rather than significantly enhanced dosage to the resist. After exposure samples were soft baked for one minute on a hotplate at 110 °C before being developed for one minute in 300 MIF developer from AZ Electronic Materials, a tetramthylammonium hydroxide based developer. Visual inspection with an optical microscope verified the development was successful, and if for some reason the photolithography was incomplete, additional development time was added in one minute increments. If the pattern was still unsatisfactory, the resist was stripped by heating the sample to 50 °C on a hotplate in n-methylpyrrolidone for several minutes. Following the solvent stripping, the sample was rinsed with acetone and then isopropyl alcohol before repeating the photolithographic process.

4.3.6 Top Contact Metal Deposition

The deposition of the top contact metalization was performed in the same electron beam evaporation system that the rear mirror was done with. Two separate top contact metalization schemes were used, one for the InP based devices and one for the GaAs based devices.

GaAs Top Contact Metalization

Unlike the rear contact, the n-type GaAs contact layer to which the top contact must form Ohmic contact was not heavily doped enough to create a tunneling contact with just any metal deposited. Deposition of a thin nickel adhesion layer followed by gold or silver results in a rectifying Schottky type contact which is presents an undesirable barrier to current flow. Therefore, a more advanced Ohmic contact scheme was required to form a low resistance Ohmic contact to the devices fabricated from the four GaAs based growths.

A common scheme [47] for forming Ohmic contacts to n-type GaAs involves the deposition of Au and Ge layers, which form a eutectic composition at 88/12 wt% Au/Ge. The eutectic temperature of this alloy is 360°C, but processing typically involves rapid thermal annealing at 450-500 °C to form the eutectic alloy and allow Ge atoms to diffuse into the III-V to form local regions of very high doping. There has been significant work developing this contact scheme for n-GaAs, and very low contact resistances have been achieved. However, due to the thermal behavior of the thin film devices backed by thick copper films in this work, a lower temperature contact scheme was required.

An attractive solution is found in the Ge/Pd scheme first reported by Marshall et al [48]. This system of Ohmic contacts is a solid phase regrowth scheme, in which the Pd initially reacts with the GaAs and forms intermetallic PdxGaAs compounds at low temperatures. As the material is annealed, the deposited Ge reacts with the Pd and consumes it from the intermetallic, resulting in a PdGe which facilitates diffusion of Ge atoms to the epitaxial surface. This results in a regrown epitaxial layer of Ge at the interface with GaAs. Additionally, Ge which diffuses into the GaAs acts as an n-type dopant and further reduces the width of the energy barrier at the interface, reducing the contact resistance further. Finally, a thick gold over-layer serves to reduce the line resistance of the contacts, as well as alloying with the excess germanium to reduce the resistance through it. Literature reports have shown that this solid phase regrowth scheme utilizing Au/Ge/Pd is kinetically limited and will proceed given sufficient time at temperatures as low as 120 °C [49] making at an ideal Ohmic contact scheme for the epitaxial films in this work.

The top contacts for GaAs based devices were fabricated by sequential electron-beam evaporation of a Au/Ge/Pd structure [50]. The thicknesses of each layer were the same for devices at all four bandgaps grown on GaAs, and they were 10 nm of Pd, 50 nm of Ge, and 500 nm of Au. The thicknesses of Ge/Pd were taken from Wang et al. [49], and the gold layer was made as thick as practical for the photolithographic processes used.

InP Top Contact Metalization

Epitaxial growths of the three lowest bandgap devices, grown lattice matched on InP substrates, included top contact layers with sufficiently high doping so as to form Ohmic contacts with low contact resistance by depositing thin metallic layers without annealing. For growths at all three bandgaps, the same top contact scheme was used with success. This scheme involved a thin nickel adhesion layer, between 3 and 5 nm thick, followed by 500 nm of gold. This thickness of gold was chosen as the thickest practical layer which could be reliably lifted off from the 4 μm thick resist. Electroplating of gold as top contacts is a promising route for fabricating higher aspect ratio features, the lower resistance of which would reduce the shadowing requirements. However, in this work all top contacts were evaporated onto patterned resist.

Metal Lift-Off

After metal deposition, samples were immersed in a bath of Remover PG, a proprietary mixture of the solvent n-methylpyrrolidone and surfactants which facilitate the removal of photoresist under metal. Dissolving the photoresist allowed the metal deposited above it to lift-off, leaving only those areas where no photoresist remained as defined by the photolithography. Samples were soaked in Remover

PG for approximately 30 minutes, and sonication was avoided because it had a tendency to break off thin metal gridlines, which would result in unacceptably high series resistance. Heating was also avoided because the solubility of black wax in n-methylpyrrolidone increases markedly, and this can cause the film to de-adhere from the silicon carrier or peel upwards, damaging the epitaxial devices. In cases where the lift-off was not proceeding well, a fabric tipped plastic applicator was used to gently wipe the metal while immersed in Remover PG.

After all the metal had lifted-off, samples were soaked for several minutes in clean remover PG so as to remove any remaining LOR-10a residue. They were then rinsed with acetone and isopropyl alcohol before being blown dry with clean dry nitrogen.

4.3.7 Annealing of Top Contacts

The top contacts on InP based devices required no additional process steps, but the Pd/Ge/Au metalization scheme required an annealing step for the solid phase regrowth to occur and form an Ohmic contact. The mismatch in the coefficient of thermal expansion between the copper handle and the III-V device layers presets challenges for elevated temperature processing. The copper handle has a thermal expansion coefficient several times larger than the semiconductor layers, and as such there is a stress during heating that which imparts a tendency to curl upward. This curling can be prevented by fixing the film in place with polyimide tape, but in doing so temperature must be kept low enough that the resulting strain does not damage the device layers. Furthermore, as the copper is approximately 20-40 times thicker than the epitaxial layers its expansion dominates the mechanics of the expansion of the combined copper-semiconductor film, causing a tensile strain in the epitaxial layers. If this tensile strain is too large cracks will readily develop in the brittle semiconductor materials, which act as centers for non-radiative recombination. Simple calculations of the tensile strain in the GaAs film as a result of the coefficients of thermal expansion indicate that at 200 C, the GaAs is under only 0.2% tensile strain, which is well within the elastic limit at that temperature [51]. However, physical defects in the sample can concentrate stresses, and empirically, experiments showed that when the lifted-off epitaxial films on copper film handles are heated in excess of 250 °C, expansion and warping of the films induces cracks in the epitaxial layers that would degrade device quality significantly.

After the deposition of the contact metals, samples were annealed in a quartz tube furnace while dry nitrogen was flowed through the tube. A number of samples were annealed at temperature between 150 and 250 °C for periods of time between 30 minutes and 24 hours. Circular transmission line measurement (CTLM) [52] [53] test features were used to assess the nature and resistance of the contact formed. Below 200 °C, contacts were not found to be Ohmic with annealing times up to 24 hours. At 200 °C, contacts were found to be Ohmic after 16 hours of annealing, with reduced contact resistance after 24 hours. At 250 °C, contacts were found to be Ohmic after 3 hours. In order to minimize the thermal stresses on the films, an anneal at 200 °C for 24 hours was adopted as the standard process for annealing the metal contacts to n-type GaAs. Figure 4.7 shows the CTLM measurement of a sample annealed at 200 °C for 24 hours. In a CTLM measurement a series of circular metal pads are separated from surrounding metal by a ring of varying thickness with no metal. Probes are used to measure the linear resistance between the center pad and the surrounding metal, and the the un-metalized ring forces the current path through the contact, into the semiconductor, and then back into the metal. Measuring a series of pads with different ring widths provides, after a geometric correction factor for current spreading, a linear function of resistance with ring width. The slope of this trend reflects the sheet resistance of the semiconductor while the intercept indicates the contact resistance. Table 4.3 summarizes the contact resistances measured for a single sample from each device bandgap.

Device Bandgap (eV)	Metalization	ρ_C ($\Omega \cdot cm^2$)
0.74	Au/Ni	$3.4 * 10^{-5}$
0.93	Au/Ni	$5.0 * 10^{-6}$
1.15	Au/Ni	$8.9 * 10^{-6}$
1.42	Au/Ge/Pd	$2.1 * 10^{-6}$
1.54	Au/Ge/Pd	$4.7 * 10^{-5}$
1.78	Au/Ge/Pd	$5.3 * 10^{-5}$
2.10	Au/Ge/Pd	$1.4 * 10^{-5}$

Table 4.3: Contact resistances measured by CTLM features for the top contact metalization at each device bandgap.

4.3.8 Contact Layer Removal Etch

After the top contact has been formed, the next process step is to remove the semiconductor contact layer across the device except underneath the metal contacts. This is only necessary in the cells grown on GaAs, as they contain absorber layer bandgaps equal to or greater than the bandgap of the GaAs contact layer. The InP cells, however, have InP contact layers with a wider bandgap than the designed

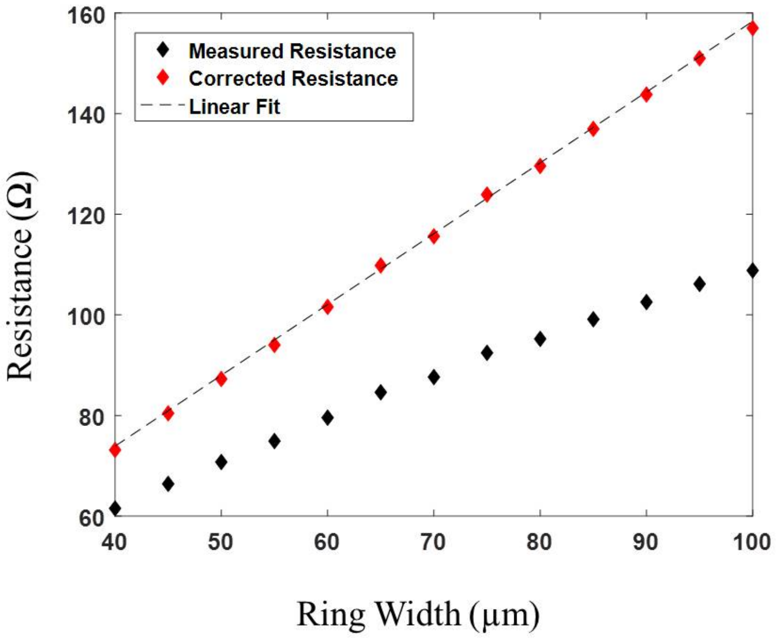

Figure 4.7: Example circular transmission line measurement to extract contact resistance.

spectral band. Therefore, removing the InP contact layer is not necessary, as it does not strongly absorb the incident light. An additional complication is that the contact and window layer on the InP based devices is InP, and thus there is not a suitable selective etch to remove the contact layer but not the window.

There is a highly selective etch system for removing the GaAs contact layer from the various ternary window layers utilized in the four highest bandgap devices though, including AlGaAs, InGaP, and AlInP. A mixture of ammonium hydroxide, hydrogen peroxide, and deionized water in the ratio 1:20:20 (NH_4OH:H_2O_2:H_2O). This basic etch is well known in literature REFERENCE: NREL IMM and Clausen and besides selectivity over the window layer, has the additional benefit of forming soluble complexes with metal impurities making it suitable for exposure to the metal contact mask. Thus, the contact etch is performed without an additional photolithographic step, rather the deposited top contact metal is used as a mask to retain the doped contact layer directly beneath it.

In preparation of the contact etch, however, the edges of the samples were coated in thick photoresist to mask the thick copper handle from exposure to the etch solution. This was done by manual application of Shipley 1813 resist using a fabric tipped plastic applicator. A bead of resist was first drawn along the edge of the film, liberally applied particularly to areas where copper was visible. A thin layer was then applied to the top of the film along the edge, extending approximately one half millimeter from the edge of the film towards the center. The sample was then baked on a hotplate for 10 minutes at 90 °C to evaporate the solvent from the resist.

Following masking of the film edges, the etch was performed by immersion in the etchant for 30 seconds. Agitation was supplied by gently pipetting the etchant across the surface to dislodge any bubbles that formed. The high concentration of hydrogen peroxide generated a number of bubbles that would inhibit diffusion of etchant to the surface, resulting in uneven etching. Dislodging the bubbles with gentle agitation ensured the etch progressed fully to the selective window stop layer, leaving no residual optically absorbing GaAs contact layer.

Bubble formation fell drastically after approximately 20 seconds, visually indicating the complete removal of the GaAs contact layer. After 30 seconds the sample was removed from the etch bath and rinsed under deionized water for at least 30 seconds, and then blown dry with clean dry nitrogen. The edge masking photoresist was removed by rinsing in acetone and then isopropyl alcohol, followed by drying with clean dry nitrogen.

4.3.9 Mesa Isolation

The final process in device fabrication before electrical characterization is practical is to electrically isolate devices from each other and surrounding epitaxial material. This is done by a wet chemical mesa etch that removes semiconductor material on the film everywhere except where the devices are defined.

The active area of each device was defined by a second photolithographic step, aligned to the array of devices and test features. The mesa pattern was 200 μm wider in each dimension than the contact grid, thereby providing 100 μm of tolerance on each edge for any rotational or translational alignment error. Additionally, the mesa etch can cause significant undercutting around the mask due to the multiple alternating etch steps. Adhesion of the mask to the film and the chemical resistance of the resist is most challenged during the multiple mesa etch steps, and any amount of peeling or delamination of the mask will occur first at the edges.

Following development of the mesa isolation resist mask, the edges of the film were masked to protect the copper film from exposure to the mesa etch solutions. This was done via manual application of photoresist as described previously for the contact etch step for GaAs devices. Following baking on a hot plate, polyimide tape was overlaid along each edge of the film, extending up to one millimeter from the edge of the film. This additional layer of tape is not strictly necessary, but it did make the mesa etch more reliable against pinholes in the edge masking photoresist. When the copper film was exposed to mesa etching, it generally fouled the etching, leading to highly non-uniform etching and unsuitable devices.

Mesa isolation via wet chemical etching of the seven different device structures required several different processes because of the different compositions involved. They all involved alternating between two etches which each tended to attack either arsenides or phosphides strongly over the other. The arsenide selective etch was composed of phosphoric acid, hydrogen peroxide, and deionized water in the ratio 3:4:1 (H_3PO_4:H_2O_2:H_2O). This is a commonly used etchant in GaAs device fabrication that operates by injecting holes into the semiconductor by decomposing hydrogen peroxide. This oxidizes the surface and the resulting Ga and As oxide species are soluble at the pH of the etchant. Concentrated hydrochloric acid was used for phosphide layers.

After each etch step, the samples were rinsed in deionized water for 20-30 seconds and blown dry with nitrogen. Immediately prior to each phosphide layer etch step, the samples were baked on a hotplate at 110 °C for one minute to desorb any water, which can inhibit the etching by concentrated hydrochloric acid. The series of mesa isolation etches for each bandgap are described in the table below.

Additionally, some portion of samples fabricated from growths at 1.15 and 1.78 eV, the back mirror was not fully exposed after the final etch step. Repeated application of the alternating selective etches did not complete the mesa etch, owing to some unknown surface modification. Refreshing the etchants also had not impact. For these samples an additional final etch step was performed with aqua regia, a solution comprised of three parts to one of hydrochloric and nitric acid. Aqua regia is non-selective towards all the III-V materials in the device stacks, and etches very rapidly. After mixing hydrochloric acid and nitric acid, they react and one of the products is gaseous chlorine. This chlorine gas is the main etching mechanism of the solution [54], and consequently the etch rate through the various device layers is highly dependent on the age of the aqua regia solution and the concentration of chlorine gas. In this work, the aqua regia solution was allowed to age for at least 10 minutes and no longer than one hour for use as a mesa etchant. Since aqua regia strongly attacks the materials that comprise the back mirror and handle, namely gold

Bandgap	First Etch	Second Etch	Third Etch	Fourth Etch	Fifth Etch	Sixth Etch
0.74 eV	HCl (0:30)	H_3PO_4 (2:00)	HCl (0:40)	H_3PO_4 (0:10)		
0.93 eV	HCl (0:30)	H_3PO_4 (2:00)	HCl (0:40)	H_3PO_4 (0:10)	HCl (0:30)	H_3PO_4 (0:10)
1.15 eV	HCl (0:30)	H_3PO_4 (2:00)	HCl (0:40)	H_3PO_4 (0:10)	HCl (0:30)	H_3PO_4 (0:10)
1.42 eV	H_3PO_4 (1:30)	HCl (0:30)	H_3PO_4 (0:10)			
1.54 eV	HCl (0:30)	H_3PO_4 (2:00)	HCl (0:30)	H_3PO_4 (0:10)		
1.78 eV	HCl (2:00)	H_3PO_4 (0:30)	HCl (0:30)	H_3PO_4 (0:10)		
2.10 eV	HCl (2:00)	H_3PO_4 (0:30)	HCl (0:30)	H_3PO_4 (0:10)		

Table 4.4: Summary of sequences for mesa isolation etching of all seven bandgap devices. The etching consisted of alternating between concentrated hydrochloric acid (denoted HCl in the table) and a mixture of phosphoric acid, hydrogen peroxide, and water in the ratio 3:4:1 (denoted H_3PO_4 in the table). Times for each etch step are indicated in (M:SS).

and copper, the samples were quickly rinsed in deionized water as soon as the back mirror was completely exposed. This was generally before the entire thickness of gold mirror was removed, but for some samples pitting was observed in the copper film.

After the mesa etch was successfully concluded and the back mirror exposed between adjacent devices, the polyimide tape was removed from the sample edges and the Shipley 1813 photoresist was removed by rinsing in acetone and then isopropyl alcohol. The samples were then blown dry and stored in a nitrogen dry box.

4.4 Prototype Integration

Following mesa etching, multiple devices which were electrically isolated and ready for optoelectronic characterization existed on each film processed. The precise number of devices depended on the mask design used and the precise film area. An example of different mask designs utilized for this work are depicted in figure 4.8. They vary in the size and number of cells the contain, the spacing between cells, and the presence or absence of electrical test features. Additionally, some samples were fabricated on wafer pieces slightly larger or smaller than 1 cm x 1 cm, and some

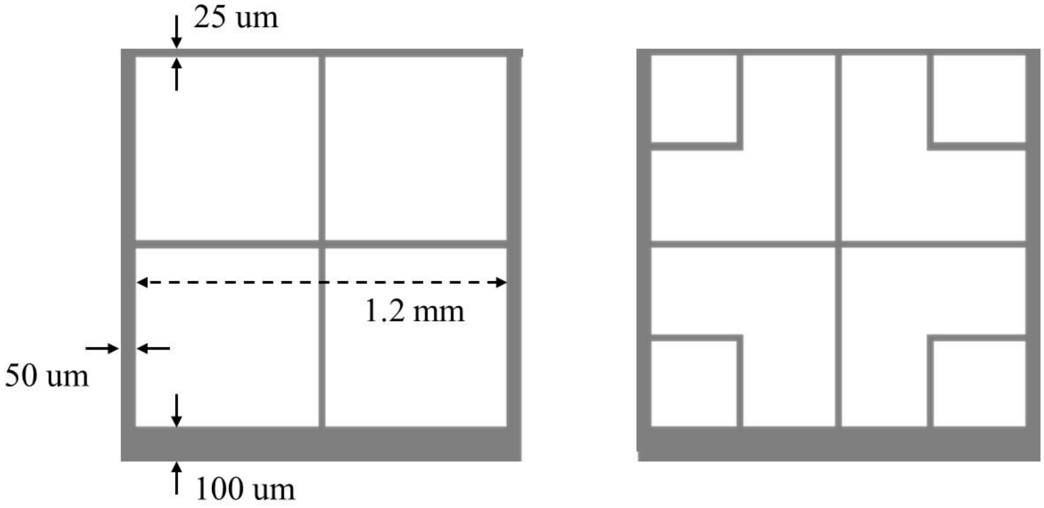

Figure 4.8: Inverted square top contact metalization patterns employed for cells designed for 100x light pipe concentrators with 1 mm output faces. Left: Design for GaAs based cells featuring one grid finger in each direction. Right: design for InP based cells featuring three grid fingers in each direction.

films sustained damage during processing that destroyed one or more cells.

In order to select the highest performing cells from each film that would be processed further, four point electrical testing was performed on all devices on a sample. Two measurements were performed on each device, and they were an illuminated linear current-voltage sweep and a decadal current sweep in the dark. Samples were illuminated by a solar simulator built from a halogen lamp with an AM1.5 spectral filter. Lamp intensity was calibrated with a calibrated silicon reference cell. The mismatch between the external quantum efficiency of the reference cell and the devices of seven different bandgaps under test makes this an imperfect absolute measure of efficiency. However, this measurement is a good relative qualification to select the highest performing devices from any particular sample.

The widest edge of the top contact busbars were no more than 200 μm wide, and thus a probe station was used to attach a source and a sense lead to the negative side, while the remaining two probes were placed in contact with the rear mirror adjacent to the device. All of the devices on a single sample shared a common back contact at the rear mirror and copper handle. While the sample was illuminated, an IV trace was taken with a Keithley 238 source-measure unit was used to source voltage in linear increments and measure the current passing through the device. Next, with

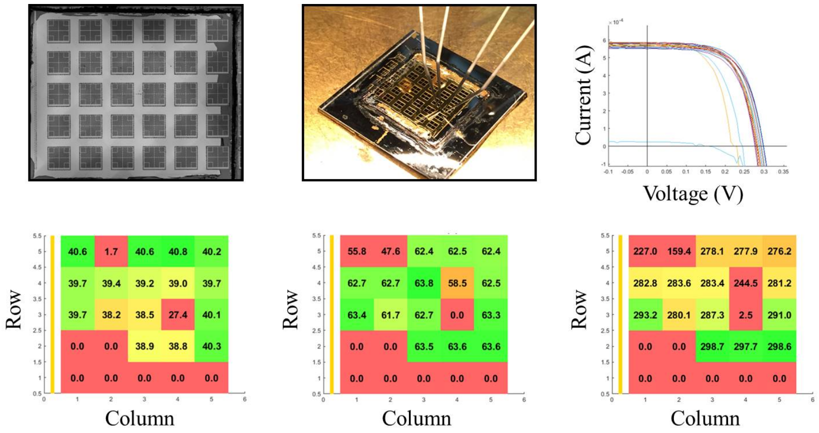

Figure 4.9: Qualification sequence to select champion devices from each processed film for further integration into prototypes.Top left: Optical image of a 5x5 array of devices following mesa etching. Top middle: Four point IV testing of each device in the array. Top right: Resulting IV traces. Bottom left: Map of short circuit currents. Bottom middle: Map of fill factors. Bottom right: Map of open circuit voltages.

the illumination turned off, the source-measure unit was used to source current from the nano-amp to the milliamp regime and measure the resulting voltage.

The light IV measurements allowed the devices to be sorted according to their efficiency, while the dark IV measurements offered additional information about the diode behavior of the devices throughout integration steps. Following the measurement of all devices on a film, up to four of the best performing devices were selected for further integration steps. In sample layouts where the isolation distance between samples was reduced, cells adjacent to champions would be sacrificed during singulation so as to not damage the champion. Therefore, in these layouts the highest performing cells were selected with consideration taken for their adjacent cells. For instance, if three high performing cells lay in a line, the two on the ends would be selected rather than the one in the middle, in the interest of generating a larger number of high performing cells. Figure 4.9 depicts a typical map of the photovoltaic device parameters extracted from a set of cells.

Mapping the measured device parameters made clear the optimal series of cuts to separate the champion cells from the film via singulation.

4.4.1 Singulation

In order to separate the champion cells from each film for further processing and possible eventual integration with the spectrum splitting optics, they needed to be physically released from their adjacent cells on the copper film. After identifying the set of up to four champions on a film, the films containing arrays of cells were placed on a glass slide and one edge was gently taped down with polyimide tape. This tape prevented the film from slipping or rotating during a cut and destroying cells. A stereoscope with 20x objective was used to better observe the manual process and allowed repeatable positioning and cutting within 100 um. A series of cuts were then made manually with a #10 scalpel blade. As much as possible efforts were made o avoid inducing any curvature in the films, however on occasion the copper film would adhere to the blade, and pull upward upon release of pressure. If the curvature induces tensile stresses in the semiconductor layers the formation of micro-cracks may result and degrade the device quality by acting as non-radiative recombination centers. For this reason cuts were made some distance from the edges of the photovoltaic devices. The precise distance varied depending on the photomask. Masks utilized for initial prototypes feature mesa isolation widths of 800-1000 μm, and singulation cuts were made along these channels. This had the benefit of releasing every device made, but it left only 400-500 μm buffer on either side of the cut. Accounting for the approximately 100 μm of tolerance via manual cutting, and cuts came as close as 300 μm to the photovoltaic devices. Photomasks for the final prototype used 800 μm of mesa isolation, but in order to minimize any possibility of damage from singulation, cuts were made not along those mesa isolation channels but rather through the middle of cells adjacent to champion cells. This destroyed those cells, but offered a total of 1.5 mm between the edge of the champion devices and the singulation cuts.

4.4.2 Mounting and Wire bonding

Singulated cells were mounted to chip carriers to physically protect them during subsequent integration steps, including attachment to optics and circuit board, and mechanically isolate the fragile devices during electrical characterization. The cells were mounted to CSO008P4 carriers from Spectrum Semiconductor with conductive epoxy as pictured in figure 4.10. The chip carriers feature a 3 mm wide square center pad and two sets of four electrically independent gold-plated feet on opposite sides.

The epoxy used to set the device film on the carrier was EPO-TEK H20E from Epoxy Technologies. It is a two part silver epoxy with a high thermal conductivity.

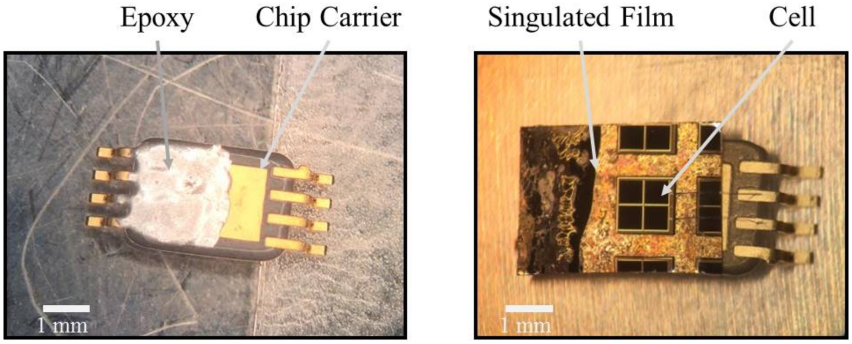

Figure 4.10: Left: Chip carrier with epoxy applied in preparation of mounting a singulated cell. Right: Mounted cell on chip carrier.

It was mixed and painted onto the chip carriers with an applicator so as to evenly coat the carrier with several hundred μm of epoxy. It was found to be important that the epoxy layer was as flat as possible, as features could give rise to voids below the film which complicate significantly the wire bonding process. If there were areas of the film near or under the busbars that were not supported by epoxy, they would not be mechanically robust during wire bonding and could present issues such as puncturing the film or lifting it up, inducing cracks and curvature. The epoxy was spread across the center pad and along the tops of one set of four feet so as to electrically connect that set of feet to the center pad and rear of the device film. The film was positioned such that the thickest edge of the busbar was nearest the second set of feet, which remained unconnected and electrically isolated from the center pad. The epoxy needed to be spread far enough towards this second set of feet to fully cover the device, particularly under the busbar which was to be wire bonded, but not so far that there was any danger of shorting when the epoxy spreads as the film is set into it. Plastic tweezers were used to gently push the film into the epoxy in order to leave the film as parallel to the chip carrier as possible, to ensure the device active area will be parallel with and as close as possible to the output face of the secondary concentrator during attachment. The carriers with the mounted cells were pre-baked on a hotplate at 80 °C for 30 minutes in order to tack them down and prevent jostling during transport to an oven where the epoxy was cured at 120 °C for 30 minutes.

Following the epoxy cure, the top contacts of the mounted cells were electrically connected to the remaining set of feet on the chip carrier via gold wire bonds. Wire bonds were formed using a Westbond 7476D wedge-wedge wire bonder housed in the Kavli Nanoscience Institute.

4.4.3 Anti-Reflection Coating

Single layer anti-reflection coatings were deposited on all mounted cells following wire bonding. Undergraduate researcher Kevin Chen deposited layers of TiO_2 via electron beam evaporation on glass slides and measured the index of refraction and thickness using profilometry and ellipsometry. With the optical properties known, the open source software OpenFilters [55], utilizing the transfer matrix method, was used to determine the optimal anti-reflection coating thickness for each spectral band.

Table 4.5 lists the target thickness of TiO_2 for the anti-reflection coating of each spectral band.

Cell Bandgap (eV)	TiO_2 Thickness (nm)
0.74	176
0.93	142
1.15	118
1.42	99
1.54	86
1.78	71
2.10	50

Table 4.5: Thicknesses of single-layer TiO_2 antireflection coatings for the seven spectral bands.

4.4.4 Attachment to Optics

The penultimate assembly step of the integrated optoelectronic prototypes was the attachment of the cells to the small output faces of the light pipe secondary optical concentrators. The cells featured an active area that was 200 μm larger in each dimension than the output face of the lighpipes, allowing for 100 μm of tolerance along each edge against rotational and translational misalignment. In order to attach the optics within this tolerance, Dr. Cris Flowers constructed a mounting jig, shown in figure 4.11. The jig was constructed on an eight inch optical breadboard which served as a base. The chip carriers with their attached cells were positioned in the center of a rotational stage, allowing azimuthal control over the cell's alignment. A set of three connected manual linear stages were also mounted to the breadboard, and supported a 3D-printed jig that seated the light pipe, allowing 3-axis translational

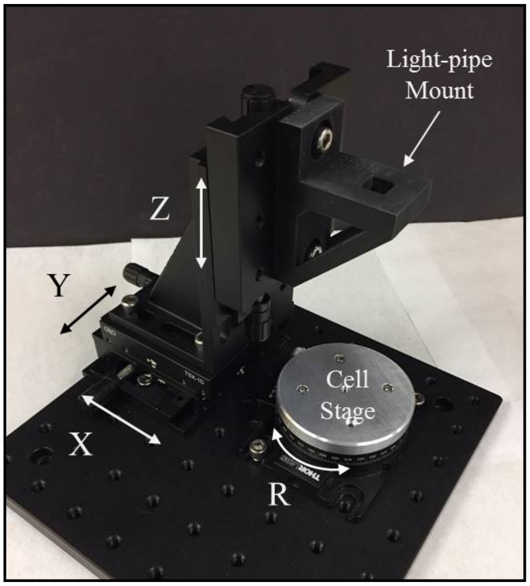

Figure 4.11: Alignment jig for attaching 100 mm long 100x light pipes to photovoltaic cells mounted on chip carriers. Features three axes of translation for the optic and a rotaional axis for the cell.

control over the positioning of the optic. The 3D-printed jig held featured a square profile hole with tapered interior sidewalls slightly narrower than the 1 cm input face of the light pipes. This held the light pipes in place vertically above the chip carrier. 4 microliters of PDMS was dispensed on the top of the photovoltaic device active area, and the stages were used to bring the optic and cell into position. As the light pipe was brought down into contact with the PDMS, it was obvious when the PDMS had fully wet the output face.

Although the light pipes are non-imaging optics, visually observing the image through the input face of the light pipe provided the best alignment indicators. The observed image included a central undistorted image of the output face, as well as a series of reflections of that image. The electrical grid lines on the cell active area provided useful alignment features. The rotational stage was driven until the grid lines formed only orthogonal shapes, indicating that the cell was rotationally aligned with the light pipe. Then lateral adjustments were made with the linear stage such that the repeating pattern observed through the length of the light pipe was consistent with the multiple reflections of a centered inverted square contact grid. Finally, the light pipe was further lowered while observing from the side. Care was taken to minimize the separation between the light pipe and the cell, and this was

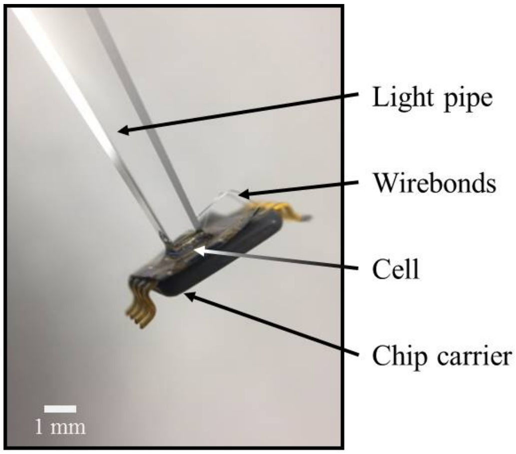

Figure 4.12: Cell mounted on chip carrier and attached to a 100x light pipe.

repeatably done to a distance of less than 100 μm.

The PDMS was cured in-situ by using a heat gun while the cell carrier and light pipe remained in place in the jig. Initial efforts involved placing the entire breadboard jig into an oven and curing at 80 °C, but as is described in chapter 4, the thermal expansion of the jig created an intolerable gap between the cell and the light pipe. Local heating via a heat gun completely solved this problem by keeping the jig at close to room temperature, and furthermore allowed for slight adjustments of the alignment during the initial stages of curing. Figure 4.12 shows a mounted cell attached to a light pipe.

4.4.5 Attachment of Light Pipes with Mounted Cells to Splitting Optics

Multiple cells were attached to light pipes at the same bandgap to allow for the selection of the highest efficiency cell-light pipe pair for integration into the prototype. Given the manual nature of the assembly, there existed the potential for variance in the efficiency of cells attached to optics due to incomplete coupling of the light pipe to the cell or damage caused to the cells during the attachment or PDMS cure steps. Champion light pipe-cell pairs were selected by measuring a current-voltage sweep of the photovoltaic cells while illuminating the input aperture of the light pipe under an AM1.5 solar simulator. Temporary electrical contacts were made to the legs of the chip carriers by applying two parallel strips of copper tape to a glass slide with wire leads soldered at the edge of the slide. The two strips of tape were separated by a distance equal to the distance between the sets of legs on the chip carrier. Beads of elemental gallium were dispensed on the copper tape and melted with a heat gun. The low melting point of gallium caused them to remain in the liquid state for 30 minutes following, allowing the light pipe with attached cell to be lowered until the feet of the carrier is immersed in the gallium, providing low resistance electrical contact to the device that was easy to align, easy to remove, and mechanically isolates the delicate device from the electrical test system.

Of the 2-3 light pipe-cell pairs at each bandgap, the best performing were then selected for attachment to the splitting optics. This process is described in great detail in the thesis of Cristofer Flowers and Carissa Eisler, who primarily performed this stage of the assembly process. In brief, however, this involved a sequential attachment, from highest to lowest bandgap, of each light pipe with attached photovoltaic cell. In order to attach each light pipe, the splitting optic was thoroughly cleaned with isopropyl alcohol and fabric applicators to remove residue and dust. Polyimide tape was attached to surfaces of the light pipe and the splitting optic in the vicinity of the attachment which were to remain unaffected such that any leakage of adhesive would be removed with the tape. A small volume of PDMS was dispensed via micropipette onto the splitting optic and the input aperture of the light pipe was placed in contact with it manually. A 3D printed jig was used to hold the light pipe in place, and the assembly was placed in a vacuum desicator for 30 minutes to remove any bubbles from the PDMS. Following degassing, the assembly was placed in an oven at 80 °C for 2 hours to cure the PDMS adhesive. The assembly was removed for visual inspection after 15 and then 30 minutes of curing. At these early stages of the cure the PDMS was not fully cured and any shifts in the alignment could be corrected with careful manual manipulation.

After curing, the polyimide tape was removed and the assembly cleaned again with isopropyl alcohol in preparation for the next light pipe attachment. This process was repeated six times until the prototype had seven light pipes with their respective photovoltaic cells attached, one for each spectral band of the splitting optic. The highest efficiency prototype, referred to as PSRv3 and analyzed in detail in chapter 5, is show in figure 4.13 along with a illustrative schematic and a ray trace model.

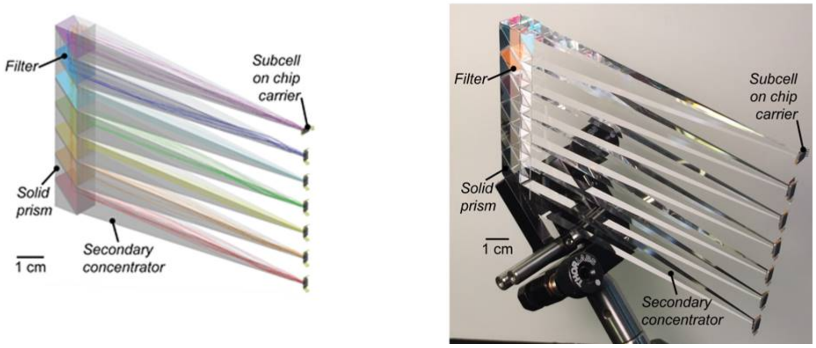

Figure 4.13: Ray trace simulation (left) of a PSR with 100x secondary concentrators and seven spectral bands along with an image of the fabricated prototype (right) of that design.

Chapter 5

PROTOTYPE CHARACTERIZATION AND PERFORMANCE

5.1 Summary of Three Prototypes

A series of three optoelectronic prototypes were fabricated sequentially according to the procedures described in chapter 4. The iterations allowed for multiple learning cycles and the incorporation of improved parts and procedures in each successive prototype. Ultimately, the highest combined power conversion efficiency was achieved in the third and final prototype, and that was 30.2% efficiency, as measured via seven independent two-terminal DC measurements under the AM1.5D solar spectrum. In this chapter the performance of the three polyhedral specular reflector spectrum-splitting prototypes is described, including the methods of characterization, sources of loss relative to the optoelectronic design, and pathways to recover those losses in future work.

A summary of the distinguishing characteristics of the three integrated prototypes is provided in table 5.1. The first prototype, herein referred to as V1, featured 25 mm long secondary concentrators with a square input face 1 cm on a side and a square output face 2.5 mm on a side, for 16x geometric gain. These coupled to solar cells with square active areas 2.9 mm on a side, which includes the illuminated area of 2.5 x 2.5 mm, along with 0.2 mm in each dimension for alignment tolerance, and 0.1 mm along each edge for the electrical contact. At the time of the fabrication of prototype v1 photovoltaic devices had been grown and processed at only four unique bandgaps, and thus several bandgaps were utilized for multiple spectral bands. For prototype v2, devices were incorporated at all seven bandgaps. Additionally, higher secondary concentration was utilized in order to reduce the influence of perimeter recombination on the photovoltaic devices. This higher optical concentration resulted from 100 mm long light pipe concentrators which had square input faces 1 cm on a side and square output faces 1 mm on a side. These were coupled to cells with square active areas 1.2 mm on a side, with an additional 0.1 mm along each edge for the electrical contact. This configuration was retained for prototype v3, with adjustments made in the fabrication and assembly processes based on information learned from prototype v2.

Build Order	Name	Secondary Concentration	Unique Bandgaps	Splitting Efficiency	Power Conversion Efficiency
1	PSRv1	16x	4	90.1%	22.9%
2	PSRv2	100x	7	86.8%	22.4%
3	PSRv3	100x	7	88.1%	30.2%

Table 5.1: Summary of properties and performance of three spectrum splitting polyhedral specular prototypes.

5.2 Characterization Methods

In order to understand the performance of individual components and their assembled structures, two optoelectronic characterization methods were employed extensively. They were broadband collimated illumination from an Abet 2000 solar simulator, and monochromatic collimated illumination in a custom set-up referred to as Spectral and Angular Resolved Photocurrent (SARP). The solar simulator was utilized for the final module efficiency measurements, but the SARP setup provided spectrally resolved information about the optical efficiency and external quantum efficiency of the components and assembled module.

5.2.1 Spectral and Angular Resolved Photocurrent

The SARP characterization setup provided a wavelength dependent measure of both how efficiently optical components transmitted incident light to desired outputs, and how efficiently photovoltaic cells collected incident light and generated photocurrent. This was achieved by passing collimated monochromatic light into the optical or optoelectronic assemblies under test and measuring either the transmitted light or the electrical response of constituent photovoltaic cells.

A Fianium model SC400 supercontinuum laser output a collimated broadband beam spanning the spectral range of 400 to 1700 nm which was of interest in this work. This white-light beam was passed into a Thermo Oriel model 77700 grating monochromator with integrated filter wheel. The resulting monochromatic beam is passed through a chopper wheel with chopping frequency between 10-100 Hz, allowing the noise from ambient light to be filtered out by a lock-in amplifier. This chopped beam was split with one portion proceeding to a reference photodiode to monitor the power output of the laser in real time, providing a correction for temporal variation in the laser output power. The remainder of the beam was passed through a series of collimating and beam expanding optics, before passing through an aperture and

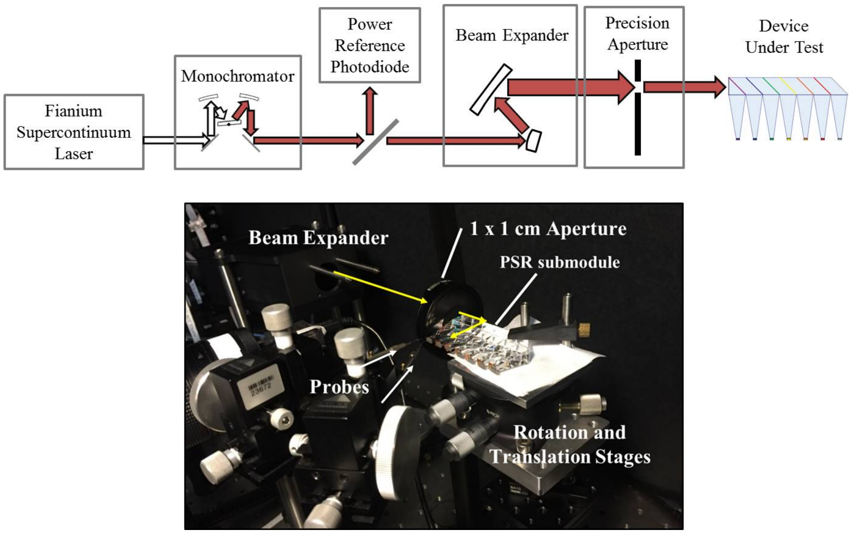

Figure 5.1: A schematic of the SARP characterization apparatus along with an annotated image of the measurement configuration.

onto the device under test. The apertures used were square apertures sized precisely to the size of the optical components being measured, such that the entire input area is equally probed. The edges of the input faces of integrated optics are likely lower optical efficiency than nearer the center, as alignment errors and surface imperfections manifest themselves first in those areas. Thus, by fully illuminating the input faces of devices under test, we do not overestimate the true optical performance.

The optical efficiency or external quantum efficiency of the optical components or optoelectronic assemblies was then measured in one of two ways. For purely optical components, including splitting optics, secondary concentrators, and integrated splitting and concentrating sub-assemblies, the optical efficiency was measured by placing a calibrated photodiode at the output face of the relevant optic. The calibrated photodiode was either a Si or Ge photodiode depending on the spectral range being measured. For optoelectronic devices, including bare photovoltaic cells, cells attached to secondary concentrators, or fully assembled prototypes, the measurement signal came not from a photodiode but by measuring the short circuit current of each photovoltaic cell under test.

The current signal from the photovoltaic cells or reference photodiodes was passed into a preamplifier and converted into a voltage signal with 40-50 dB of gain applied. The voltage signal was passed to a lock-in amplifier locking in on a signal from the chopper wheel. Finally, a Keithley Instruments model 6430 source-measure unit was used to maintain zero bias across the photovoltaic cell or reference photodiode, compensating for any impedance in the electrical test equipment that would drive the cell away from zero bias. This ensured that the short-circuit current was measured, and any finite shunt resistances did not affect the optical efficiency measurements.

5.2.2 Solar Simulator

Final system efficiency measurements on assembled prototypes were performed with collimated broadband illumination from a AAA-rated ABET model 2000 solar simulator featuring a spectral filter matched to AM1.5D. To measure the seven independently connected photovoltaic cells in an assembled PSR prototype, seven sequential measurements were performed by connecting four-point probes to the electrical leads of the chip carriers. Thin gold wires attached to probe tips were used to make the electrical connection so as to minimize any forces applied to the devices.

The lamp power was adjusted to compensate for deviations in photocurrent in each spectral band. The lamp power was adjusted up or down until the measured short-circuit current matched the expected short-circuit current calculated from integrating the external quantum efficiency measured via SARP against the AM1.5D spectrum. This power adjustment was typically insufficiently precise, and final adjustments were made by translating the measured current-voltage curve by the difference between the short-circuit current determined by the external quantum efficiency and the measured short-circuit current.

During the measurements under the solar simulator, the prototypes were clasped by an optics mount at the last prism to minimize contact area with surfaces relying on total internal reflection. The input was aperture by a bulk aperture six inches above the prototype, and a precision aperture directly above the input face of the prototype. The measurement configuration is shown in figure 5.2.

5.3 PSRv1

The first prototype that integrated splitting and concentrating optics with photovoltaic cells, referred to here as PSRv1, exhibited a sum DC power conversion efficiency of 22.9% under AM1.5D. This prototype featured 16x secondary concentrating light pipes with 2.5 mm output faces mated to seven photovoltaic cells. However, due to delays in the epitaxial growth and device processing at several bandgaps, this first prototype incorporated only four unique bandgaps. Table [TABLE] describes the substituted photovoltaic cells in PSRv1.

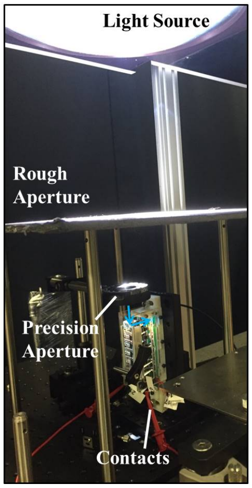

Figure 5.2: The configuration of measurements made under broadband collimated light provided by an ABET 2000 solar simulator.

Cell Order	Design Bandgap (eV)	Actual Bandgap (eV)
1	2.10	0.74
2	1.78	1.54
3	1.54	1.54
4	1.42	1.42
5	1.15	0.74
6	0.93	0.74
7	0.74	0.74

Table 5.2: Intended and actual device bandgaps for the seven photovoltaic cells in PSRv1.

The photovoltaic cells utilized in PSRv1 had inverted square top-contact patterns with a square active area of 2.7 mm wide, offering 0.2 mm of alignment tolerance in each dimension. A schematic of the top contact is shown in figure 5.3.

5.3.1 Performance of PSRv1

The optical response of the assembled splitting optic was measured via SARP prior to attachment of secondary concentrators, and it exhibited a splitting efficiency of 90.1%. That measure means that the expected power output of the designed ensemble of cells, as calculated via modified detailed balance, while illuminated by the spectrum generated by the splitting optic, is equal to 90.1% of the power generated by the same ensemble of cells under a perfectly split AM1.5D spectrum.

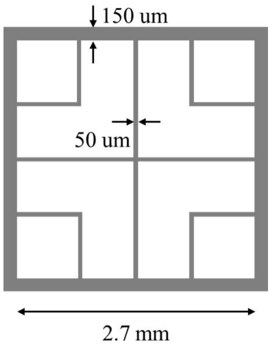

Figure 5.3: A schematic of the top contact grid for all devices incorporated in prototype PSRv1.

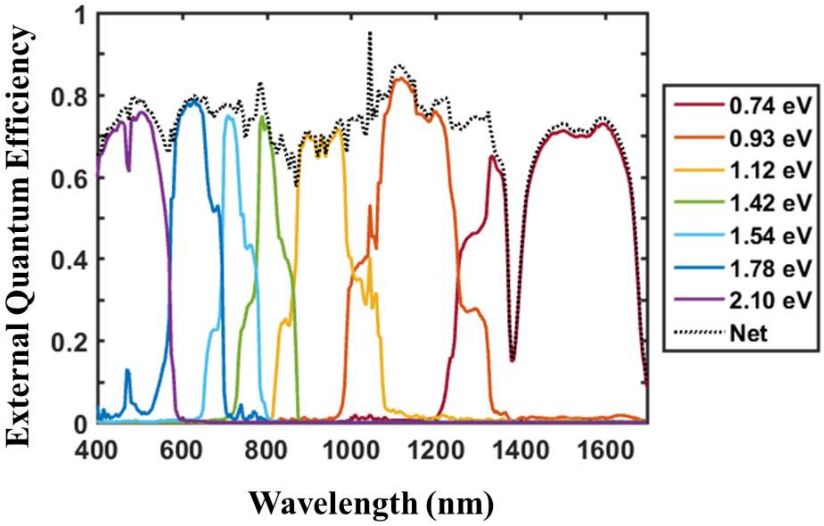

Figure 5.4: The external quantum efficiency of PSRv1. Current collected in each of the seven different photovoltaic cells is depicted by a different color, and the sum is represented by the dashed black line.

The external quantum efficiency of the integrated prototype was similarly measured via SARP, and that is depicted in figure 5.4

The set of measured current-voltage traces of PSRv1 under solar simulator illumination is shown in figure 5.5, and the device IV parameters are highlighted in table 5.3. Aside from the bandgap substitutions, there are two features of the performance of the cells of note. They are that the fill factors and open-circuit voltages are lacking relative to their designed levels. Additionally, the one-sun open circuit volt-

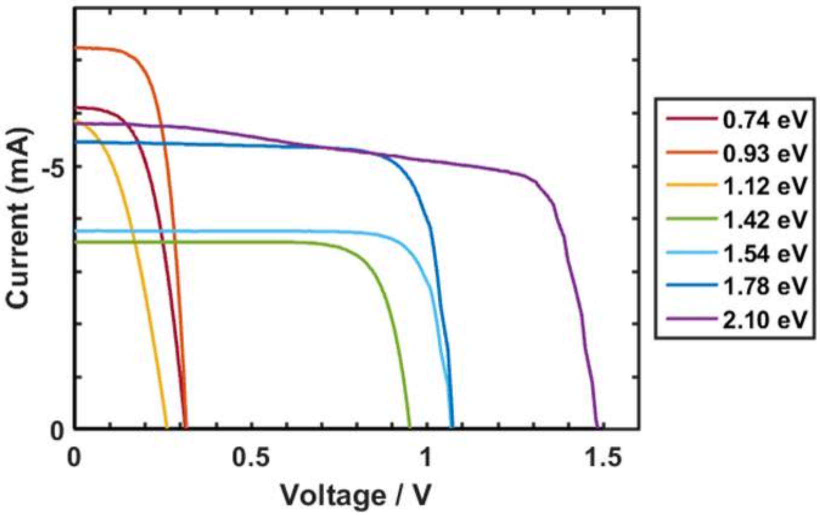

Figure 5.5: Current-Voltage traces from PSRv1 under AM1.5D illumination from a solar simulator. Substituted cells with bandgaps different than the intended bandgap are indicated with an *.

ages of the devices fabricated for PSRv1 were lower than the on-wafer qualification measurements performed by Spectrolab.

Bandgap (eV)	V_{oc} (mV)	I_{sc} (mA)	FF (%)
2.1	1485	5.7	71.9
1.78*	1065	6.1	77.2
1.54	1062	3.7	80.2
1.42	962	3.9	78.3
1.15*	260	5.8	52.3
0.93*	323	7.5	62.9
0.74	315	6.1	53.2

Table 5.3: Current-Voltage characteristics of the photovoltaics cells as measured in the integrated spectrum splitting prototype PSRv1 under AM1.5D illumination.

As part of the qualification of the epitaxial growths, Spectrolab processed wafers from the same epitaxial growths into photovoltaic cells without performing epitaxial lift-off. This "on-wafer" configuration generally exhibited undesirable fill factors and current collection, owing to the inverted growth and lack of back mirror. However, the open-circuit voltages were used to qualify the material quality of the growth. The reduction of open-circuit voltage of the cells processed in the lifted-off configuration relative to the on-wafer configuration raised the possibility that the lift-off processing was damaging the cells in some manner.

5.3.2 Perimeter Recombination

One possible explanation for the voltage degradation was minority carrier recombination at the perimeter. The on-wafer measurements were performed on square cells one centimeter on a side. The lift-off cells in PSRv1 were 2.9 mm on a side, resulting in more than three times as much perimeter length per unit area. In addition to their smaller size, the chemistry of the mesa etch used to define the device area and expose their sidewalls perhaps differed from the unknown proprietary process utilized by Spectrolab. Even if the etchants were identical, in the lifted-off configuration the metallic rear mirror, featuring a thin Ni layer, and potentially also Cu from the handle were exposed to the etch. It was conceivable that the sidewalls of the devices were more active recombination centers when exposed to metals than when not exposed to metals as in the on-wafer processing.

Tests were performed using five different mesa etch chemistries to determine if the chemical state of the sidewalls was contributing to excessive recombination and concomitant open-circuit voltage loss. The mesa etch process utilized for PSRv1 cell fabrication is the same as described in chapter 4, and consisted of alternating etches of a phosphoric acid:hydrogen peroxide:water (3:4:1) mixture and concentrated hydrochloric acid. Four other etch systems were taken from literature reports, and all five are described in table 5.4.

Etch System	Arsenide Etchant	Phosphide Etchant
1	H_3PO_4:H_2O_2:H_2O (3:4:1)	HCl (Conc.)
2	$C_6H_8O_7$:H_2O_2 (4:1)	HCl (Conc.)
3	HNO_3:HCl:H_2O (1:1:1)	HCL (Conc.)
4	HNO_3:HCl (1:4)	HCL (Conc.)
5	Etch 1 followed by brief Etch 4	

Table 5.4: Description of wet chemical etchants tested for suitability as mesa etchants as shown in figure 5.6.

To assess the influence of the five etch systems on sidewall recombination, diodes were fabricated on lift-off films of 1.42 eV GaAs samples. Diodes, with their entire top side metalized rather than a sparse contact grid to allow light absorption as in a solar cell, were chosen as a test platform to simplify the experiment. Measuring the forward bias recombination current in the dark is a good proxy for the open-circuit

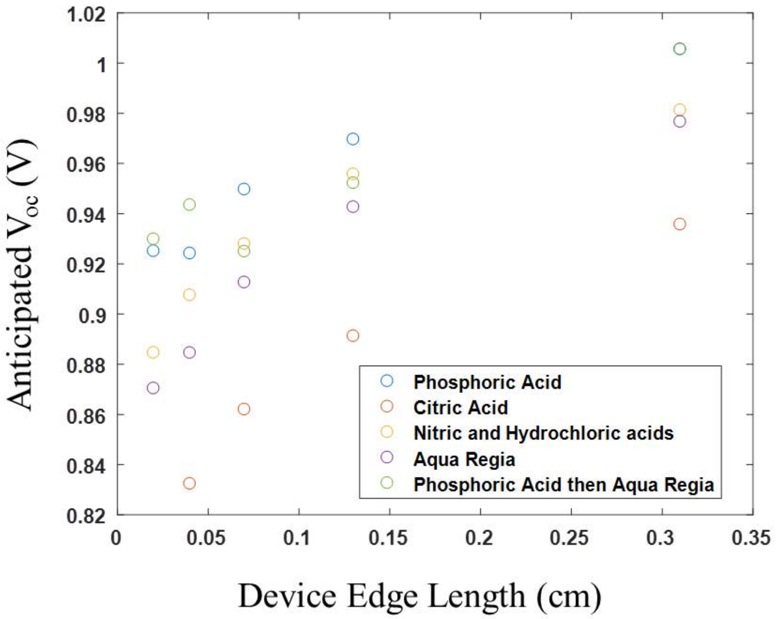

Figure 5.6: Anticipated V_{oc} of square GaAs diodes of varying side length and processed with different wet chemical mesa etches.

voltage as the superposition principle is well obeyed around the open circuit voltage. Furthermore, by metalizing the entire front surface series resistance is significantly decreased, further supporting the superposition principle. Additionally, making a fair comparison of open-circuit voltage under illumination would require careful design of the contact grids, to ensure equal shadow fraction and current collection. Finally, by not illuminating the devices, transient thermal effects that could distort the measurement are reduced.

Therefor the figure of merit for comparing the performance of the diodes fabricated with different mesa etch chemistries was the anticipated open-circuit voltage, which is the voltage at which the forward bias recombination current in the dark was equal to some arbitrary short-circuit current, taken to be 10 mA/cm^2 here. Measuring this anticipated open-circuit voltage of diodes at various sizes and mesa etch chemistries illustrated the impact of perimeter recombination on the devices. The anticipated open-circuit voltages from these measurements are shown in figure 5.6.

Figure 5.6 shows clearly that the phosphoric acid based mesa etch process is superior to the other etch chemistries, and that changing to one of them would likely further degrade device performance. Furthermore, qualitative extrapolation of the

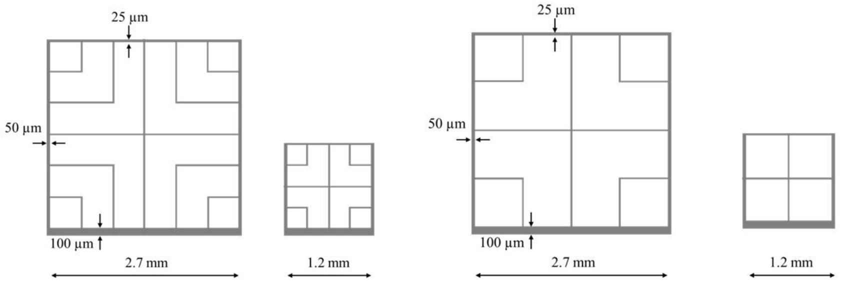

Figure 5.7: Schematics of top contact grids for two different sizes of photovoltaic cells, each with a separate grid design for InP and GaAs based devices.

anticipated open-circuit voltages measured for phosphoric acid etched diodes shows that the surface recombination velocity (SRV) of the 2.9 mm wide lifted-off devices is likely not worse than the 1 cm wide on-wafer devices, and that the voltage loss is due to increased perimeter to area ratio rather than increased SRV.

One method for reducing the impact of perimeter recombination in small devices is to operate at higher optical concentration. Greater short-circuit current pushes the open-circuit voltage higher and reduces the portion of total recombination which is non-radiative. This is due to the lower ideality of radiative recombination mechanisms relative to non-radiative recombination mechanisms, excluding Auger recombination which is not relevant in III-V material systems until very high injection levels. Therefore, in preparation for the second prototype photovoltaic cells were fabricated at two sizes, corresponding to the two available sizes of secondary concentrators. Additionally, at both sizes a separate top contact grid pattern was employed for the three lowest bandgap InP devices and the four higher bandgap GaAs based devices, on account of the slightly higher sheet resistance in the InP based devices. Diagrams of these four devices are shown in figure 5.7.

In order to quantitatively measure the impact of perimeter recombination in these devices dark current-voltage traces were taken. At low voltages variations in shunt resistance between devices renders the data unreliable, but in the vicinity of the short-circuit current densities, superposition applies well and we can extract useful parameters from the data. Comparing the current densities of the two different cell sizes at the same voltage for each bandgap allows us to fit parameters for a simple model of perimeter recombination. Figure 5.8 depicts the dark current densities under forward bias for two sizes of 1.42 eV GaAs cells, with the curret densities at the open circuit voltage of the smaller cell indicated.

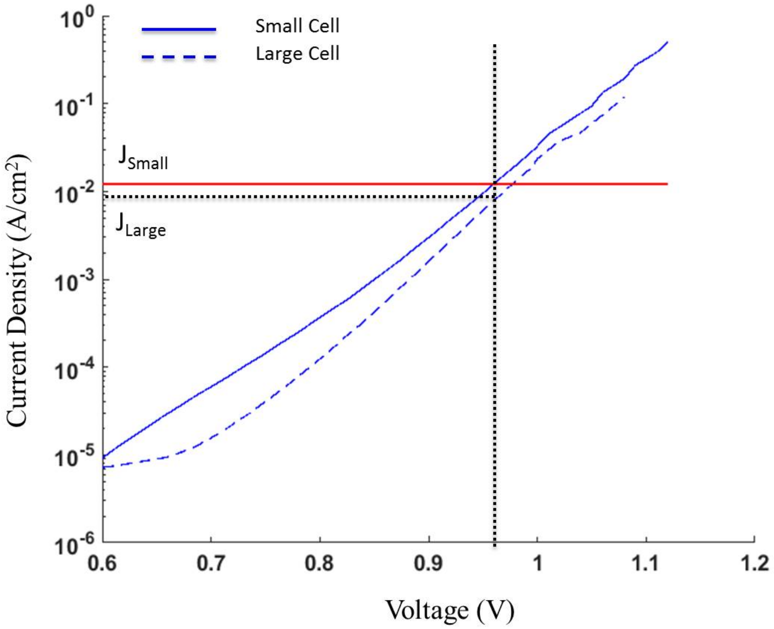

Figure 5.8: Dark current-voltage traces of two different sized photovoltaic devices. Current densities of both devices at a specific voltage are indicated by horizontal lines.

If we assume that the forward bias recombination current is the sum of a an area-dependent current density and a perimeter-dependent linear current density, than the current densities of the two different cell sizes provides a solvable system of equations as shown in equations 5.1 and 5.2.

$$J_{small} = J_{Bulk} + J_{Perimeter} * \frac{4}{L_{small}} \tag{5.1}$$

$$J_{large} = J_{Bulk} + J_{Perimeter} * \frac{4}{L_{large}} \tag{5.2}$$

Similarly, these parameters can be extracted for devices at each bandgap. Figure 5.9 shows dark current densities under forward bias for devices at two sizes for each of the seven bandgaps under consideration.

We can use this model to directly estimate the open circuit voltage loss due to perimeter recombination relative to a 1 cm wide cell in the smaller cells fabricated for the spectrum splitting prototypes. Table 5.5 summarizes the open circuit voltages measured for large cells on wafer and lifted-off small cells. The voltage loss at open

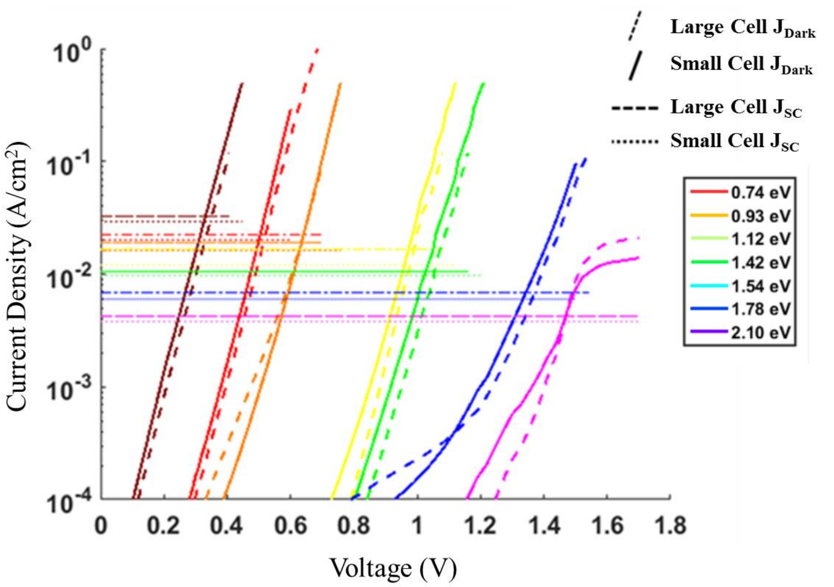

Figure 5.9: Dark current-voltage traces of two different sizes of photovoltaic cells at seven bandgaps. Horizontal lines indicate 1-sun short circuit currents.

circuit resulting from perimeter recombination for illumination from one spectral band and 100 times each spectral band is also noted, showing that although at low illumination levels the voltage loss is several tens of mV per cell, at 100x in-band currents the voltage loss becomes much less significant. Of note is that the 1.15 eV cell is hardly impacted at all by the perimeter recombination, indicating that the growth quality is poor and that non-radiative bulk recombination dominates even at small cell sizes. It should be noted that the devices measured in the on wafer configuration and the lifted-off configuration were not merely separate wafers, but separate epitaxial growths. The 0.93 and 1.15 eV cells were not measured on wafer with an incorporated epitaxial lift-off layer. Thus, the epitaxial growths incorporating sacrificial AlAsSb ELO layers need further development to raise the material quality of the quaternary absorber.

Solving this system for each of the seven bandgaps provides a quantitative answer to the fraction of total recombination which is due to the perimeter. However, these are voltage dependent terms, and in order to estimate how the impact of perimeter recombination will scale with higher voltage or higher optical concentration, we must assume an additional simple model. First, we assume that the area-dependent current density is dominated by radiative recombination with an exponential ideality of 1. Next, we assume that the perimeter recombination is non-radiative and scales

	$(1\ \text{cm})^2$ 1 Sun On Wafer	$(1.4\ \text{mm})^2$ 1 Sun Lifted-Off	$(1.4\ \text{mm})^2$ 1 Sun In-Band Under Optics	$(1.4\ \text{mm})^2$ 100 Suns In-Band Under Optics
Eg (eV)	V_{OC} (mV)	V_{OC} (mV)	ΔV_{OC} (mV)	ΔV_{OC} (mV)
0.74	414	314	28	7
0.93	601	478	23	4
1.15	787	619	2	0
1.42	1052	951	28	5
1.54	1119	1021	65	13
1.78	1402	1323	54	6
2.10	1463	1427	45	3

Table 5.5: Summary of the open circuit voltages measured for large $(1\ \text{cm})^2$ cells on wafer and small cells $(1.4\ \text{mm})^2$ after epitaxial lift-off, along with the modeled voltage loss at open circuit due to the perimeter recombination of small cells at two levels of optical concentration.

with an exponential ideality of two. This double diode model is described in equation 5.3. This double diode model offers a quantitative estimation of the dependence of open-circuit voltage on both cell dimension and optical concentration level, based on actual measurements of cells at two sizes. Figure 5.10 maps out the anticipated open-circuit voltage as a function of cell size and in-band optical concentration for all seven bandgaps.

$$J_{Total} = J_{Bulk} * e^{\frac{qV}{k_B T}} + J_{Perimeter} * e^{\frac{qV}{n_2 k_B T}} \tag{5.3}$$

5.4 PSRv2

The second integrated prototype, PSRv2, consisted of a spectrum splitting stack assembled in the same manner as PSRv1, but featured longer secondary concentrators and smaller photovoltaic cells. The light pipe secondary concentrators were 100 mm long with the same 1 cm wide input face but a smaller 1 mm output face, resulting in 100x geometric concentration. The photovoltaic cells were 1.4 mm wide, including 1.2 mm of active area providing 0.2 mm of alignment tolerance in each dimension, and 0.2 mm of ring contact and mesa exclusion zone.

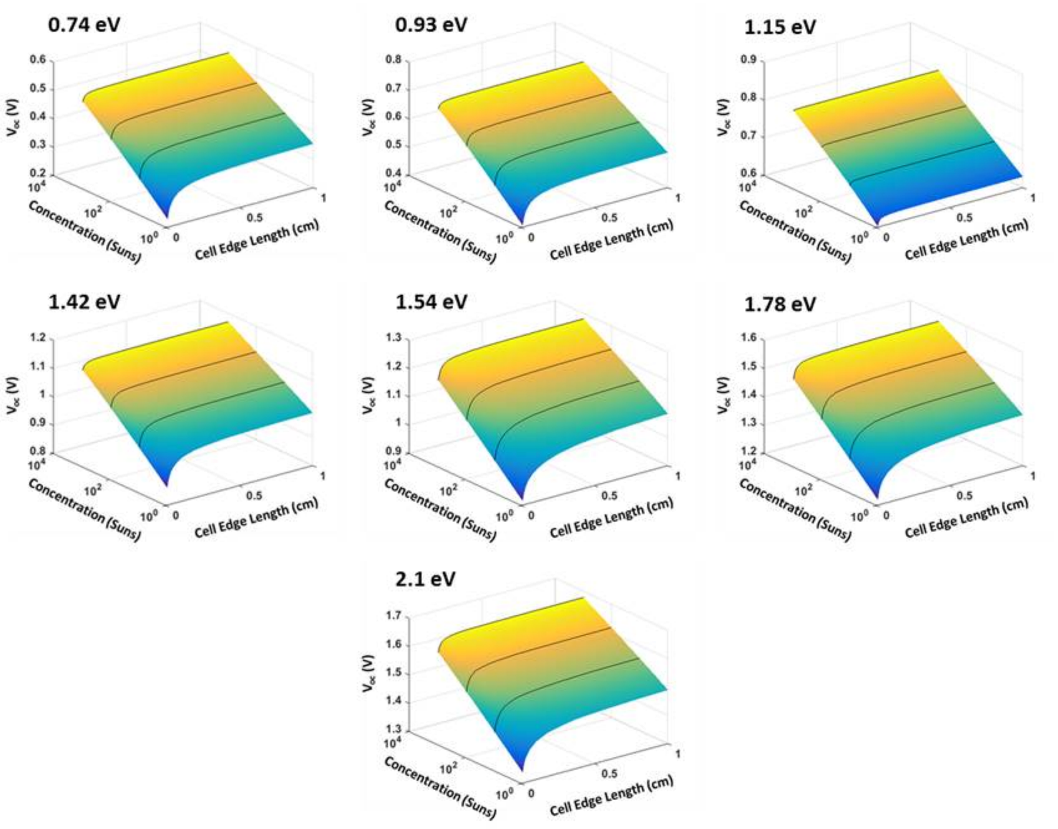

Figure 5.10: Set of plots for each device bandgap showing relationship between the level of in-band optical concentration and the size of the device on the open-circuit voltage.

5.4.1 Performance of PSRv2

The splitting efficiency of the splitting optics was measured via SARP at 86.8%, a slight decrease relative to PSRv1 and owing to misalignment of the prism units, as well as several air bubbles present in the adhesive layers which cause scattering and reflection of the incident beam. The splitting efficiency of PSRv2 is shown in figure 5.11.

Despite the longer optical path length in the 100 mm light pipes relative to the 25 mm light pipes, the fused silica is transparent enough that volumetric absorption is negligible. The measured wavelength dependent transmission efficiency of the 100 mm light pipe is shown in figure 5.12, and this corresponds to an optical efficiency of 97.6% for AM1.5D. This compares with 98% optical efficiency calculated by ray-tracing the light pipe, assuming optical properties of the fused silica provided by the manufacturer, and entirely specular surfaces. This is good evidence that

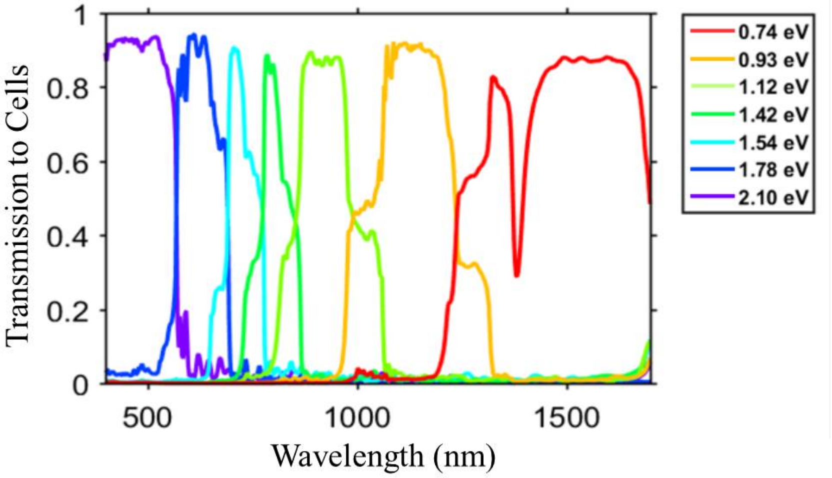

Figure 5.11: Reflectance of optical splitting prism used in PSRv2, demonstrating the spectral allocation to each of the seven photovoltaic cells.

scattering within the volume and along the surfaces of the light pipes is negligible and thus adhered dust and chipped corners of the light pipes are tolerable defects.

The sum DC power conversion efficiency of the seven independent photovoltaic cells in PSRv2 was measured to be 22.4%. This compares unfavorably with the 22.9% efficiency of PSRv1, particularly so when considering that PSRv2 featured a full suite of seven photovoltaic cells at the designed bandgaps, with not sub-optimal substitutions as in PSRv1. Additionally, PSRv2 featured higher secondary optical concentration, which should have resulted in higher open-circuit voltage and fill factor for the cells.

The external quantum efficiency of PSRv2 is shown in figure 5.13 as measured via SARP. Of note is the generally low values compared to PSRv1. The integrated current collection of PSRv2 summed to 28.2 mA, just over 53% of the available current in AM1.5D. This is a significant reduction from the 38.8 mA collected by PSRv1, representing 73.1% of the available photocurrent.

The current-voltage traces of the seven cells are shown in figure 5.14, with their extracted curve parameters listed in table 5.6. As is apparent from both the short-circuit currents listed in table 5.6 and the external quantum efficiency of PSRv2 show in 5.13, the current collection efficiency of the cells in PSRv2 was significantly less than PSRv1 and was the dominant cause of the poor efficiency. The optical splitting subassembly was not the the source of the poor current collection, as it

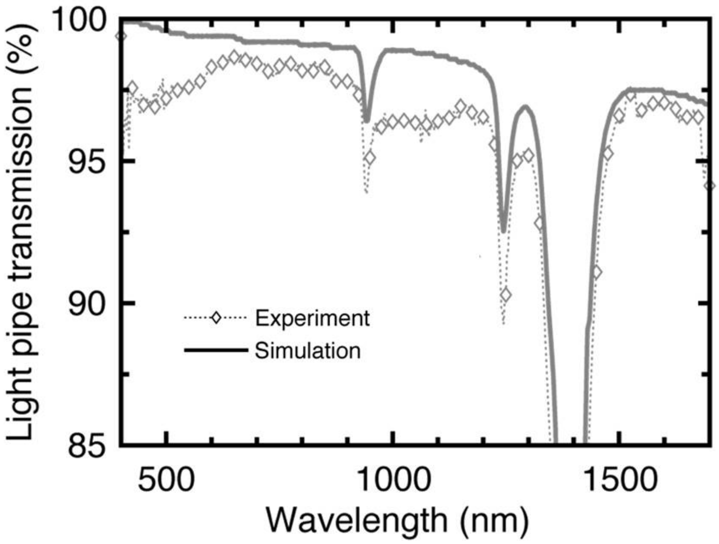

Figure 5.12: Wavelength dependent transmission through the 100 mm long straight-walled light pipes utilitzed in PSRv2. The simulation data was taken from ray-tracing simulations an compared with measurements from SARP.

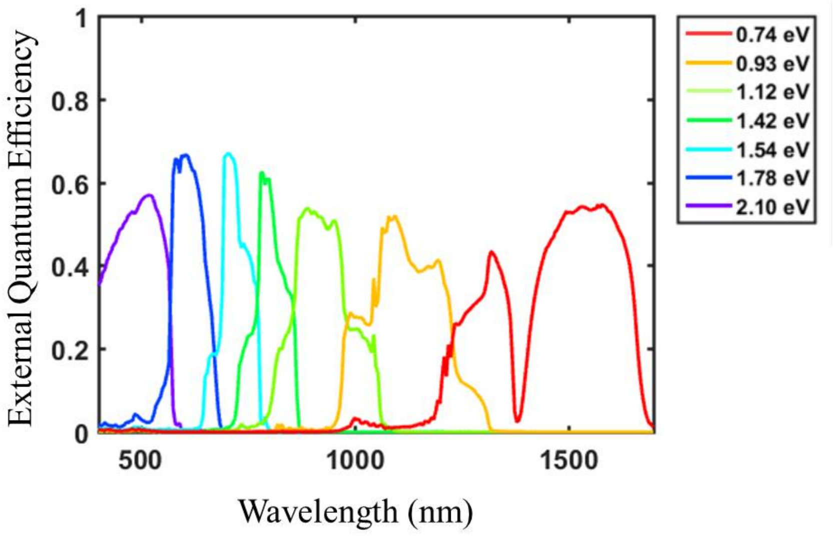

Figure 5.13: The external quantum efficiency of PSRv2 as measured via monochromatic excitation with SARP apparatus.

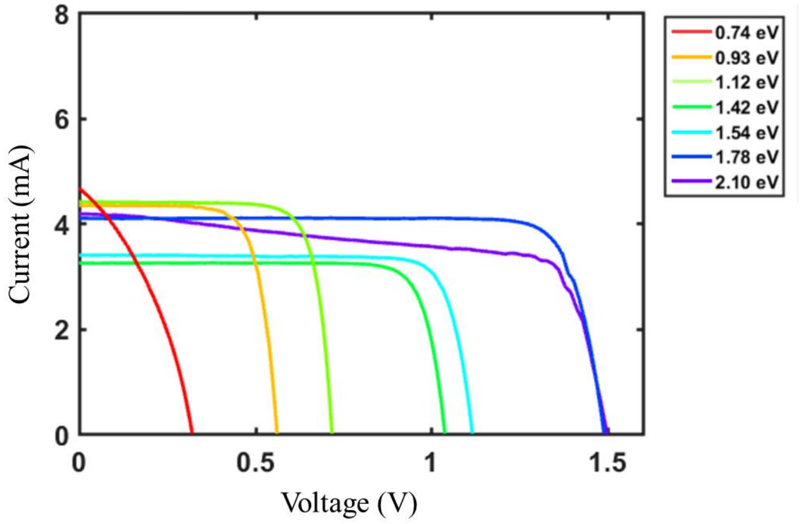

Figure 5.14: The current-voltage traces of the photovoltaic cells in PSRv2 under broadband illumination from a solar simulator.

had been independently characterized and showed good performance. Similarly, the photovoltaic cells themselves were measured under one-sun illumination, and their short-circuit currents were larger than would be implied by the poor photocurrent exhibited by the integrated prototype.

Bandgap (eV)	V_{oc} (mV)	I_{sc} (mA)	FF (%)
2.1	1499	4.2	69.8
1.78	1490	4.1	83.4
1.54	1117	3.4	82.3
1.42	1038	3.2	82.6
1.15	718	4.4	78.6
0.93	562	4.3	74.0
0.74	321	4.6	37.1

Table 5.6: Current-Voltage characteristics of the photovoltaics cells as measured in the integrated spectrum splitting prototype PSRv2 under AM1.5D illumination.

5.4.2 Optical Couping to Cells

The remaining likely source of the lost photocurrent is the optical coupling between the photovoltaic cell and the output face of the light pipe concentrator. Visual examination of that interface revealed several possible sources of loss. First, PDMS

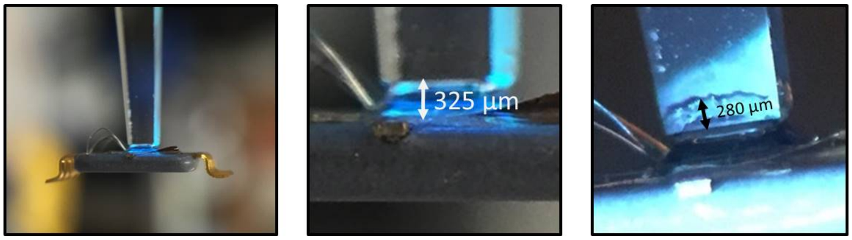

Figure 5.15: Images of the attachment between a photovoltaic cell and a 100x light pipe in PSRv2. The width of the gap filled with PDMS in this, the 2.1 eV cell, is measured at approximately 325 um and there is approximately 280 um of PDMS wicked up the side of the light pipe.

appeared to have wicked up along the sidewalls of the light pipes, owing to the low surface energy between the PDMS and the fused silica light pipe. This wicking resulted in a PDMS boot around the light pipes in the vicinity of several hundred μm from the output face. Second, the thickness of PDMS observed in this interface ranged from 250-400 μm in thickness. These two features are depicted in figure 5.15, showing the coupling of the highest bandgap cell to the light pipe in PSRv2.

Ray-tracing analysis was performed to assess the impact of these imperfections at the cell-light pipe interface on the optical coupling efficiency. A model was built of a light pipe with a variable height of PDMS around the light pipe near the output face. In the worst-case scenario, any rays striking this PDMS would be lost. This is possible if the PDMS is thick enough to destroy the shape accuracy of the light pipe, and allow internally reflected rays to strike the plane of the cell outside of its active area. Additionally, the surface of the PDMS boot was observed to have some significant roughness relative to the polished faces of the light pipe, and this roughness could cause a significant fraction of light to be scattered out of the light pipe before striking the cell, since the light intensity at the tips of the light pipes is very high.

Figure 5.16 depicts the set of simulations analyzing the potential losses from the PDMS boot for heights from 0 to 500 μm. Furthermore, because the PDMS boot may increase the sensitivity of the coupling efficiency to the angular distribution of light within the light pipe, simulations were performed assuming perfect specular reflection each time a ray struck a surface of the light pipe, as well as assuming 99.5% specular reflection with 0.5% Lambertian component. It is apparent from this plot that the loss of coupling efficiency, plotted as fraction of power transmitted to the cell, increases nearly linearly with PDMS boot height. However, it is likely that this

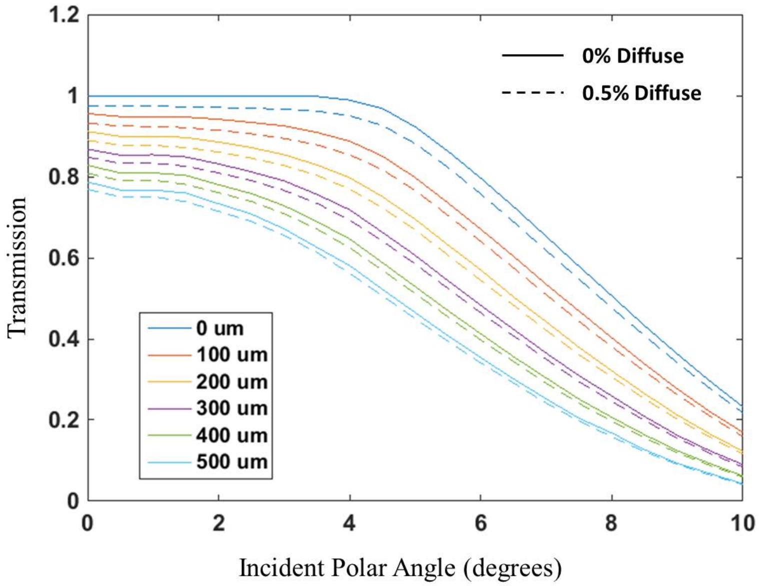

Figure 5.16: Maximum possible loss in the light pipes due to PDMS wicking or enveloping the sidewalls of the light pipes as calculated via ray tracing.

model which assumes any light incident on the PDMS boot is lost overestimates the actual impact. It illustrates that nearly 20% of the incident light is reflected by the light pipe within 400 μm of the output face, and thus this region of the light pipe must be kept clean and free of defects to the greatest extent possible.

The second issue with the PDMS coupling was its thickness and the distance between the output face of the light pipe and the surface of the photovoltaic cell. Another ray-tracing model was built to estimate the impact of the beam spreading and missing the cell active area due to a gap. In this analysis, cell receivers of both 1 x 1 mm and 1.2 x 1.2 mm in dimension were examined. This reflects the fact that the cells as used in the prototype were designed to have an active area of 1.2 x 1.2 mm, providing 0.1 mm of alignment tolerance along each edge. Therefore, if the cell is perfectly aligned with the light pipe, then the 1.2 mm wide receiver accurately represents the prototype. However, depending on the extent of rotational and translational misalignment, the reality may lie closer towards the 1 mm receiver. Figure 5.17 depicts a cross-section of the ray-trace model as well as the resulting data from the simulations.

This set of simulations shows clearly that if the PDMS coupler is 100 μm thick or less, that a well aligned cell will not suffer and loss in photocurrent out to nearly

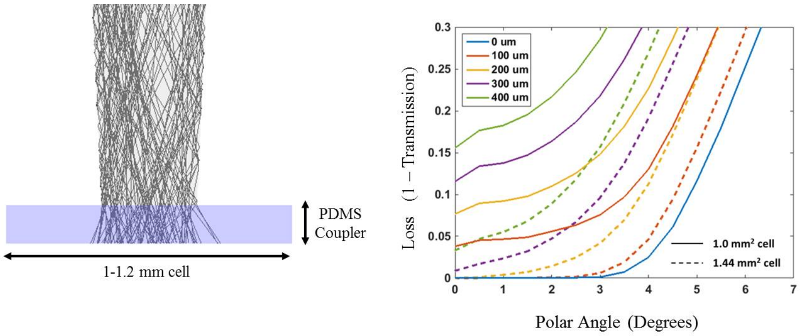

Figure 5.17: Optical loss due to the thickness of PDMS coupler between photovoltaic cell and light pipe. Loss results from lateral spreading of the beam as it exits the light pipe.

3 degrees of polar incidence, hardly worse than an infinitely thin PDMS layer. It is also apparent that the impact of misalignment of the cell is exacerbated by the thickness of the PDMS coupler. These simulations clearly support the importance of controllably fabricating a thin PDMS coupler to promote good optical coupling between the light pipe and the cell. It was determined that the original cell-to-light pipe attachment procedure, which involved aligning the two with a jig set on a series of manual stages and then baking the PDMS by placing the entire jig in an oven, was giving rise to the distortion of the PDMS coupling. As attached the PDMS layer was thin but the thermal expansion of the metal stages and breadboards created a separation between the cell and the light pipe. This also explained the appearance of the PDMS of being drawn-up from the cell. This problem was solved by spin coating PDMS onto the cells and then applying heat locally with a heat gun to avoid the expansion of the surrounding jig, and to allow in-situ adjustment of the alignment height. This modified attachment process is the process of record described in chapter 4.

5.5 PSRv3

The third PSR prototype incorporated lessons learned from the first two, and consequently exhibited the highest DC power conversion efficiency of all of them, at 30.2% under AM1.5D. Like PSRv2, this prototype incorporated smaller cells under higher concentration to mitigate perimeter recombination as learned from PSRv1. The cells were attached to the light pipes with excellent optical coupling due to learning from PSRv2. Finally, the value of redundancy and intermediate quality checks was demonstrated during the fabrication of PSRv1 and PSRv2, and thus significantly more photovoltaic cells were fabricated to allow for the selection of champion devices at several points along the fabrication process, and to have back-ups if champions suffered damage.

5.5.1 Performance of PSRv3

The integrated optical efficiency of PSRv3, from the input aperture to the output of the light pipes, was determined to be 84.5%. This number reflects the product of independent measurements of the transmission of the broadband anti-reflection coating, the splitting prism, and the secondary light pipes. The splitting optical efficiency alone was measured to be 88.1%, slightly higher than PSRv2 but lower than PSRv1. This range reflects variation due to the manual attachment process of the prism pieces, including misalignment between prism pieces and small bubbles in the PDMS adhesive between them, as well as a measurement uncertainty on the order of 0.5%. The optical splitting performance of the splitting prism in PSRv3 is depicted in figure 5.18.

Figure 5.19 depicts the set of current-voltage traces under AM1.5D illumination, adjusted to the appropriate spectral flux as determined by SARP measurements. The sum DC power conversion efficiency from these seven cells was 30.2% of the incident optical power, and the IV parameters are denoted in table 5.7.

Bandgap (eV)	V_{oc} (mV)	J_{SC} (mA/cm^2)	FF (%)
0.74	350	4.87	60.7
0.93	539	5.41	74.6
1.15	784	6.58	80.6
1.42	1061	3.88	82.1
1.54	1148	4.00	83.3
1.78	1501	4.49	82.5
2.10	1534	5.97	76.5

Table 5.7: Current-Voltage parameters of the photovoltaic cells as illuminated in the spectrum splitting prototype PSRv3.

Current Collection

The photocurrent generated by the seven cells of PSRv3 summed to 35.2 mA/cm2, which represents 66.3% of the available photocurrent in the spectrum and 83.1% of the targeted photocurrent. That the photocurrent did not reach the design target reflects two separate sources of loss. First, the top contact grids exhibited a larger

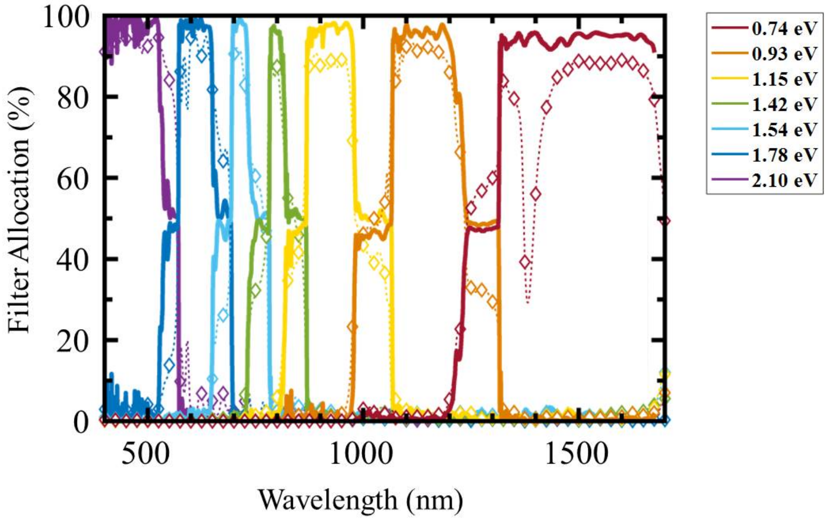

Figure 5.18: The splitting performance of the splitting prism utilized in PSRv3. The efficiency of photons allocated to each spectral band is indicated as modeled (solid line) and as measured (dashed line with markers). Figure developed by Dr. Cris Flowers.

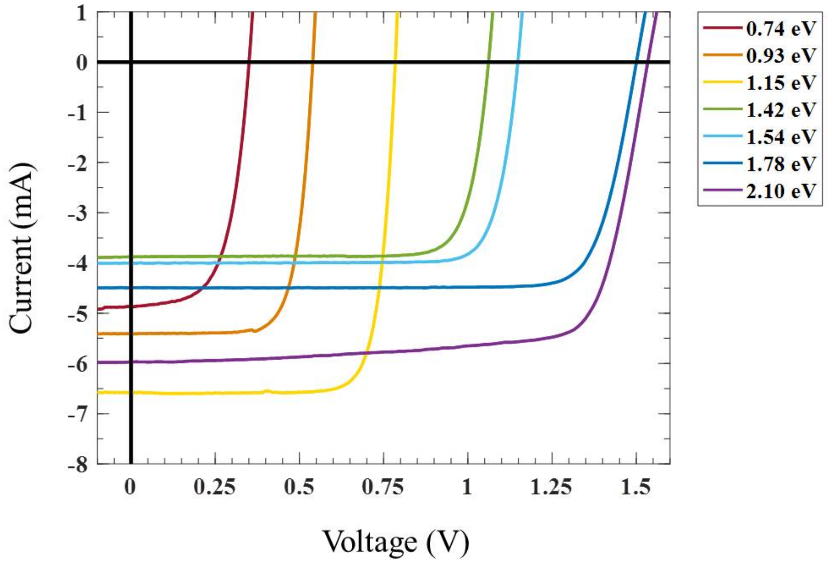

Figure 5.19: The seven current-voltage traces of the photovoltaic cells while the spectrum splitting prototype PSRv3 was illuminated with an AM1.5D spectrum.

obscuration fraction than desirable or fundamentally necessary. The contact grids featured 25 μm wide fingers in an inverted square pattern, as described in chapter 4. The width of the fingers was chosen to be 25 μm due to challenges in performing small feature photolithography on lift-off thin film samples that were not perfectly planar and featured difficult to remove edge beads. The optimized contact grids designed featuring 25 μm wide fingers featured a single finger for the four higher bandgap GaAs based devices, and three fingers for the three lower bandgap InP based devices. This resulted in a grid obscuration of 4.9% for the GaAs based devices and 8.9% for the InP based devices. Electrical simulations performed by Cris Flowers indicated that with finger widths of 5 μm, grids exhibiting only 2.5% shadow loss could be fabricated with the same resistance losses.

Having accounted for losses of light before delivery to the surfaces of the cells, we last consider the absorption of the cells themselves. As described in chapter 3, it was determined that state-of-the-art III-V photovoltaics collected 92% of the light incident on their active area as photocurrent. The remaining 8% includes reflection losses and steady state minority carrier recombination at zero bias. Figure 5.20 depicts transmission efficiency through the optics to the cells overlayed with the EQE of the prototype. From the difference, after accounting for shadowing loss and fresnel reflections, we can calculate the in-band absorption of each of the seven cells relative to the design target of 92%, also depicted in 5.20 It is clear that with the exception of the 1.15 eV cell, they fall short. The 1.78 eV cell is particularly poor, owing to a weak turn-on of absorption at its band edge. Figure 5.21 depicts the EQE of a bare 1.78 eV, under no optics and with a single layer anti-reflection coating. The slow rise in EQE at the band edge is responsible for more than 1 mA/cm^2 of lost photocurrent. It should be noted that the profile of the EQE in figure 5.21 is not exactly what one would expect for a 1.78 eV InGaP cell. The absorption coefficient of InGaP rises slowly between 700 nm and 400 nm, so a thin absorber should have a weak EQE out to shorter wavelengths than pictured. However, this could easily be explained if the emitter were actually a higher bandgap composition, closer to 1.9-2 eV, and thus contributes to current collection in the region between 400-600 nm.

In addition, all of the cells have planar metallic back mirrors deposited on thick (500 nm) heavily doped contact layers. The devices should be designed for dual pass absorption in their lifted off configuration, but the presence of the generally lower bandgap contact layer destroys the potential for second-pass absorption. Improving this back mirror would require selectively removing the contact layer across the

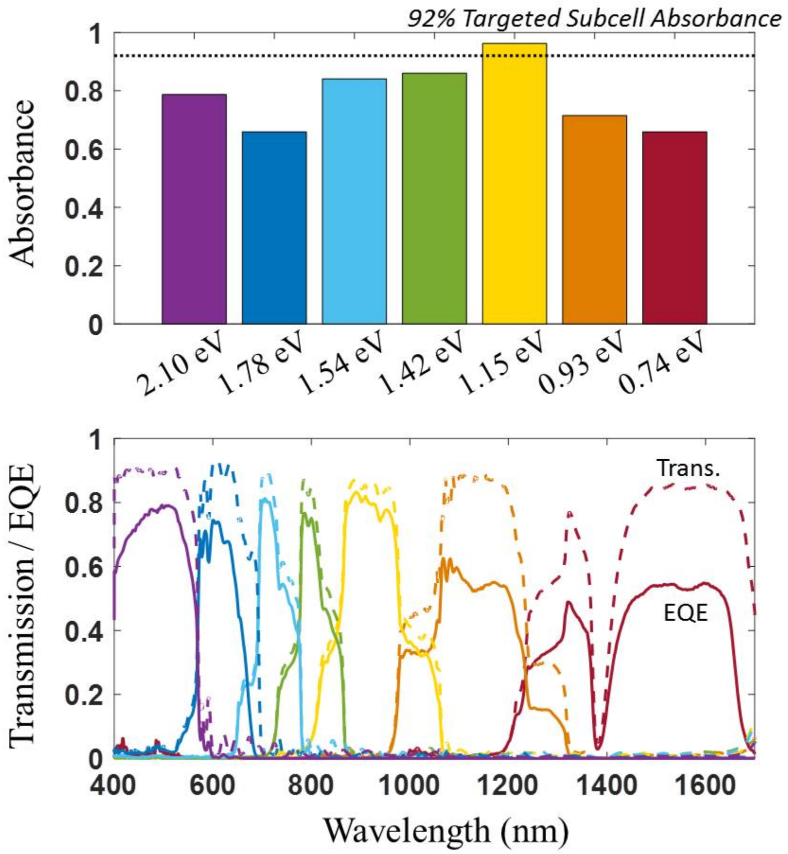

Figure 5.20: Top: In band absorbance of PSRv3 cells marked against the 92% design target. Bottom: The transmission through the optics compared with the prototype external quantum efficiency.

majority of the rear of a cell, leaving only enough area to make electrical contact to, and infilling a dielectric spacer between the metallic mirror and back surface field elsewhere. Furthermore, thinner contact layers, on the order of 50-100 nm, would be desirable. Of note, however, there were two compositions of rear contact layers used in these devices, one for the GaAs based cells and one for the InP based cells. If absorption in the rear contact layer was the primary photocurrent loss mechanism, we would expect to see it exacerbated for the higher bandgap cells of the GaAs and InP sets. In actuality, the highest bandgap InP based cell was the best performing, and similarly the trend in GaAs based cells is weak. Therefore, it is likely that another major source of the lack of photocurrent is sub-optimal thickness of the absorber layer. Optimizing the absorption of the cells by adjusting the thickness of the absorber layer and contact layers would be a key goal of further development of

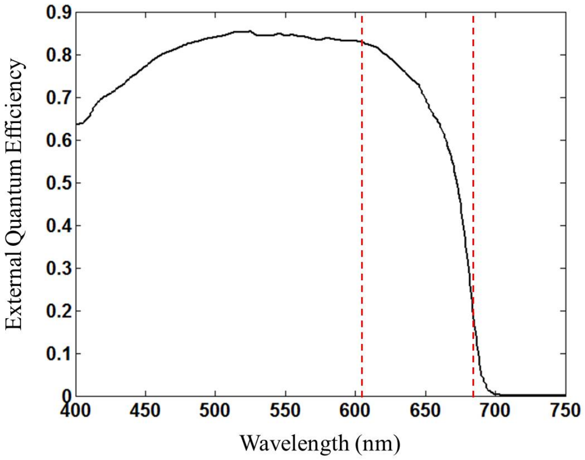

Figure 5.21: External quantum efficiency of a 1.78 eV device similar to the device integrated into PSRv3 showing weak band-edge absorption. The spectral region delivered to it via the splitting optics is indicated with vertical dashed lines.

the photovoltaic cells.

Open-Circuit Voltage and Fill Factor

The open-circuit voltages of the seven photovoltaic cells in PSRv3 shown in table 5.7 exhibit a monotonic increase in with bandgap, demonstrating the benefit of spectrum splitting. However, the open-circuit voltages were not as high as they could be. Following the analysis of perimeter recombination described in section 5.3.2, the cells are not expected to have lost more than 10 mV open circuit voltage from their small size at the optical concentration level in PSRv3. However, there is evidence that damage incurred during the integration of the cells with the optics that generated additional active recombination centers and lowered the device voltages and fill factors. Figure 5.22 shows a set of fourteen current-voltage traces taken of the seven cells incorporated in PSRv3. One trace of each cell was taken immediately after the mesa isolation, while the copper film was still attached to the silicon handle. The second trace of each cell was taken immediately before the attachment to light pipe concentrators. This is after the films were separated from their silicon handles, singulated into single cells, epoxied to a carrier, wire bonded to said carrier, and had an anti-reflection coating deposited. This second set of curves was translated to match the short circuit current of the first, as the anti-reflection coating boosted the current. It is readily apparent that the devices following integration steps have lower

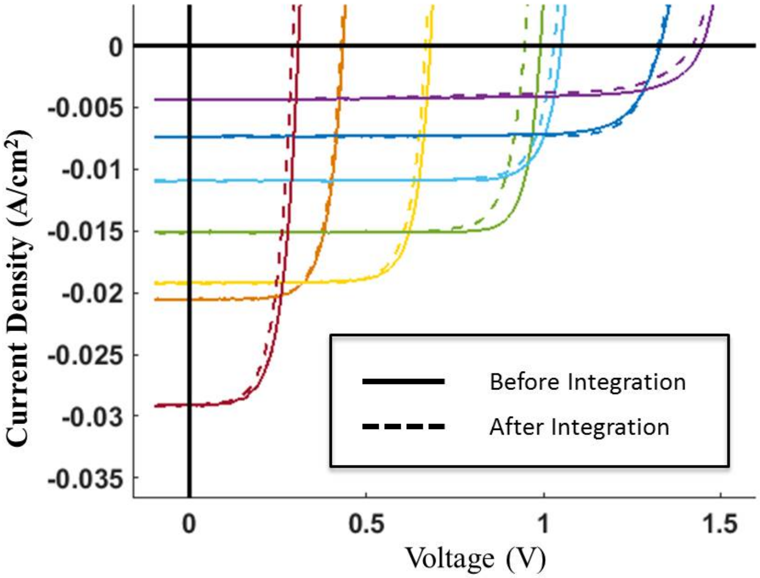

Figure 5.22: Current-voltage traces of photovoltaic cells integrated into prototype PSRv3, as they were processed on-film (solid line) and after integration with optics (dashed line).

open circuit voltages, and the values are listed in table 5.8. Improving the handling of the cells during integration, and minimizing physical damage is important to achieve the efficiency potential of these devices.

Bandgap (eV)	Pre-Integration V_{oc} (mV)	Post-Integration V_{oc} (mV)	Adjusted Post-Integration V_{oc} (mV)
0.74	308	296	291
0.93	434	432	429
1.15	680	673	668
1.42	992	954	946
1.54	1050	1038	1029
1.78	1330	1326	1324
2.10	1448	1437	1420

Table 5.8: Open circuit voltages of cells in PSRv3 before and after integration with the optics.

Another prominent feature of the photovoltaic cell power production curves is that the fill factor of the highest bandgap cell is quite low, and its open-circuit voltafe

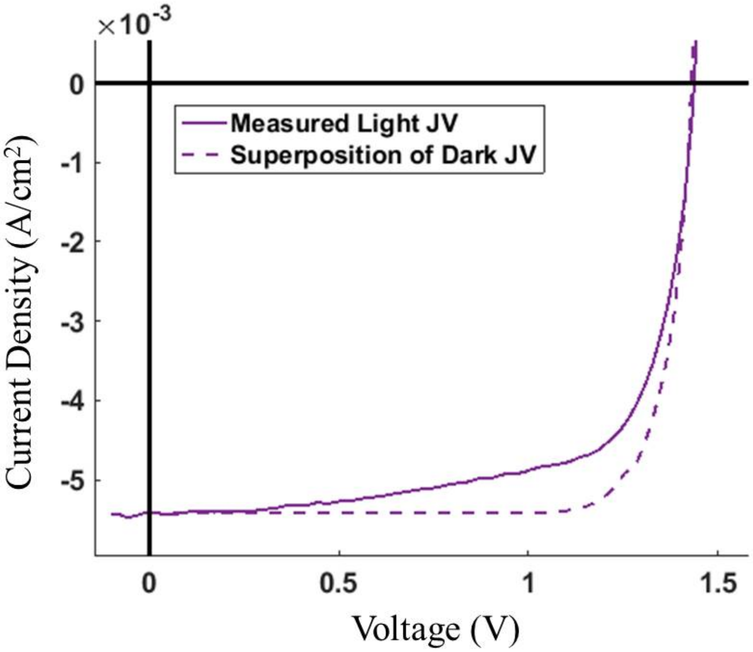

Figure 5.23: Current-voltage trace of the 2.1 eV cell under illumination in PSRv3 (solid line) along with the current-voltage trace of the same cell taken in the dark and translated by the short circuit photocurrent (dashed line) to demonstrate the violation of superposition.

is only slightly higher than that of the 1.78 eV cell. This low fill factor reflects forward bias recombination which is not present in the dark, and thus violates superposition. Figure 5.23 shows a measured current-voltage curve of a 2.1 eV cell under illumination, along with a dark current-voltage curve translated downward by the short-circuit current in the light. The superposition violation is clearly apparent in the knee of the curve, and reduction in fill factor is high enough that even though the open-circuit voltage is higher in the 2.1 eV cell, the max power voltage is lower than in the 1.78 eV cell, meaning that PSRv3 would have had higher efficiency simply by removing the top band entirely.

To understand the superposition violation, consider the EQE and electroluminescence of the 2.1 eV cell, together in figure 5.24. The EQE rises slowly beginning at about 670 nm, and then rises rapidly at about 590 nm from 20% to its peak of 80%. Note that this EQE represents a cell measured in air with an anti-reflection coating designed for incidence under glass, so reflection losses are higher than in the integrated prototype. Furthermore, the electroluminescence peaks at 650 nm. These

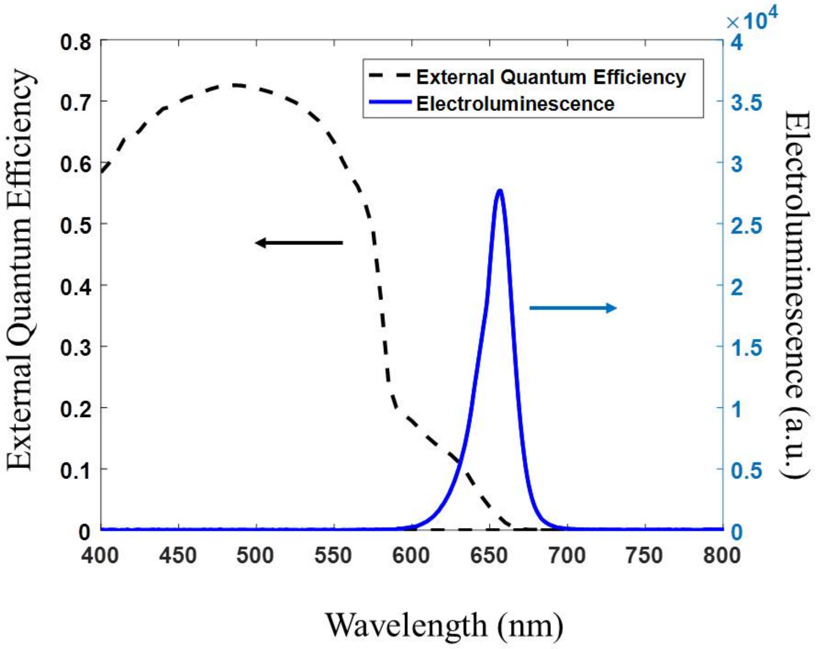

Figure 5.24: The external quantum efficiency (dashed line, left axis) and the electroluminesence spectra (solid line, right axis) of the highest bandgap cell in PSRv3. The band edge of this device is clearly at 650 nm with full absorption rising at 590 nm, indicative of a heterojunction between a 1.9 eV emitter and a 2.1 eV base.

indicated, and Spectrolab confirmed, that this device is in fact a heterojunction cell, with a 1.9 eV emitter and a 2.1 eV base. Although the composition and doping profiles of the device are proprietary to Spectrolab, a working hypothesis has been developed using one-dimensional device models that suggests this is the cause of the poor fill factor.

Consider the three band structures with 1 V applied forward bias depicted in figure 5.25, with parameters summarized in table 5.9. Part a) depicts a 1.9 eV n-type emitter with 5E18 doping level and a 2.1 eV p-type base with 2E16 doping. Level. Part b) is the same heterostructure but with lower emitter doping, only 1E18. Part c) shows the comparable 1.9 eV homojunction device with the same doping as part a), 5E18 in the emitter and 2E16 in the base. In all three parts of figure 5.25 The valence and conduction bands are shown in black, while the quasi-Fermi levels for electrons are shown in red for electrons and blue for holes. The volumetric recombination rate is plotted against the right axis in green. Finally, the quasi-Fermi levels and recombination rates in all three plots are plotted with solid lines for no illumination and dashed lines for 1 sun illumination. Consider first the heterostructure and homostructure diagrams with the same doping levels, plots a) and c) respectively. In plot c) the dominant source of recombination in the dark is in the depletion region where the quasi-Fermi levels are closest to mid-gap, reflecting more equal hole and electron populations that give the highest *np* product. Under illumination, as seen by the dashed lines, there is now a significant amount of steady state recombination in the emitter that was not present in the dark, however, it is on the order of the recombination present in the dark. This results in a small violation of superposition, and a fill factor of 86.8%. In contrast, in plot a) the recombination in the emitter under illumination is several orders of magnitude larger than the recombination in the depletion region in the dark. This gives rise to a significantly larger forward bias recombination current under illumination than in the dark, and the fill factor of the device depicted in plot a) is just 76.0%. Finally, consider the band diagram in plot b) of figure 5.25. It is not obvious due to the logarithmic scale of the recombination rate, but careful examination of the recombination in the emitter under illumination shows that it is nearly an order of magnitude lower than the in the more heavily doped emitter in plot a). Tus, the fill factor of this device has recovered somewhat, and is 83.1%. This additional recombination under steady state is always present in pn-junction solar cells [56], but it is generally negligible. In the case of this heterojunction, however, depending on the doping of the emitter and base this recombination becomes a significant fraction of the total absorbed light.

Diagram	Emitter Bandgap/Doping (eV)/(cm^{-3})	Base Bandgap/Doping (eV)/(cm^{-3})	Fill Factor (%)
Fig. 5.25-a	1.9/5E18	2.1/2E16	76.0
Fig. 5.25-b	1.9/1E18	2.1/2E16	83.1
Fig. 5.25-c	1.9/5E18	1.9/2E16	86.8

Table 5.9: Summary of emitter and base doping levels for simulated devices depicted in 5.25

The effect is exacerbated by heavily doping the emitter, which increases the np-product in the emitter under illumination, since the hole population is dominated by the photogenerated carriers and the electron population is dominated, outside the regime of high injection levels, by the donor doping. Furthermore, this effect can be somewhat ameliorated by more heavily doping the base, which affects the alignment of the valence bands and pushes the emitter valence band slightly lower. The effect is most pronounced then with a heavily doped emitter and lightly doped

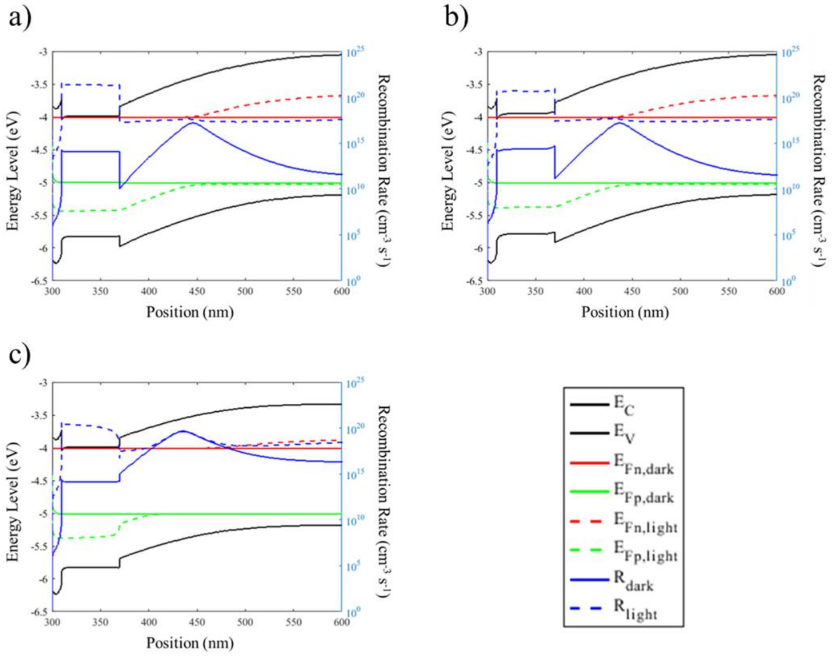

Figure 5.25: Band diagrams of the junction of a device modeled on the 2.1 eV cell under three scenarios, summarized in table 5.9. a) 1.9 eV emitter doped 5E18 and 2.1 eV base doped 2E16. b) 1.9 eV emitter doped 1E18 and 2.1 eV base doped 2E16. 1c) 1.9 eV emitter doped 5E18 and 1.9 eV base doped 2E16. Electron and hole quasi-Fermi levels are depicted in red and green, respectively, and volumetric recombination rates are plotted in blue. Solid lines are in the dark and dashed lines are under 1 sun illumination.

base, and this trend is depicted in table figure 5.26, which also shows that the effect is not observed in either a 1.9 eV or 2.1 eV homojunction device.

Figure 5.27 shows two simulated sets of current-voltage traces for two heterojunction cells with different levels of emitter doping. The first, with a 1.9 eV n-type emitter with 1E17 doping and a 2.1 eV p-type base with 2E16 doping level, and the second with a 1.9 eV n-type emitter with 5E18 cm-3 doping and a 2.1 eV p-type base with 2E16 cm-3 doping. The two current-voltage traces for each device include under illumination and in the dark but translated by the illuminated short circuit current, to demonstrate the extent of superposition violation. The more heavily doped device has a fill factor of the translated dark curve of 87.0%, but just 76.0% in the light. The more lightly doped device has a fill factor in the dark of 93%, which is a slight overestimation due to corrections for high series resistance losses at high current densities in the dark, and a fill factor in the light of 85.2%. It is likely that the

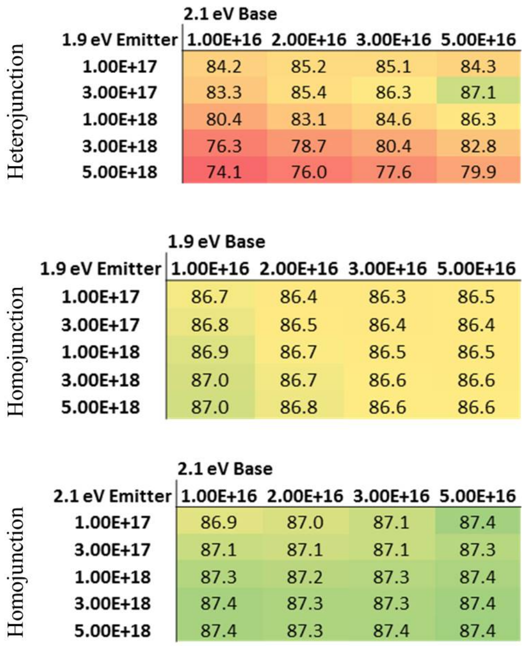

Heterojunction

1.9 eV Emitter	2.1 eV Base 1.00E+16	2.00E+16	3.00E+16	5.00E+16
1.00E+17	84.2	85.2	85.1	84.3
3.00E+17	83.3	85.4	86.3	87.1
1.00E+18	80.4	83.1	84.6	86.3
3.00E+18	76.3	78.7	80.4	82.8
5.00E+18	74.1	76.0	77.6	79.9

Homojunction

1.9 eV Emitter	1.9 eV Base 1.00E+16	2.00E+16	3.00E+16	5.00E+16
1.00E+17	86.7	86.4	86.3	86.5
3.00E+17	86.8	86.5	86.4	86.4
1.00E+18	86.9	86.7	86.5	86.5
3.00E+18	87.0	86.7	86.6	86.6
5.00E+18	87.0	86.8	86.6	86.6

Homojunction

2.1 eV Emitter	2.1 eV Base 1.00E+16	2.00E+16	3.00E+16	5.00E+16
1.00E+17	86.9	87.0	87.1	87.4
3.00E+17	87.1	87.1	87.1	87.3
1.00E+18	87.3	87.2	87.3	87.4
3.00E+18	87.4	87.3	87.3	87.4
5.00E+18	87.4	87.3	87.4	87.4

Figure 5.26: Summary of fill factors for photovoltaic cells under 1 sun illumination with various emitter and base doping levels. Top: A heterojunction cell with a 1.9 eV emitter and 2.1 eV base. Middle: A homojunction cell with a 1.9 eV emitter and 2.1 eV base. Bottom: A homojunction cell with a 2.1 eV emitter and a 2.1 eV base.

modeled device with a more heavily doped emitter features a similar doping profile to the device incorporated into the PSR prototypes.

5.5.2 Pathways to Regain Efficiency

The attainable contactless device efficiency of the optical design for the final prototype was modeled to be 47.5%. This calculated efficiency reflects certain compromises in the from the highest efficiency optical design which exhibited a contactless device efficiency of 52.4%. These compromises in the reduction to practice include lower optical concentration due to removing the top concentrator, replacing the secondary CPCs with straight-walled light pipes, and slightly over-sizing the cells to account for alignment tolerances and busbars. Furthermore, the edges on the prism pieces on which the filters are deposited were beveled for fabrication reasons. Figure 5.28 depicts the optical transmission to each of the seven photovoltaic cells for light incident on the top aperture with an angular width of 1.5 degrees as calculated via ray tracing the optical design.

The contactless device efficiency of 47.5% for the optical design of PSRv3 was

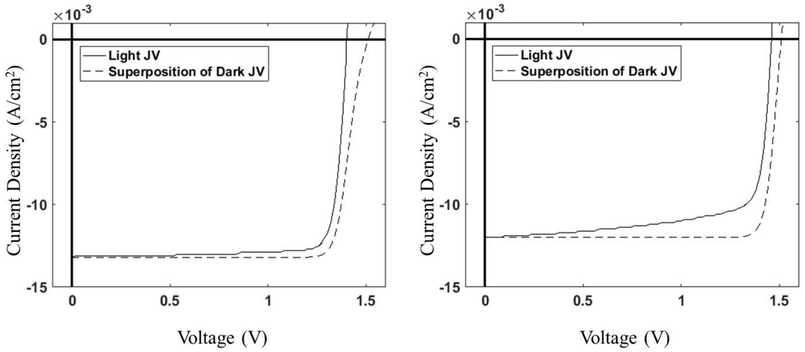

Figure 5.27: Simulated current voltage curves for two heterojunction devices with different emitter doping levels under 1 sun illumination, along with their dark current-voltage trace translated by the short circuit current. Left: 1E17 emitter doping and 2E16 base doping. Right: 5E18 emitter doping and 2E16 base doping.

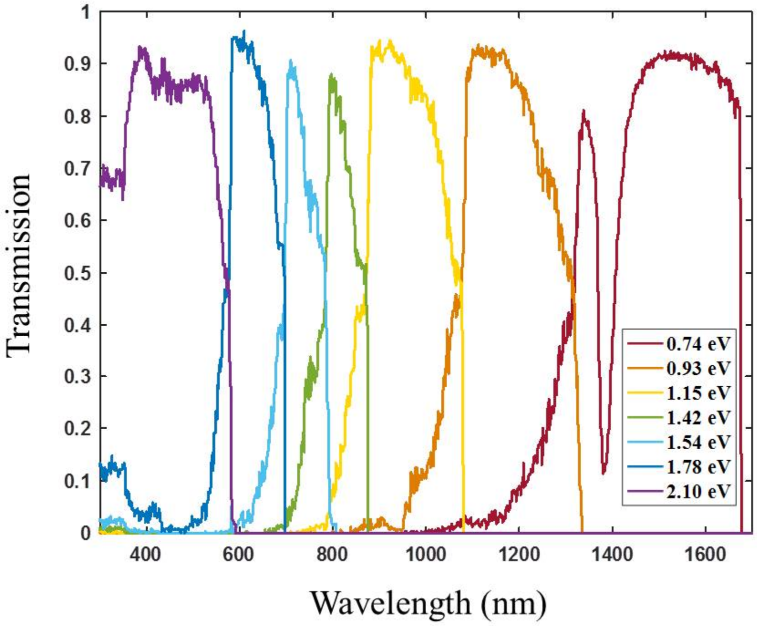

Figure 5.28: Spectral allocation to each of the seven photovoltaic cells as determined by ray tracing the PSRv3 optical design.

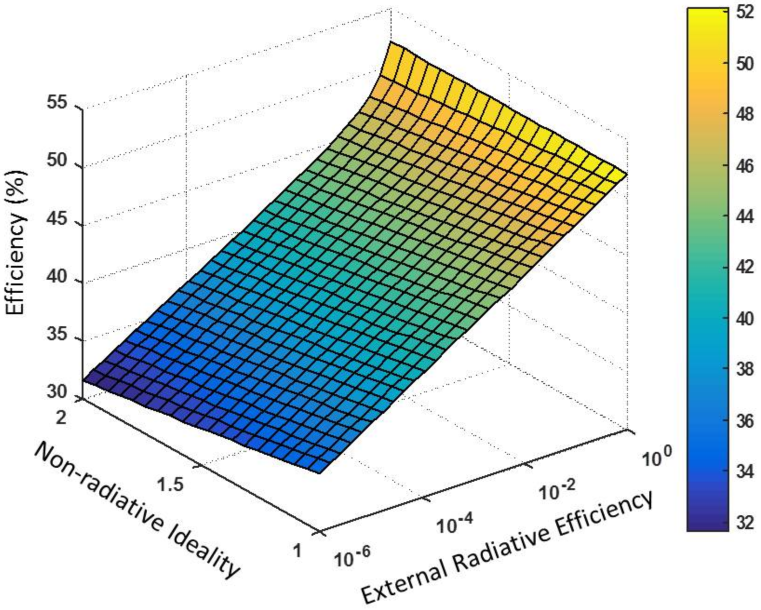

Figure 5.29: The efficiency of the optical design of PSRv3 as a function of the non-radiative ideality and the external radiative efficiency of the ensemble of photovoltaic cells.

calculated via a modified detailed balance model that assumed the seven bandgaps had 92% absorption of light on their active area, and external radiative efficiency as described in table 3.1. Importantly, this also assumed that the non-radiative recombination had an exponential modulation with an ideality of one. As described in chapter 1, this is generally not valid, although if the external radiative efficiency is high enough and the non-radiative ideality is closer to one, the assumption is not bad. Figure 5.29 depicts the modeled contactless device efficiency of the PSRv3 prototype under a range of values for the average ERE and non-radiative ideality of the ensemble of cells. If the cells exhibited ERE values as targeted and had non-radiative idealities of 1.3 rather than 1, the contactless device efficiency would be 46.3%, rather than 47.5%.

In order to understand how to raise the efficiency of PSRv3 from 30.2% to 47.5% then, let us cascade the losses described already. First, the current collection of the cells could be improved by reducing the shadowed fraction to just 2.5% if the minimum feature size could be reduced from 25 μm to 5 μm. Next, co-development of the cells and filters to better match the filter band edges to the absorption edges of the cells, as well as optimizing the cell absorber thicknesses would allow the cells to match the demonstrated possible carrier collection efficiency of 92% in-band. These two enhancements would raise the efficiency of PSRv3 to 37.1%

Next , improvements in the handling, singulation, mounting and wire bonding of devices should allow the external radiative efficiencies to be increased to their on-wafer levels, for those devices which were lacking. Those improvements would also decrease the non-radiative ideality, as evidenced by the increase in idealities observed throughout the integration process. Non-radiative idealities of 1.7 should be attainable by eliminating the observed series resistance in the 1.78 eV cell and improving the superposition violation near the max power point of the top cell. These two improvements would further raise the submodule efficiency to 40.9%.

Further development of the top cell as a 2.1 eV homojunction device with an ERE of 0.1% would significantly improve its fill factor and voltage, and raise the efficiency to 42.5%. Lowering the non-radiative ideality of all cells to 1.3, a reasonable value as evidenced by measurements prior to damage incurred during prototype integration, would increase the efficiency to 43.8%. Finally, through further development of the cells and more optical design of their rear contact layers and back mirrors, their EREs could be raised to the design targets, yielding an efficiency of 45.2%. The difference between this attainable efficiency of 45.2% and the simulated value of 46.3% for the optoelectronic design of PSRv3 reflects the discrepancy between the assembled optics and their more idealized versions in the ray trace. This suggests that adhered dust, chipped edges, and misalignment reduced the total efficiency by only 2.4% relative.

The efficiencies attainable through these identified improvements are summarized in figure 5.30

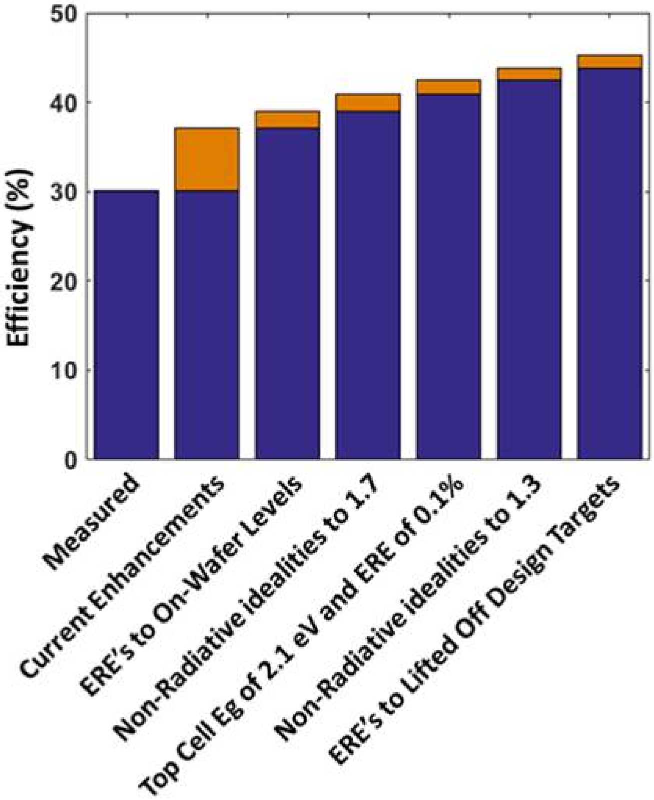

Figure 5.30: Improvements to the efficiency of PSRv3 that are achievable through identified methods.

Chapter 6

OPTICAL DESIGN OF A SCALABLE POLYHEDRAL SPECULAR REFLECTOR

6.1 Lessons From Technoeconomic Analysis of PSR Designs

Significant effort was devoted to understanding the limiting cost at scaled production of the polyhedral specular reflector designs described in earlier chapters of this thesis. Ultimately, there were three primary drivers of the underlying costs. They were the sheer number of components, the material utilization involved in maintaining a solid optical path, and the photovoltaic cells themselves. Any spectrum splitting design which might offer economic advantage over less efficient modules must address these three aspects and do so in a way which is conceivably scalable.

The primary cost driver in the analysis of the family of PSR designs described in chapter 3 was the component count, and the expense of assembling such designs with large numbers of components requiring high shape and alignment tolerances. This family of designs require multilayer dielectric stack filters deposited on quartz pieces, which are then combined to create filters embedded in a solid optical path. Secondary concentrators coupling the cells to the splitting optic offer an additional component per spectral band. For a sub-module with n spectral bands, this creates 3n components per submodule without even considering mechanical and electrical integration requirements.

The second cost driver in the analysis of the PSR was the volume of material required per unit aperture area. Utilizing two stages of concentration was advantageous for the optical design, in that it reduced the angular width of light incident upon the filters while still allowing high optical concentration levels on the photovoltaic cells. However, the downside is that the cell size has a practical lower limit of 100-1000 um on a side, determined by alignment tolerances and perimeter recombination. The area of the splitting optic that couples to each secondary concentrator is then 4 larger than the cell in each dimension. This area is equal to the area of the input face of the splitting optic, since each band is reflected off to the side at 45 degrees. Thus, for a design with a photovoltaic device of edge length L and secondary concentration C_s, the volume of solid material required for the splitting optic alone is $(\sqrt{C} * L)^3$, or an area equivalent thickness of $\sqrt{C_s} * L$. Figure 6.1 demonstrates the equivalent

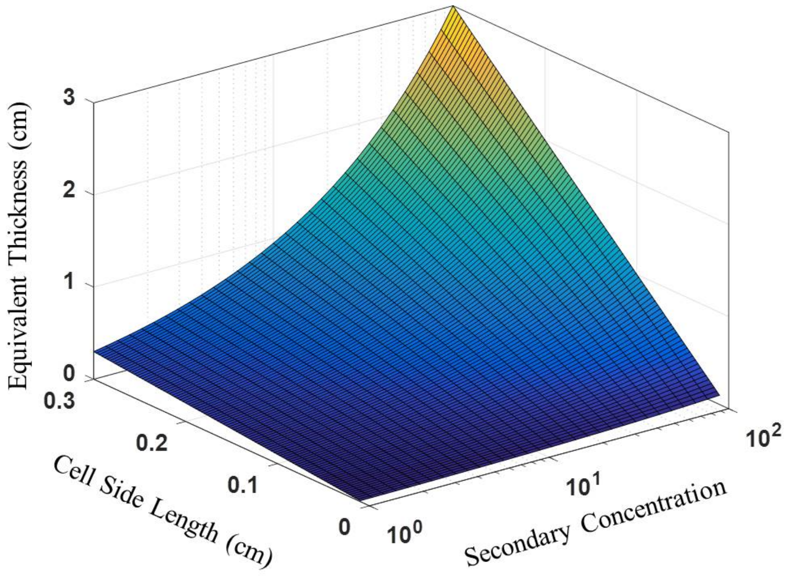

Figure 6.1: Equivalent thickness per unit aperture area per single spitting optic element as a function of cell size and secondary concentration.

thickness per unit aperture area per single spitting optic element as a function of cell size and secondary concentration. Although this areal density is reduced by a factor equal to the primary concentration, it is multiplied by the number of spectral bands. Additionally, the secondary concentrator will require a volume of material roughly equal to or as much as several times that of the splitting optic piece. This scaling relationship imposes a requirement for low secondary concentration even with small cells. It also means that the optical path length through the solid material is quite long, and thus lower cost but more optically absorbing materials such as polymers are unsuitable.

The least significant of these three cost drivers was the photovoltaic devices themselves. Although at present the supply chain for lifted-off single junction photovoltaic devices is not robust, advances in epitaxial lift-off with substrate reuse and high growth rate epitaxial growth make it conceivable that high quality single junction III-V devices operating under concentration levels up to 200x would be a small portion of a module's cost.

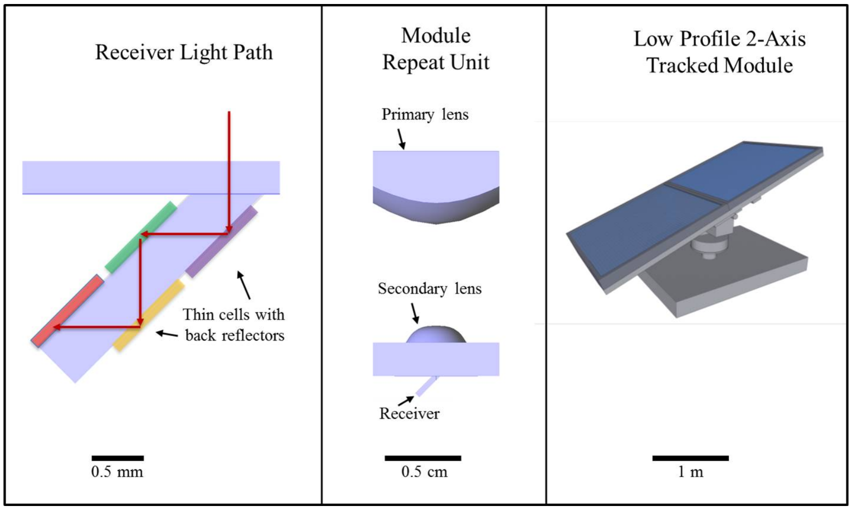

Figure 6.2: Schematic of the kirigami micro-optical design. Left: Specular ray path within the receiver across four cells acting as absorbing filters. Center: Repeat unit of two-aspheric lenses focusing light into the receiver. Right: Envisioned module profile on a 2-axis tracker.

6.2 Kirigami Micro-Optical Design

With the cost drivers from the PSR technoeconomic analysis in mind, a new design was conceived that may offer a pathway to retain high efficiencies afforded by spectrum splitting while significantly reducing costs. This design eliminates a large number of components by using the cells themselves as optical filters, eliminating the dichroic filters and secondary concentrators. The design is depicted at three scales in figure 6.2. First, the receiver is a solid material tilted at some angle near 45 degrees, with cells aligned along two opposing tilted faces. The cells are arranged in order of high to low bandgap, and when light strikes each cell the light above the device bandgap is absorbed while the lower energy light passes through the device, reflects off of a back reflector, and passes back out of the cell towards the next cell. The spectrum splitting is thus performed by each cell as a long-pass absorption filter, which is entirely angle insensitive. This angular insensitivity of the splitting mechanism means that as long as the geometry of the ray path can be designed to hit the cells in the correct order, higher primary concentration can be utilized and further reduce the component count. This does place a requirement for specularity on the back reflector of each device it should be noted. Part a of figure 6.2 depicts this specular ray path through the receiver for a particular ray path.

In order to keep the material utilization low for the optics the size of the receiver input aperture is set to by 500 um by 500 um with cells of side length 500 um by 707 um. Furthermore, a two-stage refractive optic with an air gap, visible in part b of figure 6.1, allows a compact optical design compatible with the small receiver size. This optical design allows for a single injection molded or embossed top sheet with a flat side facing the environment, a standard design feature of nearly all commercial photovoltaic modules. The optical concentration is provided by two aspheric plano-convex lens arrays. The first is on the underside of the top sheet, and the second is just above the receiver. The receiver and second lens can be fabricated on a single sheet of injection molded or embossed acrylic, allowing all of the optics to be fabricated from just two molded parts. Finally, as seen in part c of figure 6.2, these receivers are tiled in a close packed array and mounted on a two-axis tracker to keep direct insolation within the acceptance angle of the optics.

A key enabling feature of this proposed design is one that would allow the careful placement of single-junction microcells on the 3D receiver. A promising pathway to do so involves transfer printing of the microcells onto a single backsheet with integrated electrical traces. Cuts can be made in the back sheet around sets of cells to create tabs which may be folded up around the molded receiver elements. In this way scalable transfer printing manufacturing can be combined with scalable molding technologies, and result cells assembled on a 3D receiver element. Figure 6.3 depicts an exploded view of this assembly process in several stages.

6.3 Module Optical Design and Performance

The use of cells as absorbing long-pass filters works very well for light normally incident on the receiver, but in order to reach moderate to high concentration levels that lower costs by reducing component counts on an area and power basis, light is necessarily incident on the receiver through a range of angles. The first order analysis of this design requires assessing whether the geometric arrangement of cells on the receiver is compatible with good splitting efficiency at higher incident angles.

A ray trace model was built using Synopsis LightTools to assess the splitting efficiency of the receiver element alone. Four single junction photovoltaic cells at bandgaps indicated in table 6.1 were arrayed long the receiver, two on each tilted face. The cells were assumed to absorb 92% of the available light above their bandgaps, and 2% parasitically below their bandgaps. In order to reach this low level of parasitic sub-bandgap absorption careful attention must be paid to the back

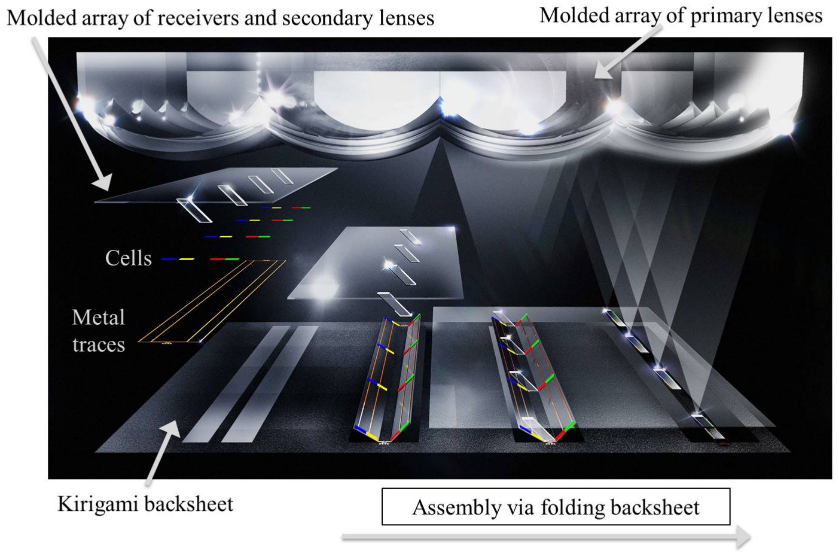

Figure 6.3: Rendering of kirigami micro-optical design and envisioned assembly process. The kirigami folding assembly process positions cells that were transfer printed onto the backsheet to be paired with the array of receivers molded on a single piece of acyrlic aling with secondary lenses (not pictured).

reflector and the various device layers. Cladding and contacting layers must be high enough bandgap or thin enough so as not to parasitically absorb lower spectral bands. The external radiative efficiency was used to parameterize the material quality, as described in chapter 1 and used in chapter 3 of this thesis, and these assumed values are also given in table 6.1. The spacing between adjacent cells is important to be minimized while maintaining electrical isolation. A minimum practical gap of 10 um was assumed, although this parameter needs further study.

Cell Order	Bandgap (eV)	Alloy	External Radiative Efficiency (%)
1	2.1	AlInGaP	0.19
2	1.58	AlGaAs	3.0
3	1.15	InGaAsP	1.2
4	0.74	InGaAs	11

Table 6.1: Proposed bandgaps, alloys, and assumed external radiative efficiency for the proposed four bandgap kirigami micro-optical design.

A broadband light source was directed onto the receiver input face and the flux to each cell recorded as the angle of incidence of the source was varied about two

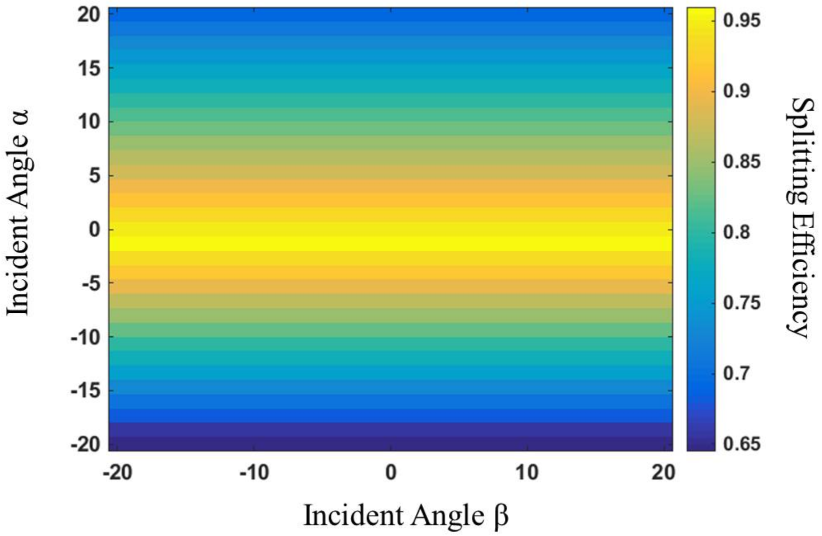

Figure 6.4: Optical splitting efficiency of the receiver element as a function of two angles of incidence on the input aperture. α is the angle about the axis of rotation that the receiver is tilted, and β is the angle about the perpendicular axis of rotation in the plane of the input aperture.

angles of rotation. The first, referred to here as alpha, is rotation about the same axis of rotation as the receiver is tilted. Thus, at -45 degrees in alpha light travels directly down the receiver, and at +45 degrees in alpha light strikes the first cell at normal incidence. Similarly, beta refers to rotation about an axis perpendicular to the tilt axis of the receiver, and light incident at higher angles in beta is totally internally reflected up to the critical angle in acrylic. The figure of merit to assess the receiver is the splitting efficiency, defined as before as the modified detailed balance efficiency of the cell ensemble exposed to the flux resulting from ray tracing, divided by the modified detailed balance efficiency of the cell ensemble with perfect spectral photon allocation.

The asymmetry in the receiver due to the tilt gives rise to an asymmetry in the angular response of the splitting efficiency of the receiver. Figure 6.4 depicts the splitting efficiency as a function of alpha and beta angles of incidence on the receiver input aperture. This asymmetry of the splitting efficiency can be exploited, as the incident angles map back to position on the primary optic. Thus, a rectangular optic can achieve optical concentration with wider angular width in beta than in alpha, which would offer higher splitting efficiency than a square concentrator with the same geometric gain.

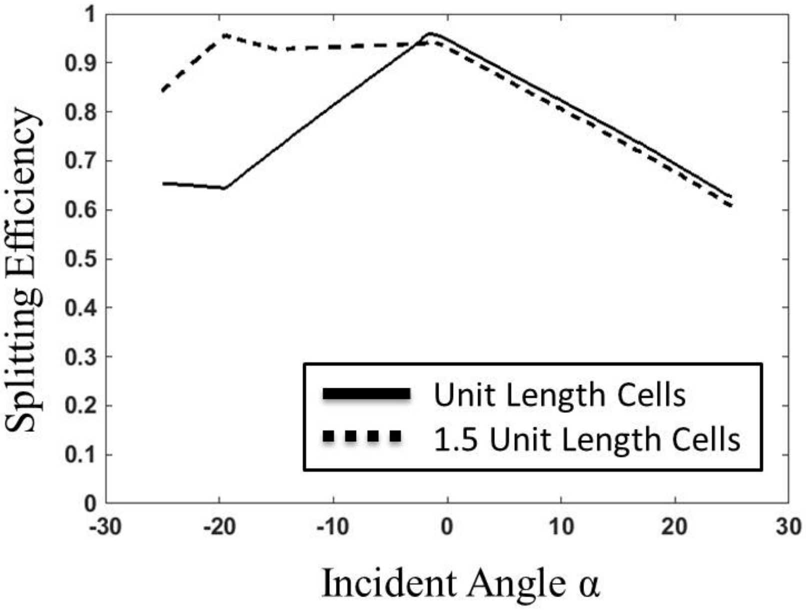

Figure 6.5: Optical splitting efficiency of the receiver as a function of the incident angle on the input aperture for two different cell lengths along the receiver. Unit length is the length equal to the projection of the input aperture on the face of the receiver.

Additionally, as long as the cells have suitably low parasitic sub-bandgap absorption, the cells can be extended in length along the receiver and gain higher splitting efficiency along alpha. This effect is shown in figure 6.5. Cells 500 um by 707 um in dimension are represented by the solid line, and are equal to the width of the receiver input aperture as well as the projection directly downward onto the side of the receiver, which is $\sqrt{2}$ times the width of the input aperture for a 45 degree tilted receiver. The dashed line depicts cells 1.5 times longer along the face of the receiver. These longer cells drive the design conceptually closer to a cavity design, and light coming from more positive angles in alpha suffer slightly more parasitic absorption from additional bounces on higher bandgap cells, but light incident from more negative angles in alpha has more opportunity for striking cells in the proper order. This data shows that an average splitting efficiency of 90% is attainable with an angular width in alpha of +/- 10 degrees, even before extending the cells.

Figure 6.6 shows the thermodynamic limits to two-axis concentration for the system. With an acceptance angle of 1 degree, and for two cases of the angular width of beta after concentration (45 and 60 degrees), the concentration limit is given for

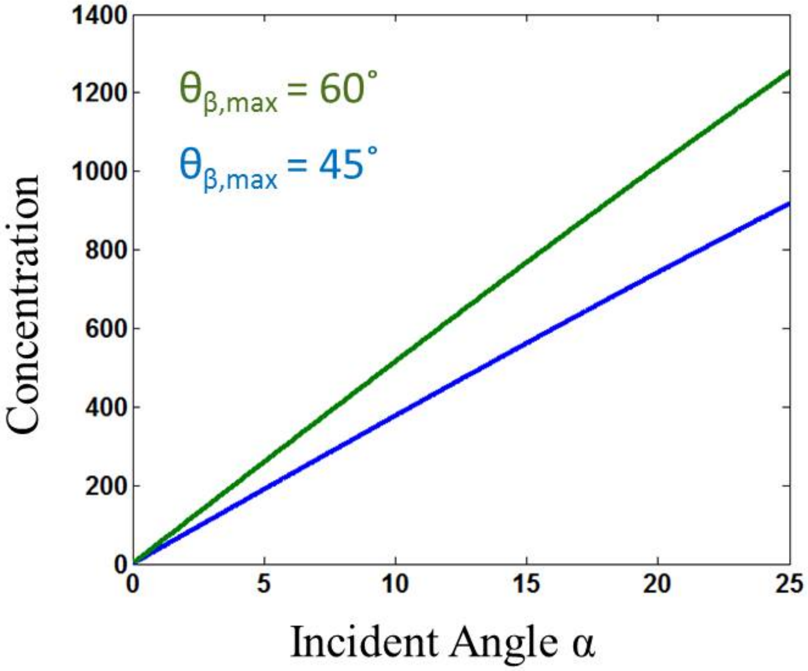

Figure 6.6: The maximum optical concentration on the input aperture of the receiver as a function of the angular width in α for two different angular widths in β.

the half angle in alpha. This encouragingly shows that even with beta restricted to 45 degrees to maintain total internal reflection, the thermodynamic limit to concentration is nearly 400x, and thus even with aberrations in a real optical system high concentrations should be achievable.

The two-stage aspheric plano-convex lenses were designed by first setting the height of the module at 1.5 cm, which represents an angular width of approximately 15 degrees at 225x. Then a gradient ascent algorithm was implemented that searched over a number of parameters. First, the polynomial aspheric coefficients of both plano-convex lenses were optimized for throughput on the receiver face. Next, the receiver was optimized by adjusting the width in both dimensions of the first lens, and the relative vertical spacing between the two lens arrays, subject to the constraint of maximum 1.5 cm module thickness. Finally, the geometric perturbations of the receiver were optimized, including the pitch of the receiver and the aspect ratio of the photovoltaic cells. The resulting repeat unit had dimension of 9.4 mm by 6.0 mm, a geometric concentration of 225.6x relative to the input face of the receiver. The thickness of the top sheet plano-convex lens array was constrained to at least 3

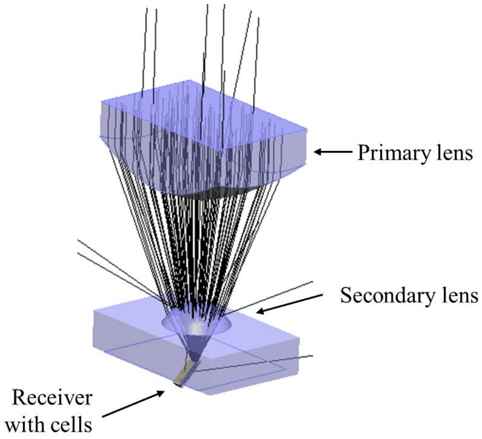

Figure 6.7: Ray trace model of the repeat unit in the kirigami micro-optical design.

mm to satisfy module durability requirements, and the thickness of the second sheet containing the receiver elements and secondary lenses was constrained to 1.5 mm thick at its narrowest point for structural reasons.

The resulting optimized optical design is shown in figure 6.7. The resulting efficiency of this design was 40.3% for the four bandgap cell ensemble described previously. For this design there were three primary optical loss mechanisms. This cell ensemble as derated for detailed balance would have an efficiency of 51.7% at 225x in band optical concentration if every photon was perfectly allocated according to its energy. When the imperfect splitting resulting from the geometric configuration of the cells and angular spread of the concentrator is considered, the efficiency drops to 47.6%. This represents a splitting efficiency of 92%, as expected from the initial examination of the receiver geometry. The next large loss mechanism is the multiple Fresnel reflections. The air gap between the two lens arrays gives a total of three air-acrylic interfaces, which are not easily treated to reduce reflective losses. These losses account for an additional 6% absolute loss in efficiency, reducing the total to 41.6%. Technological improvements in acrylic anti-reflection coatings would be very beneficial to this design. Finally, an additional 1.3% absolute of the power is lost due to parasitic volumetric absorption in the acrylic. This is unavoidable, but kept acceptably low owing to the short optical paths in this compact micro-optical design. Thus, the resulting efficiency of this four-junction spectrum splitting design is 40.3%.

Chapter 7

PERSPECTIVE ON THE PROSPECTS FOR SPECTRUM-SPLITTING PHOTOVOLTAICS

The commercial realities of the solar photovoltaic marketplace have changed quickly and radically over the last several decades. Silicon modules have gained a dominant market share owing to relentless cost-cutting and power conversion efficiency gains. This has reduced the potential market opportunity for alternative technologies, and a long line of competing material systems and optical technologies have failed to thrive in the commodity electricity generation business. Spectrum-splitting solar technologies, including those presented in this work, exhibit a complexity that is difficult to scale. The promise of high efficiency is limited by the technical challenges whose mitigation is equivalent to cost. Furthermore, the semiconductor material systems that would be most advantageous to spectrum-splitting technologies, namely the III-V compound semiconductors, presently lack a supply chain and cost structure that would enable a new spectrum-splitting technology to quickly reach scale. Finally, physical mechanisms that exhibit sharp and controllable cutoffs in both angle and wavelength space are necessary to fully exploit the promise of spectrum-splitting photovoltaics.

An environment wherein some spectrum-splitting technology might gain a cost advantage would likely require further advances on several fronts. Firstly, an increase in the availability of high-quality III-V photovoltaic material would support spectrum-splitting technologies. The decline of the concentrating photovoltaic industry has reduced prospects for the supply of such materials, as the space-based photovoltaic market supports a much smaller volume at a much higher cost than terrestrial photovoltaics. Research into improving growth rates and epitaxial quality, as well as reducing precursor costs and the capital expense of growth systems is an important towards reaching these goals. Incremental improvements in III-V MOCVD growth methods is unlikely to reach these goals in the short term, though advancements in alternative growth methods such as hydride vapor phase epitaxy may.

A second enabling condition would be the maturation of nano- and micro-scale fabrication techniques. There are tremendous advantages in concentrating photovoltaics to reducing the physical scale of systems. Fabrication techniques that allow for very high component counts at low cost would be beneficial, including for example high-throughput transfer printing approaches. Spectrum-splitting optics must efficiently utilize material and volume and small system scales enable that. Additionally, wave-optical spectrum-splitting optics would need to be fabricated at low areal cost. Fabrication of micro-optical systems via scale-able methods such as nanoimprint lithography could be exploited to fabricate more affordably than multilayer deposition methods.

Finally, future research into engineered optical properties and metamaterials is necessary to develop physical mechanisms that will sharply split the spectrum and can be fabricated with the required fidelity over large areas at low cost. Higher dimensional (2D, 2.5D, 3D) photonic crystals exhibit some promise as angle-independent spectrum-splitting structures, but the fabrication of such structures without scattering and with high throughput over large areas remains a challenge. Further development of these structures may enable spectrum-splitting module designs that capture some significant portion of diffuse light in addition to direct light, a weakness common to many current proposed spectrum-splitting designs.

The commercial prospects for spectrum-splitting solar are accordingly faint at this point. Future advances in the areas described above will likely be necessary to enable fundamentally low-cost spectrum-splitting photovoltaic designs, and even then the technical risk of new materials and technologies will be a daunting barrier to challenging the dominant silicon photovoltaic incumbent. However, the laws of physics are not affected by manufacturing volume, and as incumbent technologies approach their theoretical potential they will stagnate unless they adapt new strategies, including potentially optical spectrum-splitting techniques.

BIBLIOGRAPHY

[1] IPCC. *Climate Change 2014: Synthesis Report*. Tech. rep. IPCC, 2014.

[2] Chris Martin. *Solar Panels Now So Cheap Manufacturers Probably Selling at Loss*. Jan. 2017. URL: `https://www.bloomberg.com/news/articles/2016-12-30/solar-panels-now-so-cheap-manufacturers-probably-selling-at-loss`.

[3] Sam Pothecary. "PVMA figures show 75 GW of solar PV was installed in 2016". *PV Magazine* (Jan. 2017). URL: `https://www.pv-magazine.com/2017/01/19/pvma-figures-show-75-gw-of-solar-pv-was-installed-in-2016/`.

[4] M. A. Green. "The path to 25% silicon solar cell efficiency: History of silicon cell evolution". *Progress in Photovoltaics: Research and Applications* 17 (2009).
, pp. 183–189.

[5] Simon M. Sze and Kwok K. Ng. *Physics of Semiconductor Devices, 3rd Edition*. 3rd. Wiley-Interscience, 2007.

[6] Peter Würfel and Uli Würfel. *Physics of solar cells : from basic principles to advanced concepts*. 2nd. Wiley-VCH, 2009.

[7] Jenny Nelson. *The Physics of Solar Cells*. Imperial College Press, 2003.

[8] P. T. Landsberg and G. Tonge. "Thermodynamic energy conversion efficiencies". *Journal of Applied Physics* 51.7 (1980), R1–R20. DOI: `10.1063/1.328187`.

[9] William Shockley and Hans J. Queisser. "Detailed Balance Limit of Efficiency of p-n Junction Solar Cells". *Journal of Applied Physics* 32.3 (1961), pp. 510–519. DOI: `10.1063/1.1736034`.

[10] Martin A. Green. "Radiative efficiency of state-of-the-art photovoltaic cells". *Progress in Photovoltaics: Research and Applications* 20.4 (2012), pp. 472–476. ISSN: 1099-159X. DOI: `10.1002/pip.1147`. URL: `http://dx.doi.org/10.1002/pip.1147`.

[11] Gordon Lasher and Frank Stern. "Spontaneous and Stimulated Recombination Radiation in Semiconductors". *Phys. Rev.* 133 (2A Jan. 1964), A553–A563. DOI: `10.1103/PhysRev.133.A553`. URL: `https://link.aps.org/doi/10.1103/PhysRev.133.A553`.

[12] P Wurfel. "The chemical potential of radiation". *Journal of Physics C: Solid State Physics* 15.18 (1982), p. 3967. URL: `http://stacks.iop.org/0022-3719/15/i=18/a=012`.

[13] B Feuerbacher and P Wurfel. “Verification of a generalised Planck law by investigation of the emission from GaAs luminescent diodes”. *Journal of Physics: Condensed Matter* 2.16 (1990), p. 3803. URL: `http://stacks.iop.org/0953-8984/2/i=16/a=010`.

[14] Albert Polman and Harry A. Atwater. “Photonic design principles for ultrahigh-efficiency photovoltaics”. *Nat Mater* 11.3 (Mar. 2012), pp. 174–177. ISSN: 1476-1122. DOI: `10.1038/nmat3263`. URL: `http://dx.doi.org/10.1038/nmat3263`.

[15] Ghassan Zubi, Jose L. Bernal-Agustin, and Gian Vincenzo Fracastoro. “High concentration photovoltaic systems applying III-V cells”. 13.9 (2009), pp. 2645–2652.

[16] Martin A. Green, Keith Emery, Yoshihiro Hishikawa, Wilhelm Warta, and Ewan D. Dunlop. “Solar cell efficiency tables (version 48)”. *Progress in Photovoltaics: Research and Applications* 24.7 (2016), pp. 905–913. ISSN: 1099-159X. DOI: `10.1002/pip.2788`. URL: `http://dx.doi.org/10.1002/pip.2788`.

[17] Emily C. Warmann and Harry A. Atwater. “Energy production advantage of independent subcell connection for multijunction photovoltaics”. *Energy Science & Engineering* 4.4 (2016), pp. 235–244. ISSN: 2050-0505. DOI: `10.1002/ese3.125`. URL: `http://dx.doi.org/10.1002/ese3.125`.

[18] A.G. Imenes and D.R. Mills. “Spectral beam splitting technology for increased conversion efficiency in solar concentrating systems: a review”. *Solar Energy Materials and Solar Cells* 84.1–4 (2004). International Solar Energy Society World Congress 2003, pp. 19–69. ISSN: 0927-0248. DOI: `http://doi.org/10.1016/j.solmat.2004.01.038`. URL: `http://www.sciencedirect.com/science/article/pii/S0927024804001394`.

[19] D.R. Mills and J.E. Giutronich. “Ideal prism solar concentrators”. *Solar Energy* 21.5 (1978), pp. 423–430. ISSN: 0038-092X. DOI: `http://dx.doi.org/10.1016/0038-092X(78)90175-5`. URL: `http://www.sciencedirect.com/science/article/pii/0038092X78901755`.

[20] Carlo Maragliano, Matteo Chiesa, and Marco Stefancich. “Point-focus spectral splitting solar concentrator for multiple cells concentrating photovoltaic system”. *Journal of Optics* 17.10 (2015), p. 105901. URL: `http://stacks.iop.org/2040-8986/17/i=10/a=105901`.

[21] Shelby Vorndran, Juan M. Russo, Yuechen Wu, and Raymond K. Kostuk. “Holographic Lens Hybrid Spectrum-Splitting System: Design and Performance”. *Renewable Energy and the Environment*. Optical Society of America, 2013, RW1D.3. DOI: `10.1364/OSE.2013.RW1D.3`. URL: `http://www.osapublishing.org/abstract.cfm?URI=OSE-2013-RW1D.3`.

[22] Deming Zhang, Michael Gordon, Juan M. Russo, Shelby Vorndran, and Raymond K. Kostuk. “Spectrum-splitting photovoltaic system using transmission holographic lenses”. *Journal of Photonics for Energy* 3.1 (2013), pp. 034597–034597. DOI: `10.1117/1.JPE.3.034597`. URL: `http://dx.doi.org/10.1117/1.JPE.3.034597`.

[23] Ganghun Kim, Jose A. Dominguez-Caballero, Howard Lee, Daniel J. Friedman, and Rajesh Menon. “Increased Photovoltaic Power Output via Diffractive Spectrum Separation”. *Phys. Rev. Lett.* 110 (12 Mar. 2013), p. 123901. DOI: `10.1103/PhysRevLett.110.123901`. URL: `https://link.aps.org/doi/10.1103/PhysRevLett.110.123901`.

[24] A. Barnett, C. Honsberg, D. Kirkpatrick, S. Kurtz, D. Moore, D. Salzman, R. Schwartz, J. Gray, S. Bowden, K. Goossen, M. Haney, D. Aiken, M. Wanlass, and K. Emery. “50% Efficient Solar Cell Architectures and Designs”. *2006 IEEE 4th World Conference on Photovoltaic Energy Conference*. Vol. 2. May 2006, pp. 2560–2564. DOI: `10.1109/WCPEC.2006.279768`.

[25] Juan Manuel Russo, Shelby Vorndran, Yuechen Wu, and Raymond K. Kostuk. “Cross-correlation analysis of dispersive spectrum splitting techniques for photovoltaic systems”. *Journal of Photonics for Energy* 5.1 (2015), p. 054599. DOI: `10.1117/1.JPE.5.054599`. URL: `http://dx.doi.org/10.1117/1.JPE.5.054599`.

[26] U. Ortabasi, A. Lewandowski, R. McConnell, D. J. Aiken, P. L. Sharps, and B. G. Bovard. “Dish/photovoltaic cavity converter (PVCC) system for ultimate solar-to-electricty conversion efficiency-general concept and first performance predictions”. *Conference Record of the Twenty-Ninth IEEE Photovoltaic Specialists Conference, 2002.* May 2002, pp. 1616–1620. DOI: `10.1109/PVSC.2002.1190925`.

[27] A. Goetzberger, J.C. Goldschmidt, M. Peters, and P. Löper. “Light trapping, a new approach to spectrum splitting”. *Solar Energy Materials and Solar Cells* 92.12 (2008), pp. 1570–1578. ISSN: 0927-0248. DOI: `http://doi.org/10.1016/j.solmat.2008.07.007`. URL: `http://www.sciencedirect.com/science/article/pii/S0927024808002274`.

[28] E Yablonovich and G.D. Cody. “Intensity Enhancement in Textured Optical Sheets for Solar Cells”. *IEEE Transactions on Electron Devices* ED-29 (1982), pp. 300–305.

[29] S.K. Tripathy. “Refractive indices of semiconductors from energy gaps”. *Optical Materials* 46 (2015), pp. 240–246. ISSN: 0925-3467. DOI: `http://doi.org/10.1016/j.optmat.2015.04.026`. URL: `http://www.sciencedirect.com/science/article/pii/S0925346715002542`.

[30] Martin A. Green. “Lambertian light trapping in textured solar cells and light-emitting diodes: analytical solutions”. *Progress in Photovoltaics: Research*

and Applications 10.4 (2002), pp. 235–241. ISSN: 1099-159X. DOI: `10.1002/pip.404`. URL: `http://dx.doi.org/10.1002/pip.404`.

[31] Carissa N Eisler, Emily D Kosten, Emily C Warmann, and Harry A Atwater. “Spectrum splitting photovoltaics: Polyhedral specular reflector design for ultra-high efficiency modules”. *Photovoltaic Specialists Conference (PVSC), 2013 IEEE 39th*. IEEE. 2013, pp. 1848–1851.

[32] W. T. Welford and R. Winston. *High Collection Nonimaging Optics*. Academic Press, 1989. DOI: `http://doi.org/10.1016/B978-0-12-742885-7.50001-2`.

[33] Emily C. Warmann, Cristofer Flowers, John Lloyd, Carissa N. Eisler, Matthew D. Escarra, and Harry A. Atwater. “Design of photovoltaics for modules with 50% efficiency”. *Energy Science & Engineering* (2017). ISSN: 2050-0505. DOI: `10.1002/ese3.155`. URL: `http://dx.doi.org/10.1002/ese3.155`.

[34] I. Vurgaftman, J. R. Meyer, and L. R. Ram-Mohan. “Band parameters for III–V compound semiconductors and their alloys”. *Journal of Applied Physics* 89.11 (2001), pp. 5815–5875. DOI: `10.1063/1.1368156`.

[35] R. Varache, C. Leendertz, M.E. Gueunier-Farret, J. Haschke, D. Muñoz, and L. Korte. “Investigation of selective junctions using a newly developed tunnel current model for solar cell applications”. *Solar Energy Materials and Solar Cells* 141 (2015), pp. 14–23. ISSN: 0927-0248. DOI: `http://doi.org/10.1016/j.solmat.2015.05.014`. URL: `http://www.sciencedirect.com/science/article/pii/S0927024815002196`.

[36] A. Boca, K. M. Edmondson, and R. R. King. “Prismatic covers for boosting the efficiency of high-concentration PV systems”. *2009 34th IEEE Photovoltaic Specialists Conference (PVSC)*. June 2009, pp. 000131–000136. DOI: `10.1109/PVSC.2009.5411714`.

[37] Rebecca Saive, Aleca M. Borsuk, Hal S. Emmer, Colton R. Bukowsky, John V. Lloyd, Sisir Yalamanchili, and Harry A. Atwater. “Effectively Transparent Front Contacts for Optoelectronic Devices”. *Advanced Optical Materials* 4.10 (2016), pp. 1470–1474. ISSN: 2195-1071. DOI: `10.1002/adom.201600252`. URL: `http://dx.doi.org/10.1002/adom.201600252`.

[38] Cristofer A. Flowersr. “Full Spectrum Ultrahigh Efficiency Photovoltaics: System Design, Integration, and Characterization”. PhD thesis. California Institute of Technology, 2017.

[39] Ralf Leutz and Akio Suzuki. *Nonimaging Fresnel Lenses*. Springer-Verlag Berlin Heidelberg, 2001. DOI: `10.1007/978-3-540-45290-4`.

[40] Carissa N. Eisler. “Photonic and Device Design Principles for Ultrahigh-Efficiency (>50%), Spectrum-Splitting Photovoltaics”. PhD thesis. California Institute of Technology, 2016.

[41] O. D. Miller, E. Yablonovitch, and S. R. Kurtz. “Strong Internal and External Luminescence as Solar Cells Approach the Shockley-Queisser Limit”. *IEEE Journal of Photovoltaics* 2.3 (July 2012), pp. 303–311. ISSN: 2156-3381. DOI: `10.1109/JPHOTOV.2012.2198434`.

[42] M. C. Tseng, R. H. Horng, Y. L. Tsai, D. S. Wuu, and H. H. Yu. “Fabrication and Characterization of GaAs Solar Cells on Copper Substrates”. *IEEE Electron Device Letters* 30.9 (Sept. 2009), pp. 940–942. ISSN: 0741-3106. DOI: `10.1109/LED.2009.2026292`.

[43] Eli Yablonovitch, T. Gmitter, J. P. Harbison, and R. Bhat. “Extreme selectivity in the lift-off of epitaxial GaAs films”. *Applied Physics Letters* 51.26 (1987), pp. 2222–2224. DOI: `10.1063/1.98946`.

[44] P Demeester, I Pollentier, P De Dobbelaere, C Brys, and P Van Daele. “Epitaxial lift-off and its applications”. *Semiconductor Science and Technology* 8.6 (1993), p. 1124. URL: `http://stacks.iop.org/0268-1242/8/i=6/a=021`.

[45] J.W. Matthews and A.E. Blakeslee. “Defects in epitaxial multilayers”. *Journal of Crystal Growth* 27 (1974), pp. 118–125. ISSN: 0022-0248. DOI: `http://dx.doi.org/10.1016/S0022-0248(74)80055-2`. URL: `http://www.sciencedirect.com/science/article/pii/S0022024874800552`.

[46] P. Kumar, S. Kanakaraju, and D.L. DeVoe. “Sacrificial etching of AlxGa1-xAs for III–V MEMS surface micromachining”. *Applied Physics A* 88.4 (2007), pp. 711–714. ISSN: 1432-0630. DOI: `10.1007/s00339-007-4032-7`. URL: `http://dx.doi.org/10.1007/s00339-007-4032-7`.

[47] A. G. Baca, F. Ren, J. C. Zolper, R. D. Briggs, and S. J. Pearton. “A survey of ohmic contacts to III-V compound semiconductors”. *Thin SOlid FIlms* (1997), pp. 599–606.

[48] E. D. Marshall, W. X. Chen, C. S. Wu, S. S. Lau, and T. F. Kuech. “Non-alloyed ohmic contact to n-GaAs by solid phase epitaxy”. *Applied Physics Letters* 47.3 (1985), pp. 298–300. DOI: `10.1063/1.96198`. URL: `http://dx.doi.org/10.1063/1.96198`.

[49] L. C. Wang, P. H. Hao, J. Y. Cheng, F. Deng, and S. S. Lau. “Ohmic contact formation mechanism of the n-GaAs system formed below 200 C”. *Journal of Applied Physics* 79.8 (1996), pp. 4216–4220. DOI: `10.1063/1.361789`. URL: `http://aip.scitation.org/doi/abs/10.1063/1.361789`.

[50] L. C. Wang, P. H. Hao, and B. J. Wu. “Low-temperature-processed Pd-based Ohmic contacts to n-GaAs”. *Applied Physics Letters* 67.4 (1995), pp. 509–511. DOI: `10.1063/1.114552`. URL: `http://dx.doi.org/10.1063/1.114552`.

[51] Wang Shanling and Pirouz Pirouz. “Mechanical properties of undoped GaAs Part I: Yield stress measurements”. 55.16 (2007), pp. 5500–5514.

[52] G.K. Reeves. “Specific contact resistance using a circular transmission line model”. *Solid-State Electronics* 23.5 (1980), pp. 487–490. ISSN: 0038-1101. DOI: `http://dx.doi.org/10.1016/0038-1101(80)90086-6`. URL: `http://www.sciencedirect.com/science/article/pii/0038110180900866`.

[53] J. H. Klootwijk and C. E. Timmering. “Merits and limitations of circular TLM structures for contact resistance determination for novel III-V HBTs”. *Proceedings of the 2004 International Conference on Microelectronic Test Structures (IEEE Cat. No.04CH37516)*. Mar. 2004, pp. 247–252. DOI: `10.1109/ICMTS.2004.1309489`.

[54] Brian Tuck. “The chemical polishing of semiconductors”. *Journal of Materials Science* 10.2 (1975), pp. 321–339. ISSN: 1573-4803. DOI: `10.1007/BF00540357`. URL: `http://dx.doi.org/10.1007/BF00540357`.

[55] Stéphane Larouche and Ludvik Martinu. “OpenFilters: open-source software for the design, optimization, and synthesis of optical filters”. *Appl. Opt.* 47.13 (May 2008), pp. C219–C230. DOI: `10.1364/AO.47.00C219`. URL: `http://ao.osa.org/abstract.cfm?URI=ao-47-13-C219`.

[56] N. G. Tarr and D. L. Pulfrey. “The superposition principle for homojunction solar cells”. *IEEE Transactions on Electron Devices* 27.4 (Apr. 1980), pp. 771–776. ISSN: 0018-9383. DOI: `10.1109/T-ED.1980.19935`.

Appendix A

MODIFIED DETAILED BALANCE MATLAB CODE

```
%Calculates the IV response of a photovoltaic device via a double diode modified detailed balance model. Inputs are bandgap[Eg (eV)], short circuit current [Jsc (A/cm2)], ERE, non-radiative ideality [n2], and concentration [C].
%=================================
Eg = 1.9; % eV
 Jsc = 0.010; %A/cm2
ERE = 2.0e-3;
n2 = 2;
C=1;

 Jsc = Jsc * C;

 hbar=1.05457148e-34; %m2kg/s
c=299792458; %m/s
k=1.3806503e-23; % m2kg/s2K
T=300; %K
q=1.60217646e-19; %C
kT=k*T/q;
% Etendu accounts for optical environment of cell via top and bottom index values and geometric factor.
 nitop1=1;
 nibottom1=0;
 etendue1=pi*nitop1^2+pi*nibottom1^2;

 power = zeros(length(Eg),1);
 speceff = zeros(length(Eg),1);

max_eV = 4.4;
```

```
number = 2000;  % No difference in 4 places with 1000 vs 10000

specindex = zeros(length(Eg),2);
Gen = zeros(length(Eg),1);

% Calculate radiative emmision from cell at range of operating voltages.

Va=zeros(number,length(Eg));
x=zeros(number,length(Eg));
N=zeros(number,length(Eg));
J0=N;
Jtot=N;
Pn=N;


    Va=linspace(0,(max_eV-0.0001),number)';                    % Applied Bias
    x=logspace(log10(max_eV),log10(max_eV+10),number)';

    for i=1:length(Va)
        N(i)=trapz(x,x.^2./(exp(x/kT)-1)-x.^2./(exp((x-Va(i))/kT)-1));
    end

        Nrad=(q^3*N.*etendue1.*q./(4*pi^3*hbar^3*c^2*100^2)); %A/cm^2

    % Calculate the total dark current if ERE is constant, then use it to find Voc because that ERE is only true at Voc
    J0t = Nrad./ERE;
    Jt = J0t+Jsc;
    zer_oc = find(Jt<=0,1,'first');
```

```
    V_oc = interp1(Jt(zer_oc-10:zer_oc+10),v(zer_oc-10:zer_oc+10),0);
    v_oc_simple = v(zer_oc);
    J0t_oc = J0t(zer_oc);   %The total dark current at open circuit voltage

    % Find the n=1 and n=2 contributions to the total dark current at Voc to extract the J01 and J02 prefactors
    J01_oc = J0t_oc * ERE;
    J02_oc = J0t_oc - J01_oc;

    J01 = J01_oc / exp(V_oc/kT);
    J02 = J02_oc / exp(V_oc/(n2*kT));

    % Now we can calculate entire double diode current.
    J01t = J01*exp(Va/kT);
    J02t = J02*exp(Va/(n2*kT));
    J0tot = J01t+J02t;
    Jtot=Jsc+J0tot;
    Pn = Jtot.*Va;

     maxpn = max(Pn);
     cell_power = maxpn';
     FF = maxpn'./(V_oc.*abs(Jsc));
     mpInd = find(Pn == max(Pn),1,'first');
     v_mp = v(mpInd);
     ERE_mp = J01t(mpInd)/J0tot(mpInd);
```

Appendix B

NONIMAGING FRESNEL LENS DESIGN CODE

```
%Code that designs a the profile of a nonimaging Fresnel lens and
%(optional) imports as a component into Synopsis LightTools

%=================================================
% Define a function to calculate the required tilt of a facet for a given angle of incidence theta1 from medium n1 and exit at angle theta2 into medium n2
function [thetaS, Error] = SlopeSolve(theta1, n1, theta2, n2)
    SlopeD = 0:0.001:40;
    Slope = SlopeD*pi/180;
    for i=1:length(Slope)
        theta1_SCS(i) = theta1 - Slope(i);
        theta2_SCS(i) = asin((n1/n2)*sin(theta1_SCS(i)));
        theta2_find(i)= theta2_SCS(i)+Slope(i);
        Dif(i) = abs(theta2 - theta2_find(i));
    end
    [Error, Index] = min(Dif);
    thetaS = Slope(Index);
end


%==================================================
n1 = 1.5; % Index in the lens
n2 = 1;   % Index below the lens
IncidentAngle = 1 * (pi/180);
L = 200;    % Focal length Units in mm
Wf = 10;    % width of focal plane Units in mm
```

```

% Angles are positive counter-clockwise.
% Let theta2_N be for the exit of negative edge rays (ie to find the slope) and theta2_P for the exit of positive edge rays (to find the width).

theta1 = asin((n2/n1)*sin(IncidentAngle)); % Angle in glass incident on exit facet
theta2_P(1) = asin((n1/n2)*sin(theta1));
theta2_N(1) = asin((n1/n2)*sin(-theta1));

% First determine width of flat face
Slope(1) = 0;
theta2_P_proj(1) = L*theta2_P(1);
theta2_N_proj(1) = L*theta2_N(1);

%Width of flat facet is length to translate the positive edge ray to right edge of Focal plane
w(1)= Wf/2-theta2_P_proj(1);
Facet_x(2) = w(1);

for i=2:60

    %Now calc new exit angle of negative dge ray so it hits left edge of focal plane
    theta2_N(i) = atan((-Wf/2 - sum(w(1:i-1)))/L);

    % Now solve the slope that results in that exit angle for theta2_N
    [Slope(i), Error(i)] = FindSlope(-theta1, n1, theta2_N(i), n2);

    %Now calculate Snell's law to find exit angles of edge rays
    PosEdgeRay_SCS(i) = theta1 - Slope(i);
    NegEdgeRay_SCS(i) = -theta1 - Slope(i);
```

```
    theta2_N_SCS(i) = asin((n1/n2)*sin(NegEdgeRay_SCS(i)));
    theta2_P_SCS(i) = asin((n1/n2)*sin(PosEdgeRay_SCS(i)));

    theta2_N_check(i) = theta2_N_SCS(i) + Slope(i);
    theta2_P(i) = theta2_P_SCS(i) + Slope(i);

    %Project edge rays onto focal plane
    theta2_N_proj(i) = L*tan(theta2_N(i));
    theta2_P_proj(i) = L*tan(theta2_P(i));


    X_Pos_N(i)= sum(w(1:i-1))+theta2_N_proj(i);
    X_Pos_P(i)= sum(w(1:i-1))+theta2_P_proj(i);

    %Translate Positive edge ray to right edge of FP
    w(i)= Wf/2 - X_Pos_P(i);

    if w(i)<1
        break;
    end

% Determine vertex points
Facet_x(2*i-1)=sum(w(1:i));
Facet_x(2*i)=sum(w(1:i));

Facet_y(2*i-1)=tan(Slope(i))*w(i);
Facet_y(2*i) = 0;

end

if length(Facet_y)>1
    Facet_x = Facet_x(1:length(Facet_x)-1);
    Facet_y = Facet_y(1:length(Facet_y)-1);

```

```
    C = (Facet_x(end)*2/Wf)^2;
else
    Facet_x = 0;
    Facet_y = 0;
    C = 1;
end

%Following code imports the profile as an object in Synopsis LightTools
lt=actxserver('LightTools.LTAPI');

lt.Cmd('\VConsole');

lt.SetOption('SHOWFILEDIALOGBOX', 0);
lt.SetOption('SHOWDIALOGS', 0);
lt.SetOption('SCRIPTING', 1);
lt.SetOption('DBUPDATE', 1);
lt.SetOption('CONFIRMDELETEMODEL', 0);
lt.SetOption('VIEWUPDATE', 1);

cmdStr = 'ExtrudedPrism ';
lt.Cmd('\V3D');
for i=1:length(Facet_x)
    cmdStr = [cmdStr ' XYZ ' num2str(Facet_x(i)) ',' num2str(Facet_y(i)) ',0'];

end
    cmdStr = [cmdStr ' XYZ ' num2str(Facet_x(i)) ',' num2str(Facet_y(i)+5) ',0'];
    cmdStr = [cmdStr ' XYZ 0,' num2str(Facet_y(i)+5) ',0'];
    cmdStr = [cmdStr ' XYZ 0,0,10'];
    cmdStr = [cmdStr ' XYZ 0,0,10'];
```